NEW MATERIALS AND STRUCTURES FOR TERAHERTZ PLASMONIC APPLICATIONS

by

Shuchang Liu

A dissertation submitted to the faculty of
The University of Utah
in partial fulfillment of the requirements for the degree of

Doctor of Philosophy

Department of Electrical and Computer Engineering

The University of Utah

May 2016

The University of Utah Graduate School

STATEMENT OF DISSERTATION APPROVAL

The dissertation of **Shuchang Liu**

has been approved by the following supervisory committee members:

Ajay Nahata	, Chair	**06/24/2015** Date Approved
Zeev Valentine Vardeny	, Member	**06/24/2015** Date Approved
Cynthia Furse	, Member	**06/24/2015** Date Approved
Steven Blair	, Member	**06/24/2015** Date Approved
Rajesh Menon	, Member	**06/24/2015** Date Approved

and by **Gianluca Lazzi** , Chair/Dean of

the Department/College/School of **Electrical and Computer Engineering**

and by David B. Kieda, Dean of The Graduate School.

ABSTRACT

This dissertation describes our work on design, fabrication and characterization of plasmonic metamaterials and tapered structures, with primary focus on their applications at terahertz (THz) frequencies. The phenomena associated with these structures rely on surface plasmon polaritons (SPPs), which may allow for high field enhancement and tight field confinement. We have investigated the underlying mechanisms of these structures and used that knowledge to develop unique and practical applications. We first studied two-dimensional periodic and random lattices based on aperture arrays, and modified the model to describe the effective dielectric response of the perforated metallic medium. Using two layers of the perforated stainless steel films, we demonstrated the emergence of an additional resonance and reproduced the transmission spectra using the effective dielectric model of the single-layer medium. Also, we improved the filtering performance of the multilayer periodic aperture arrays by adjusting the relative distance and angle between the layers, and demonstrated its application as a high quality bandpass filter. Then, we examined the transmission properties of graphite and carbon nanotube (CNT) films, and then the same films perforated with periodically distributed aperture arrays. The extracted dielectric constants of the graphite and CNT films demonstrate their availability for THz surface plasmonic devices. Moreover, we developed a narrow band/multiband THz detector in which the photoconductive antenna was surrounded by periodically corrugated gratings. This detector not only enhanced the sensitivity of

detection at the specific frequencies, but also efficiently collected the radiation within the structure area, which obviated the need for a substrate lens. Finally, we improved the concentration properties of conically tapered apertures. Based on the optimal taper angle we determined, we introduced various modifications to the individual tapered aperture, e.g., to form an array and insert a gap spacing, and further enhanced the concentration capabilities and realized complete broadband transmission. Based on these studies and results, we are currently extending our work towards development of more reconfigurable and active devices that could enrich the available pool of THz and optical devices. Furthermore, such THz devices have great promise for the development of THz systems level applications and even a THz-based world in the future.

TABLE OF CONTENTS

ABSTRACT iii

ACKNOWLEDGEMENTS viii

Chapters

1 INTRODUCTION 1

1.1 Background 1
1.2 Motivation 3
1.3 Outline 7
1.4 References 11

2 COMPREHENSIVE ANALYSIS OF DIELECTRIC PROPERTIES OF PLASMONIC METAMATERIALS 14

2.1 Introduction 14
2.2 Theoretical Analysis 17
2.3 Experimental Details 18
2.4 Experimental Results, Analytical Modeling and Discussion 20
2.5 Prospective Applications and Possible Future Directions 25
2.6 Conclusion 26
2.7 References 27

3 ENGINEERING THE PROPERTIES OF TERAHERTZ FILTERS USING MULTILAYER APERTURE ARRAYS 29

3.1 Introduction 29
3.2 Experimental Details 30
3.3 Experimental Results, Simulation and Discussion 32
3.4 Conclusion 42
3.5 References 43

4 TERAHERTZ PLASMONIC PROPERTIES OF HIGHLY ORIENTED PYROLYTIC GRAPHITE 45

4.1 Introduction 45
4.2 Experimental Details, Results and Discussion 47

4.3 Conclusion 54
4.4 References 56

5 TERAHERTZ SURFACE PLASMON POLARITONS ON FREESTANDING MULTIWALLED CARBON NANOTUBE AEROGEL SHEETS 58

5.1 Introduction 58
5.2 Experimental Details 59
5.3 Results and Discussion 61
5.4 Conclusion 68
5.5 References 69

6 COHERENT DETECTION OF MULTIBAND TERAHERTZ RADIATION USING A SURFACE PLASMON-POLARITON BASED PHOTOCONDUCTIVE ANTENNA 71

6.1 Introduction 71
6.2 Experimental Details 72
6.3 Experimental Results, Simulation and Discussion 74
6.4 Conclusion 80
6.5 References 80

7 OPTIMIZATION OF GEOMETRICAL PARAMETERS OF INDIVIDUAL CONICALLY TAPERED APERTURES 83

7.1 Introduction 83
7.2 Experimental Details 84
7.3 Experimental Results, Simulation and Discussion 87
7.4 Supplementary Information 92
7.5 Conclusion 94
7.6 References 94

8 CONCENTRATION OF BROADBAND TERAHERTZ RADIATION USING A PERIODIC ARRAY OF CONICALLY TAPERED APERTURES 97

8.1 Introduction 97
8.2 Experimental Details 98
8.3 Experimental Results, Simulation and Discussion 101
8.4 Conclusion 108
8.5 References 108

9 TRANSMISSION BLEACHING AND COUPLING CROSSOVER IN A SPLIT TAPERED APERTURE 110

9.1 Introduction 110
9.2 Experimental Details 112
9.3 Experimental Results, Simulation and Discussion 115

9.4 Supplementary Information: Comparison between Tapered Apertures and a Conventional Lens 124
9.5 Conclusion 125
9.6 References 127

10 NEAR-FIELD IMAGING USING BROADBAND TERAHERTZ TRANSMISSION THROUGH TAPERED APERTURES 130

10.1 Introduction 130
10.2 Experimental Details 132
10.3 Experimental Results and Discussion 134
10.4 Conclusion 141
10.5 References 141

11 FUTURE WORK AND CONCLUSIONS 144

11.1 Future Work 144
11.2 Conclusions 147
11.3 References 152

ACKNOWLEDGEMENTS

This section triggers a lot of my thoughts and memories, now that I organize them and write down all the thanks on paper which I wanted to send out during the last five and a half years, as a period of my Ph.D. life working on this dissertation.

First of all, I would like to express my most sincere gratitude to Dr. Ajay Nahata, for his invaluable guidance and strong support throughout my Ph.D. study. As an old Chinese saying goes, "For one day my teacher, for ever my parent." Although I wish to say these words to all my teachers and instructors, they are especially appropriate for Dr. Nahata. When I came to the US for the Ph.D. program here just after my undergraduate study, I hadn't gone through systematic research training. Moreover, that was the first time I came abroad and my English needed a lot of work. In this case, Dr. Nahata helped me and cared for me in every aspect. I learned from him independent thinking, scientific writing and effective communication. He is not only good at research but also at with people, both of which had a subtle interacting but important impact on me. He is always right there waiting for you to ask any questions on any subject, from study to life. I still remember the time when I hurt my finger in the office and he took me to the clinic, and hundreds of times he corrected my English pronunciation and grammatical errors. Though some of them look trivial, they largely influenced me and helped me grow up, not only as a researcher but also to be a better person. Thus, I want to say, Dr. Nahata is my mentor, and he is more like my father, friend and role model.

I want to express my appreciation to Dr. Valy Vardeny for his encouragement and guidance throughout this project. His charisma – passion, dedication and humor – deeply impressed me. I have learned a lot from his profound knowledge, rich experience and insightful views in class and in research. His unselfish and timely help always encouraged me and benefited me.

I am thankful to Dr. Steve Blair for his guidance and advice in my work. Moreover, his course on Nanophotonics took me into a much broader world of plasmonics and facilitated the accomplishment of this thesis to a large extent.

I would also like to extend my appreciation to Dr. Rajesh Menon. I still remember every time when I knocked at his office and asked help for course materials and Matlab in my first semester, and he reached out to me with his patience and knowledge. His guidance helped me overcome difficulties at that time and later.

I am also very thankful to Dr. Cynthia Furse for her guidance and for serving on my committee. Her kindness and her contribution to the women engineers' society profoundly encouraged me and increased my confidence as a woman engineer.

Again, I want to express my gratitude to all my teachers and instructors, including all my committee members just mentioned, and Dr. Schurig, Dr. Bartl, Dr. Scarpulla and Dr. Mitrofanov, for generously enriching me in knowledge and putting me on their shoulders to make me see farther.

Finally, I would like to thank my group members and collaborators for their suggestions, help and dedication, which made my course of research easier and more reasonable. Specifically I want to thank Dr. Nguyen and Dr. Kumar, who worked with me in the first two years of my study, and guided and helped me to start as a researcher. I

would also like to thank all my friends for without them my life could not be so colorful and joyful.

Lastly and most importantly, I would like to express my indebtedness to my family, especially to my parents, for their full support to me, their only child, to go farther away home. They center all their love and attention on me, educating me and enlightening me after I was born. I also dedicate this work to the memory of my grandfathers and grandmothers who all taught me to be an honest and independent person and offered me so much affection and care. My family will be an unlimited source of power for me. I am grateful to them for everything they have given me.

Thank you to all the beloved people in my life, and to those who appeared in my life to prompt me to move forward. All the love and motivation I have received and will receive from you continues to encourage me to be a better and better person.

CHAPTER 1

INTRODUCTION

1.1 Background

Optics is a long-standing topic that has inspired human beings since ancient times due to the direct connection between light and vision and the vitality it preserves through entanglement with various aspects of science, engineering and technology. However, it turns out that the mysteries of light are not as easy to perceive as is the colorful world. It is destined to be a long quest for human beings to try understanding light, and this journey leads to an understanding of a broader world and the opening of new eras. Today, although optical and photonic devices have occupied a large area of the market, our daily life is still dominated by electronics. This can be attributed to a variety of considerations, such as volume, flexibility, cost, reliability, and manufacturability. However, the development of artificial intelligence and automation demonstrates that beyond all the factors mentioned above, convenience is placed as the top priority, and it gives light many unique advantages over other subjects. As examples, stereoscopic visualization and tabletop displays can make life more organized and everything clear at a glance. With this said, optics still contains great potential and deserves effort on the development of more advanced devices.

Although optics is first defined through visual perception when visible light is employed by human eyes to perceive our colorful world, it is a much broader concept and

has served to integrate many different subdisciplines in science, engineering and technology, and spans the entire electromagnetic spectrum. With the different mechanisms, there is a deep barrier in the interactions between electronics and photonics, while it is easier and more arbitrary to tune light depending on its adjacent electromagnetic frequencies. With this view in mind, current advances in optics span a broader range of fields, and we could expect the further developments to serve to enhance current capabilities, as well as to revolutionarily change the ways we understand and interact with the world around us. One of the electromagnetic bands close to the visible range lies from about 100 GHz to 10 THz, which is recognized as the far-infrared or terahertz (THz) frequency range. In general, this spectral region is the last unexploited portion of the electromagnetic spectrum, since it is not easily accessible using conventional electronics or photonics. Although the technologies in its neighboring spectral regions are rather mature, practical devices that operate in the THz region are still rather rudimentary. To solve this problem, approaches have been made to this region from both above (by extending optical techniques to lower frequencies) and below (by extending electronic measurements to higher frequencies). However, in this region the physical phenomena and material properties are unique and, thus, simple scaling often cannot be applied and new techniques need to be developed. Despite the fact that this has made the field very challenging, it has long been recognized as a region of great scientific interest and technological importance, and has led to various applications.

One of the unique aspects of the THz spectral range is the development of the approach to the temporal measurement of the signals via THz time-domain spectroscopy (THz-TDS) [1]. Using this approach, the time-domain electrical field transient can be

measured by sweeping the coherent femtosecond laser pulses when increasing the optical path length in one branch of the pump-probe scheme, and subpicosecond temporal resolution can be obtained. In contrast to conventional optical measurements, where the transmitted optical power is measured, the direct measurement of the THz electric field yields a complete set of data with both amplitude and phase information, which is significant in understanding the mechanisms revealed by the complex form of the electrical field. More specifically, the real and imaginary components of the dielectric constant can be completely computed based on the complex amplitude coefficient, avoiding the use of Kramers-Kronig analysis.

Based on the current situation in the area of THz applications, my research is focused on investigating the underlying mechanisms of the surface plasmonic structures, exploring unconventional plasmonic materials, and designing new devices for surface plasmonic applications at THz frequencies. The work described in this thesis is focused on three topics that include examination and characterization of THz plasmonic properties of a variety of materials, demonstration of constructing high performance THz devices using periodically structured metal films, and optimization of conically tapered apertures for concentration of terahertz (THz) radiation to benefit the practical near-field microscopic and imaging systems.

1.2 Motivation

In order to develop new techniques for the THz spectral range, SPPs are one of the possible solutions that provide unique features. The surface plasmon polaritons (SPPs) are electromagnetic excitations bound to the interface between a metal and a dielectric. They mediate the metal-light interaction via coupling of the electromagnetic field to the

oscillations of the conductor's electron plasma. The SPPs are evanescent waves and decay exponentially from the metal-dielectric interface, so they are different from the free-space electromagnetic waves—for example, they are not restricted by the diffraction limit. Due to their tight bounding to the interface, they can tightly confine, effectively guide and efficiently focus radiation. One of the important publications in this field, from Ebbesen et al., described the extraordinary optical transmission (EOT) through metallic periodic lattices with structures on the scale of or less than the wavelength of light [2]. This phenomenon relies on the SPPs modulated by the two-dimensional (2D) periodic lattices, and the transmission is greatly enhanced at the wavelengths, which is equal to the lattice periodicity. Therefore, the SPPs can also strongly enhance the radiation based on the resonance effect.

In the surface plasmonic applications, the dielectric properties of the metal highly influence the performance of the device. Because of this, gold and silver are the primary metals that are used at optical frequencies, because most other metals exhibit unacceptably high losses. In contrast, plasmonic applications at longer wavelengths, such as in the terahertz (THz) spectral range, have an advantage that the conductivities of all conventional metals are sufficiently high so that relatively low losses are incurred over reasonable propagation lengths. The wider selection of metallic materials will greatly benefit the fabrication processes and enrich the possible functionalities of devices.

The enhanced transmission through 2D periodic arrays of subwavelength apertures has attracted significant attention in exploring the underlying physical mechanisms behind the phenomenon [3,4]. In Chapter 2-5 we discuss our work on the 2D arrays of subwavelength apertures fabricated in stainless steel foils, graphite films and

layers of multiwalled carbon nanotubes. We describe the dielectric properties of these plasmonic metamaterials with the modification to the analytical model we previously defined [5]. We again confirm that this model is valid and quite powerful in characterizing the dielectric properties of plasmonic metamaterials. We also develop a high performance filter with multiple layers of periodic aperture arrays made in stainless steel foils based on the associated plasmonic effect. Although conventional metals are usually selected in SPP applications, their conductivity cannot be easily altered, which is a highly desirable characteristic in developing active plasmonic devices. In this case, the graphite and multiwalled carbon nanotubes (MWCNTs) are expected to be potential candidates in active plasmonic applications, since they have a number of unique characteristics, including a highly anisotropic conductivity, which could be altered. We provide evidence with the dielectric information that graphite and carbon nanotubes could be used as plasmonic media.

Besides the demonstration of the perforated apertures patterned in 2D periodic lattices as mentioned above, another example of the surface plasmonic structures include a subwavelength single aperture surrounded by periodically spaced circular corrugations, which is referred to as a bullseye structure. This structure is first proposed by Thio et al., who found that the optical transmission could also be strongly enhanced at wavelengths corresponding to the period spacing of the corrugated gratings [6]. Based on these initial demonstrations at optical frequencies [6–8], there has also been work on this geometry in other frequencies [9,10]. Moreover, our group carefully studied this geometry fabricated with variable numbers and parameters of concentric annular grooves on stainless steel foils at THz frequencies [11–14]. With the fundamental understanding to the plasmonic

mechanism of the bullseye structure, we discuss our work on highly sensitive THz detectors based on periodically corrugated gratings surrounding a photoconductive antenna in Chapter 6.

In the previous section, we focus on the periodic structures that can excite SPPs and enhance the coupled electromagnetic radiation. In fact, the unique dispersion properties of SPPs also allow them to be tightly focused to dimensions smaller than the corresponding free-space diffraction limit. To realize this objective, tapered structures are typical choices, such as tapered apertures, tapered wires and tapered parallel plate waveguides. The first realizations of near-field surface plasmonic focusing emerged in the optical microscopic field in 1984 [15]. A sharply pointed quartz crystal tip coated by metal with a small aperture was used as the probe and the resolution was achieved at 25 nm. In 1997 [16] and in 2000 [17], Nerkararyan published two theoretical papers analyzing the ability to achieve superfocusing of SPPs in a wedge-like structure and a conical structure, and mentioned that a tapered structure would result in the focusing of polaritons and anomalous increase of electric field. However, until 2004, researchers mainly focused their attention on near-field scanning optical microscopy and neglected the highly concentrated power associated with the focusing process. The significance of superfocusing in tapered structures was clarified in 2004, when Stockman clearly stated the nanofocusing of energy in a tapered plasmonic waveguide [18]. Most importantly, he pointed out that the nanofocusing could essentially foster various prospective applications in nano-optics and nanotechnology with also greatly enhanced optical fields. This work has aroused great interest in studying tapered structures.

Among the different geometries of tapered structures, the tapered

apertures/tapered hollow waveguides are widely used in near-field microscopy [19] and other optical components [20–22]. Associated with the applications, there has been sufficient theoretical analysis on this geometry, but few systematic experimental studies have been done on the properties of the geometry. Based on the initial experimental work in our group [23], we continue the study on the characterization of concentrating THz radiation through conically tapered metallic apertures in Chapter 7-10. Our goal is to study the parameters of the structure and improve its performance by modifications to the geometry. The optimized structure could enhance the capabilities of such a probe in near-field microscopy and imaging. To demonstrate the feasibility of the probe, we set up a practical near-field imaging system.

1.3 Outline

Here, we review our work in each chapter before the major part of this dissertation to give a brief overview of the scope of our work.

In Chapter 2, we systematically demonstrate an approach to measure the dielectric response $\varepsilon(\omega)$ of subwavelength aperture arrays fabricated in metal films using THz-TDS, and modeled the response based on the geometric parameters of the arrays. Using THz-TDS, we are able to directly obtain the complex dielectric response function from the THz experimental transmission measurements. Based on a model we developed before, we make effective modifications and obtain a much better fit to the experimentally extracted data. In the following two chapters, we will see that the modified model works well with double layers of aperture arrays in stainless steel foils and the aperture arrays in the films of graphite. In addition, by efficient characterization of the graphite and carbon nanotube films in Chapters 4 and 5, we provide evidence that they have good surface

plasmonic properties.

Following the studies in the last chapter, we experimentally demonstrate the ability to create additional transmission resonances in a double-layer aperture array by varying the interlayer gap spacing in Chapter 3. In the case of periodic aperture arrays, these additional resonances are sharply peaked, while for random aperture arrays the resonances are broad. Notably, these additional resonances only explicitly occur when the interlayer gap spacing is greater than half the aperture spacing on a single periodic array. Since there is no corresponding periodicity in the random arrays, these resonances occur regardless of how small the gap spacing is made. This phenomenon can be accurately modeled only if the correct frequency-dependent complex dielectric function of a metal film perforated with subwavelength apertures is used. We conclude by demonstrating several passive free-space THz filters using multilayer aperture arrays. Importantly, we show that the magnitude of the lowest order resonance can be approximately maintained, while the background transmission can be significantly suppressed, leading to a significant improvement in the optical filter fidelity.

In Chapter 4, we demonstrate that highly oriented pyrolytic graphite is a potentially useful material for plasmonic applications in the THz spectral range. Using THz-TDS, we study the transmission properties of a ~ 7.5 μm thick graphite film made via mechanical exfoliation, and find that the complex dielectric constant follows the Drude model with a plasma frequency ν_p = 34 THz. To assess the graphite plasmonic properties, we fabricate a subwavelength periodic aperture array in the graphite film and in a free-standing stainless steel film. Despite the low conductivity of graphite compared to conventional metals, the resonant transmission properties are similar.

We also demonstrate that MWCNTs are capable of supporting SPPs at THz frequencies in Chapter 5. To achieve this, we fabricate sub-100 μm-thick freestanding and highly oriented MWCNT aerogel sheets. Utilizing THz-TDS, we measure the complex index of refraction of the sheets for two orthogonal nanotube orientations. We find that the MWCNT sheets exhibit highly anisotropic THz polarization behavior. Based on the extracted dielectric properties of the medium, which show that it exhibits metallic behavior in the THz spectral range, we investigate the existence and propagation of SPPs by studying the resonantly enhanced transmission through periodic MWCNT hole arrays. We find that carbon nanotubes support SPP excitations that propagate along the tubes, but highly suppress these surface waves in the direction perpendicular to the nanotubes.

In Chapter 6, we characterize a dipole antenna structure that allows for coherent detection of narrowband THz radiation with enhanced sensitivity at the resonant frequency. The antenna incorporates a corrugated metal structure that surrounds the dipole. Each periodically spaced groove in the corrugation couples an approximate replica of the incident THz pulse to a SPP pulse, which then propagates towards and is detected by the dipole. We use numerical simulations to validate the experimental data. Based on these results, we describe a multiband dipole antenna detector that allows for enhanced sensitivity at multiple frequencies. This device can also be used as an emitter.

In Chapter 7, we optimize the geometrical properties of individual conically tapered apertures (TAs) as a first step for our following research on the same geometry. By taking the requirements of practical applications into consideration, we keep the output aperture diameter fixed, and find that the optimal taper angle is 30°. A consequence of increasing the taper angle is that the effective cutoff frequency red shifts,

which can be readily explained using conventional waveguide theory.

Based on the preceding research, we describe the optical concentration properties of periodic arrays of conically tapered metallic apertures measured using THz-TDS in Chapter 8.We fabricate and measure the transmission properties of a periodic (hexagonal) array of optimized TAs. In contrast to periodic arrays of subwavelength apertures in thin metal films, which are characterized by narrowband transmission resonances associated with periodic spacing, here we observe broadband enhanced transmission above the effective cutoff frequency. Further enhancement in the concentration capabilities of the array can be achieved by tilting the apertures towards the array center, although the optical throughput of individual TAs is reduced with increasing tilt angle. Finally, we discuss possible future directions that utilize cascaded structures, as a means for obtaining further enhancement in the amplitude of the transmitted THz radiation.

In Chapter 9, we investigate the spectral transmission properties of conically tapered metallic apertures made in a split metallic plate using THz-TDS. The introduction of even a small gap between the two halves of the plate results in spectral broadening of the transmitted radiation due to a reduction of the cut-off effect. We find that the resulting transmission spectrum can be described as a weighted sum of the spectra associated with a TA and a parallel plate waveguide, with the gap spacing controlling the relative ratio. We further find that the field concentration properties of the aperture in a split plate are limited by the radiation leakage through the gap, and propose a tapered shell structure to realize strong broadband field concentration. Using numerical simulations, we validate these observations and yield insight into the mode properties within the split TA.

Then in Chapter 10, we demonstrate the near-field imaging capabilities of the

split shell TA, in which the sidewall thickness is small in the vicinity of the gap, using broadband THz radiation. In contrast to conventional conically tapered apertures, which are characterized by strong transmission suppression below the cutoff frequency, the combination of these geometrical features allows for significantly enhanced transmission at frequencies below the cutoff frequency, without compromising the spatial resolution of the structure. We fabricate such a structure consisting two pieces, such that there is an adjustable gap along the length of the structure. We demonstrate the utility of this probe for near-field imaging using a sample that is simultaneously imaged at several frequencies that lie above, near and below the cutoff frequency. We observe only mild degradation in the image quality as the frequency is reduced below the cutoff frequency. These results suggest that further refinements in the probe structure will allow for improved imaging capabilities at frequencies well below the cutoff frequency.

Finally in Chapter 11, we propose some new directions based on the work from previous chapters that can also be extended to develop more devices.

1.4 References

1. D. Grischkowsky, *Frontiers in Nonlinear Optics* (Philadelphia: Institute of Physics Publishing, 1992).
2. T. W. Ebbesen, H. J. Lezec, H. F. Ghaemi, T. Thio, and P. A. Wolff, "Extraordinary optical transmission through subwavelength hole arrays," Phys. Rev. Lett. **391**, 667–669 (1998).
3. C. Genet and T. W. Ebbesen, "Light in tiny holes," Nature **445**(7123), 39–46 (2007).
4. F. J. Garcia-Vidal, L. Martin-Moreno, T. W. Ebbesen, and L. Kuipers, "Light passing through subwavelength apertures," Rev. Mod. Phys. **82**(1), 729–787 (2010).
5. A. Agrawal, Z. V Vardeny, and A. Nahata, "Engineering the dielectric function of plasmonic lattices," Opt. Express **16**(13), 9601–9613 (2008).
6. T. Thio, K. M. Pellerin, R. A. Linke, H. J. Lezec, and T. W. Ebbesen, "Enhanced

light transmission through a single subwavelength aperture," Opt. Lett. **26**(24), 1972–1974 (2001).

7. H. J. Lezec, A. Degiron, E. Devaux, R. A. Linke, and T. W. Ebbesen, "Beaming light from a subwavelength aperture," Science **297**, 820–822 (2002).

8. A. Nahata, R. A. Linke, T. Ishi, and K. Ohashi, "Enhanced nonlinear optical conversion from a periodically nanostructured metal film," Opt. Lett. **28**(6), 423–425 (2003).

9. S. S. Akarca-Biyikli, I. Bulu, and E. Ozbay, "Enhanced transmission of microwave radiation in one-dimensional metallic gratings with subwavelength aperture," Appl. Phys. Lett. **85**(7), 1098–1100 (2004).

10. M. J. Lockyear, A. P. Hibbins, J. R. Sambles, and C. R. Lawrence, "Surface-topography-induced enhanced transmission and directivity of microwave radiation through a subwavelength circular metal aperture," Appl. Phys. Lett. **84**(12), 2040–2042 (2004).

11. H. Cao, A. Agrawal, and A. Nahata, "Controlling the transmission resonance lineshape of a single subwavelength aperture," Opt. Express **13**(3), 763–769 (2005).

12. A. Agrawal, H. Cao, and A. Nahata, "Time-domain analysis of enhanced transmission through a single subwavelength aperture," Opt. Express **13**(9), 3535–3542 (2005).

13. A. Agrawal, H. Cao, and A. Nahata, "Excitation and scattering of surface plasmon-polaritons on structured metal films and their application to pulse shaping and enhanced transmission," New J. Phys. **7**, 249 (2005).

14. A. Agrawal and A. Nahata, "Time-domain radiative properties of a single subwavelength aperture surrounded by an exit side surface corrugation," Opt. Express **14**(5), 1973–1981 (2006).

15. D. W. Pohl, W. Denk, and M. Lanz, "Optical stethoscopy: Image recording with resolution λ/20," Appl. Phys. Lett. **44**(7), 651–653 (1984).

16. K. V. Nerkararyan, "Superfocusing of a surface polariton in a wedge-like structure," Phys. Lett. A **237**, 103–105 (1997).

17. A. J. Babadjanyan, N. L. Margaryan, and K. V. Nerkararyan, "Superfocusing of surface polaritons in the conical structure," J. Appl. Phys. **87**(8), 3785–3788 (2000).

18. M. Stockman, "Nanofocusing of optical energy in tapered plasmonic waveguides," Phys. Rev. Lett. **93**(13), 137404 (2004).

19. E. Betzig, J. K. Trautman, T. D. Harris, J. S. Weiner, and R. L. Kostelak, "Breaking the diffraction barrier: optical microscopy on a nanometric scale," Science **251**(5000),

1468–1470 (1991).

20. I. K. Ilev and R. W. Waynant, “Grazing-incidence-based hollow taper for infrared laser-to-fiber coupling,” Appl. Phys. Lett. **74**(20), 2921–2923 (1999).

21. R. G. DeCorby, N. Ponnampalam, E. Epp, T. Allen, and J. N. McMullin, “Chip-scale spectrometry based on tapered hollow Bragg waveguides,” Opt. Express **17**(19), 16632–16645 (2009).

22. H. Dalir, Y. Yokota, and F. Koyama, “Spatial mode multiplexer/demultiplexer based on tapered hollow waveguide,” IEICE Electron. Express **8**(9), 684–688 (2011).

23. T. D. Nguyen, Z. V. Vardeny, and A. Nahata, “Concentration of terahertz radiation through a conically tapered aperture,” Opt. Express **18**(24), 25441–25448 (2010).

CHAPTER 2

COMPREHENSIVE ANALYSIS OF DIELECTRIC PROPERTIES OF PLASMONIC METAMATERIALS

2.1 Introduction

One of the first material parameters that scientists examined while studying the interaction between light and substance is refractive index, which is ubiquitous in its appearance in the classic optical laws, e.g., Snell's Law, Fermat's Principle, etc. Along with greater understanding of light-material interactions, the concept of material properties has been extended to a complex and multivariate parameter, and its most general embodiments are permittivity and permeability. Maxwell's Equations are macroscopic laws that govern the propagation properties of electromagnetic waves, and permittivity and permeability are the elements necessary to express the relations. Moreover, the material properties have been exploited to guide the electromagnetic fields. In classic examples, lenses and prisms are designed into various shapes, such that the refractive indices in the optical path determine the direction of optical rays. In a more advanced case, numerical methods can be applied to properly design the material properties to effectively engineer the functionality of various devices. One important algorithm to achieve this goal is by means of transformation optics, which maps the distortion of fields to the inhomogeneity of material properties through topology [1,2]. Due to the universality of the design and the diversity of the applications,

transformational optics has attracted enormous attention in the last decade, including a variety of implementations, e.g., invisible cloaking [3–6], beam shifters and splitters [7], lenses and light concentrators [8–10], field rotators [11], enhanced scatterers [12], waveguide bends and corners [13], deep-subwavelength waveguides [14], and even optical-illusion devices [15].

All the examples above demonstrate that the dielectric properties of a medium are not only central to understanding the electromagnetic phenomena, but also of fundamental importance in constructing demand-oriented devices. In many cases, especially when transformation optics is applied, the devices require materials with extraordinary electromagnetic characteristics that are difficult or impossible to achieve with conventional, naturally occurring materials but can be realized by a new class of materials called metamaterials [16]. The permittivity and permeability values of the metamaterials can be designed to vary independently and arbitrarily throughout a material by tailoring the subwavelength details of the structures, and thus they are usually exploited to fulfill the demand of inhomogeneous materials for unconventional devices, e.g., the aforementioned example of invisible cloaking [3–6]. In order to better exploit metamaterials for practical applications, we must answer two questions: 1. How do we calculate the dielectric response of metamaterials; 2. How do we model the dielectric properties according to the dimensions of the subwavelength structures? These two questions are complementary. The former has been applied in constructing the metamaterial devices, but in order to realize specific values, the dimensions are determined through trial and error, or through an evolutionary algorithm. For the latter, although people tried to model some of the metamaterial to an IC circuit, much of the

work has focused on a single unit and few studies investigated the structure from a material perspective. However, as stressed above, to analytically model the dielectric properties of metamaterials is important and efficient in device implementation, while the numerical method is time- and energy- consuming.

The plasmonic subwavelength structure is within the category of metamaterials. The concept of the plasmonic metamaterial was first put forward by Pendry et al. [17]. Assuming that metals are perfect conductors, they proposed a theoretical framework hypothesizing that metallic films perforated with periodically spaced apertures exhibit an effective dispersion relation due to the excitation of surface plasmon polaritons (SPPs). Thus the electromagnetic field is governed by an effective permittivity; the effective plasma frequency is distinct from the material plasma frequency and can be approximated by the cut-off frequency of the waveguide mode in the individual apertures. Based on this concept and Drude model as well as Fano-type resonance from a more material-based perspective, we then developed the equation of the effective permittivity into a complete form [18]. By means of this model, the effective permittivity can, in principle, be designed to exhibit any response that we expect it to be, which provides great flexibility in designing a variety of unique plasmonic metamaterials. In this chapter, we modified the analytical model to better describe the dielectric properties of plasmonic metamaterials. Using this method, we modeled single layers of periodic and random aperture arrays made in stainless steel foils. In the next chapter, we confirmed the validation of this model with double layers of periodic and random aperture arrays in stainless steel foils and developed a high-quality array filter based on our studies of multi-layer aperture arrays. In addition, we provide evidence with the dielectric

information that graphite and carbon nanotubes could be used as plasmonic materials, and also modeled the dielectric properties of graphite with the parameters of the structured pattern, in the following chapters.

2.2 Theoretical Analysis

The calculation of permittivity and permeability of the homogeneous materials could be fulfilled by Fresnel's equations with complex transmittance and reflectance (including phase information). According to the Fresnel equations, the reflection and transmission coefficients can be written as

$$r_{ab}^{TE} = \frac{n_a \cos\theta_i - n_b \cos\theta_t}{n_a \cos\theta_i + n_b \cos\theta_t}, \tag{2.1}$$

$$t_{ab}^{TE} = \frac{2n_a \cos\theta_i}{n_a \cos\theta_i + n_b \cos\theta_t}, \tag{2.2}$$

$$r_{ab}^{TM} = \frac{n_b \cos\theta_i - n_a \cos\theta_t}{n_b \cos\theta_i + n_a \cos\theta_t}, \tag{2.3}$$

$$t_{ab}^{TM} = \frac{2n_b \cos\theta_i}{n_b \cos\theta_i + n_a \cos\theta_t}, \tag{2.4}$$

where the superscripts TE and TM represent the polarization directions of the components (any general waves can be decomposed into TE and TM waves), n_a and n_b are the refractive indices of the two media where the wave is incident from and transmitted to, and θ_i and θ_t are the incident and refraction angles. Here if we consider a simple case where the wave is incident normally to the face of a planar slab of a homogeneous material in the air (refractive index $n_o = 1$), as shown in Fig. 2.1, the wave passes through two interfaces and could undergo multiple internal reflections as the Fabry-Perot effect. Thus the equation could be written as

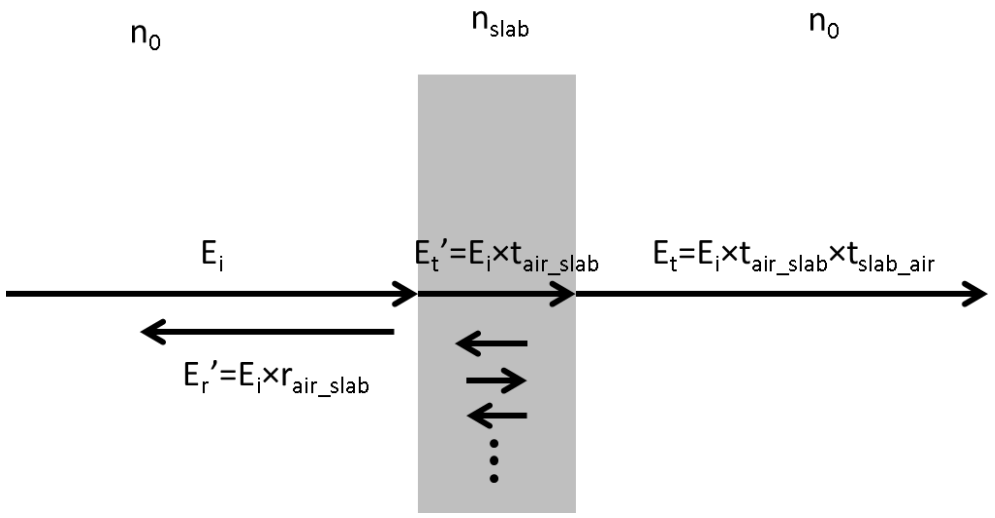

Figure 2.1. Schematic diagram of a planar slab of a homogeneous material in the air with the wave normally incident to the surface.

$$
\begin{aligned}
t_{total} &= t_{air\_slab} t_{slab\_air} e^{-ik(n_{slab}-n_0)l} \\
&\times \left[1 + r_{slab\_air} r_{air\_slab} e^{-i2kn_{slab}l} + \ldots + \left(r_{slab\_air} r_{air\_slab} e^{-i2kn_{slab}l}\right)^n\right] \\
&\cong t_{air\_slab} t_{slab\_air} e^{-i\frac{2\pi f (n_{slab}-n_0)l}{c_0}} \frac{1}{1 - r_{slab\_air} r_{air\_slab} e^{-i\frac{4\pi f n_{slab} l}{c_0}}}
\end{aligned}
\tag{2.5}
$$

Here, l is the thickness of the material, $k=2\pi f/c_o$ is the wavenumber and f is the frequency. Upon solving this equation, the refractive index of the slab could be extracted. The detailed extraction procedure of this equation could be found in Ref. [19].

2.3 Experimental Details

In our experiment, we fabricated two-dimensional (2D) aperture arrays in d = 75 μm thick, ~5×5 cm^2 area of freestanding stainless steel metal foils by laser cutting using a frequency tripled Nd:YAG laser. Two different aperture arrays, based on periodic and random hole patterns, respectively, were designed and fabricated. The periodic aperture

array consisted of 2D periodically spaced circular holes on a square lattice with a lattice constant, a = 1.5 mm, and aperture diameters, D = 750 μm, while the random aperture array consisted of 2D randomly distributed circular holes designed to have an average spacing, a' = a, and the same aperture diameter D. As a result, these two different arrays have the same fractional aperture area of ~19%. In Fig. 2.2, we show the photos of the periodic and random aperture arrays.

We used THz time-domain spectroscopy (THz-TDS) to measure the optical transmission spectra, t(ω), of the perforated metal films, where the THz frequency ν = ω/2π [7]. A pair of off-axis paraboloidal mirrors was used to collect and collimate the THz radiation from the emitter, which was then normally incident on the aperture array structures. Each array was attached to a solid metal plate with a 5 cm × 5 cm opening that was placed in the path of the collimated THz beam. The 1/e THz beam diameter was smaller than the aperture opening in the metal holders and the spatial extent of the aperture array structures, thereby minimizing edge effects due to the finite size of the array samples. Reference transmission spectra were taken with just the metal holders in the THz beam path using the same setup. The metallic foils were completely opaque prior to fabrication of the arrays. Therefore transmission through the perforated metallic films was uniquely due to the apertures.

The detected transient photocurrent was then Fourier transformed and normalized to the reference transmission, yielding the electric field transmission spectrum, t(ω), which contains both the magnitude and phase of the amplitude transmission coefficient, t(ω), using the relation

$$t(\omega) = |t(\omega)| \exp[i\varphi(\omega)] = \frac{E_{transmitted}}{E_{reference}} \tag{2.6}$$

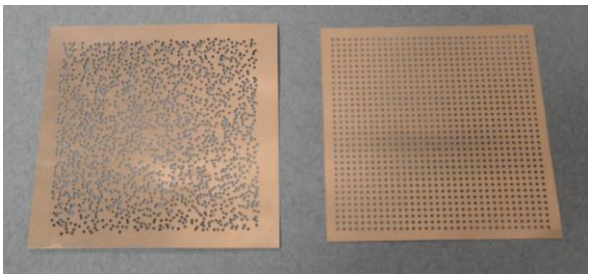

Figure 2.2. The photo of the two aperture arrays used in the experiment, the random array on the left and periodic array on the right.

In this expression, $E_{transmitted}$ and $E_{reference}$ are the incident and transmitted THz fields, respectively, $|t(\omega)|$ and $\varphi(\omega)$ are the magnitude and phase of the amplitude transmission coefficient, respectively, and $\nu = \omega /2\pi$ is the THz frequency.

As mentioned in Chapter 1, using the THz-TDS, the complex expression of the variables in Eq. (2.5) could be obtained directly from the magnitude and phase of the amplitude coefficient.

2.4 Experimental Results, Analytical Modeling and Discussion

The amplitude transmittance, $t(\omega)$, and phase, $\phi(\omega)$, spectra for the random aperture array medium with normal incidence are shown in Fig. 2.3(a) and its inset. Under this circumstance, since most conventional metals exhibit low loss in the THz spectral range (including the stainless steels), the absorption of the samples is negligible. We can simultaneously extract the real and imaginary components of the effective refractive index $n(\omega)$ using the magnitude, $|t(\omega)|$, and the phase spectra, $\varphi(\omega)$ of the amplitude transmittance [19]. Since the effective permeability μ is frequency independent and of the order of 1 in the non-magnetic materials [17,20], the effective permittivity ε could be examined through $\varepsilon = n^2$, as shown in Fig. 2.3(b) (red lines). As is demonstrated

in [18], ε(ω) exhibits the dispersion properties of a plasma, similar to that of a metallic medium, and thus can be fitted with a Drude model. However, the model is distinguished with an effective plasma frequency approximately equal to the waveguide mode cutoff frequency, f_c of a cylindrical aperture. f_c here is given by the relation $f_c = c\chi_m/\pi D$, where χ_m is a mode-dependent constant equal to 1.841 for the lowest-order mode (TE_{11}), and c is the speed of light. We obtained an excellent fit to the real and imaginary components of ε(ω), as shown in Fig. 2.3(b) (blue lines), with fit parameters given in Table 2.1, using the complex ε(ω) response of the plasmonic lattices in the form of the 'lossy plasma':

$$\tilde{\varepsilon}(\omega) = \varepsilon_r \left(1 - \frac{\tilde{\omega}_p^2}{\omega^2 + i\gamma\omega} \right) \tag{2.7}$$

where $\tilde{\omega}_p$ is the effective plasma frequency, ε_r is the high frequency dielectric constant, and γ is the plasma relaxation rate.

The individual uncorrelated apertures in the random aperture array result in a broad continuous transmission band [Fig. 2.3(b)]. In contrast, the transmission spectrum associated with the periodic aperture array is characterized by resonant transmission bands. Fig. 2.4(a) and its inset show t(ω) and ϕ(ω) spectra, respectively, also measured at normal incidence. The measured transmission spectra exhibit enhanced resonance peaks and concomitant sharp antiresonance (AR) dips immediately to the right of the resonance peaks, as shown in the measured transmission spectra in Fig. 2.4(a). We have shown previously that the AR feature is directly related with the underlying structure factor [21], and matches the equation [22,23]

$$\omega_{Tj} = \frac{2\pi c}{a}\sqrt{m^2 + n^2}\ , \tag{2.8}$$

where c is the speed of light in a vacuum, a is the lattice periodicity, m and n are integers,

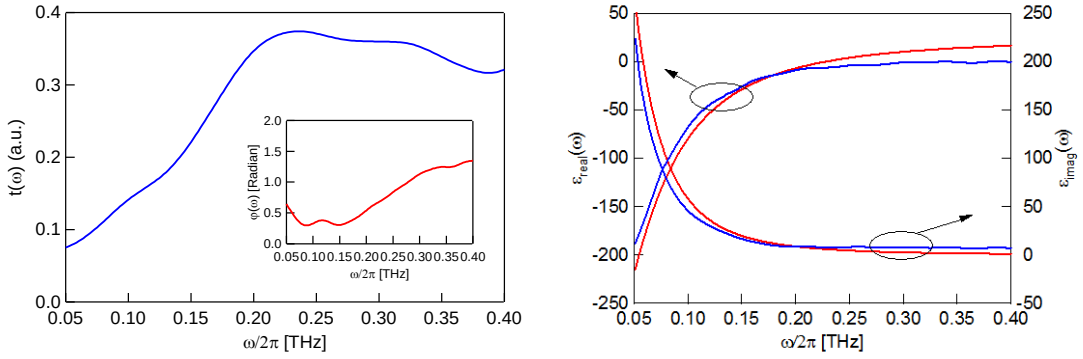

(a) (b)

Figure 2.3. Determination of the real and imaginary components of ε(ω) for the random aperture array with D = 750 μm and fractional aperture area of ~19%. (a) The amplitude transmission t(ω) and phase ϕ(ω) (inset) spectra of the random aperture array measured using THz-TDS. (b) Spectra of real and imaginary ε(ω) components (red line) obtained from t(ω) and ϕ(ω) shown in Fig. 2.3(a). The modeled ε(ω) of the random aperture array (blue line) is based on Eq. (2.7) with parameters given in Table 2.1.

Table 2.1. The "best fit" parameters for the effective ε(ω) of random aperture arrays with D = 750 μm. The parameters are defined in Eq. (2.7).

ε_r	$\tilde{\omega}_p$ (rad/ps)	γ (rad/ps)
37	0.73	0.35

and we assume n_{eff} = 1 for the refraction index of SPP along air-metal interface in the THz spectral range [21]. Using the two measured spectra, we again obtained the dielectric response shown in Fig. 2.4(b) (red lines), for the real and imaginary ε(ω) components.

As is also demonstrated in Ref. [18], ε(ω) of the periodic lattice is strongly modulated in the vicinity of the resonant frequencies. Although we have carefully studied the dielectric response in Ref. [18], superposing the Fano-type interference on the Drude model in Eq. (2.7) and quantitatively described it using inherent reciprocal vectors of the periodic aperture arrays having periodicity G = 2π/a, we note that with slight modification to the formula, we could obtain a better fit to the experimental data,

$$\tilde{\varepsilon}(\omega) = \varepsilon_r \left(1 - \frac{\tilde{\omega}_p^2}{\omega^2 + i\gamma\omega}\right) + \sum_j i\varepsilon_{pj} \frac{\omega_{Lj}^2 - \omega^2}{\omega_{Tj}^2 - \omega^2 - i\gamma_j\omega} \qquad (2.9)$$

where $\tilde{\omega}_P$ is the effective plasma frequency, ε_r and ε_{pj} are associated with the relative contributions of all of the components, γ is the plasma relaxation rate, ω_{Lj} and ω_{Tj} are the effective longitudinal optical (LO) and transverse optical (TO) frequencies associated with the 'phonon-like' resonant contributions in the effective medium, and γ_j is the relaxation rate (inversely proportional to the linewidth) of the jth resonance. The first term in Eq. (2.9) corresponds to a smooth 'plasma-type' response, and is the only term used in modeling the random arrays (discussed above), while the last (summation) term in Eq. (2.9) corresponds to the discrete resonances associated with the periodic aperture arrays. The modeled ε(ω) of the periodic aperture array using Eq. (2.9) are also shown in Fig. 2.4(b) (blue lines), with fit parameters given in Table 2.2. In fitting the data for the periodic arrays, we used the same effective plasma frequency ($\tilde{\omega}_P$) that we used in

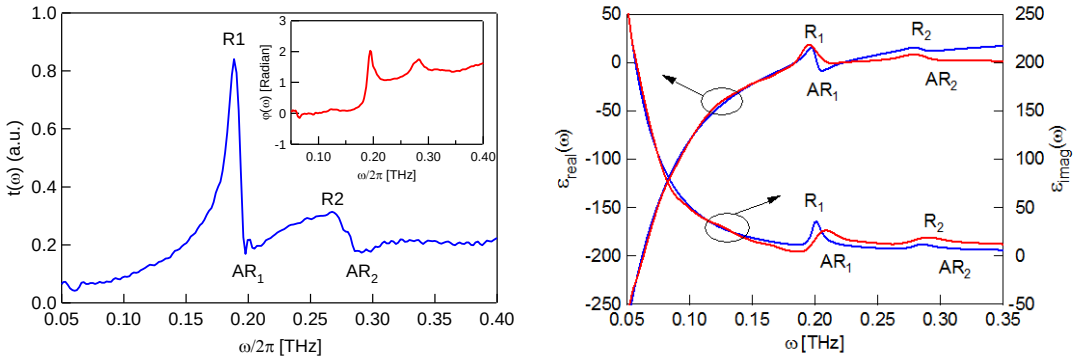

(a) (b)

Figure 2.4. Determination of the real and imaginary components of ε(ω) for the periodic aperture array with D = 750 μm and a = 1.5 mm. (a) The amplitude transmittance t(ω) and phase ϕ(ω) (inset) spectra of the periodic aperture array measured using THz-TDS. The resonance peaks R_j and antiresonance dips AR_j are marked when j is the resonance order. (b) Real and imaginary components of the effective ε(ω) response for the periodic aperture array extracted from the amplitude and phase of t(ω) (red traces) in Fig. 2.4(a). The fit (blue traces) is calculated using Eq. (2.9). The features corresponding to R_j and AR_j are also marked.

Table 2.2. The "best fit" parameters for the effective ε(ω) of periodic aperture arrays with lattice spacing, a = 1.5 mm and diameter, D = 750 μm. The parameters are defined in Eq. (2.9). In the fit, the TO resonant frequencies, ω_{Tj}, were set to the AR frequencies [Eq. (2.8)] in the transmission spectra, while the LO resonant frequencies, ω_{Lj}, were set to the frequencies corresponding to the resonance peaks, R_j.

ε_r	$\tilde{\omega}_p$ (rad/ps)	g (rad/ps)	ε_{p1}	ω_{L1} (rad/ps)	ω_{T1} (rad/ps)	γ_1 (rad/ps)
10.6	0.73	0.35	12	1.19	1.26	0.042
			ε_{p2}	ω_{L2} (rad/ps)	ω_{T2} (rad/ps)	γ_2 (rad/ps)
			1.5	1.68	1.78	0.07

describing ε(ω) of the corresponding random aperture array. The TO frequencies (ω_{T_j}) in the resonant contribution correspond to AR_1 and AR_2 frequencies (Fig. 2.4), which can also be derived from the standard surface plasmon equation [Eq. (2.8)].

With a more careful observation of the individual Fano-resonance, we linked it to more information hidden in the amplitude spectra t(ω) and ϕ(ω). Associated with each resonance, there are two features we would like to point out: one is the sharp antiresonance (AR_i) dip which is closely related to the periodic spacing of the lattice, and the other is the resonance peaks (R_i) on the lower frequency side of the AR_i, where j is the order of the resonance. They both also correspond to the clear features in the ε(ω) spectra [Fig. 2.4(b) (blue lines)]. With a slight modification to the dielectric fitting model, we found that not only the TO resonant frequencies correspond to the AR_j frequencies but also the LO resonance frequencies are close to the R_j frequencies. We also obtained a more matched plot, as shown in Fig. 2.4(b) (red lines).

2.5 Prospective Applications and Possible Future Directions

According to the macroscopic theory of materials and Maxwell's Equation, both the permittivity and permeability of a media could be written as 3×3 matrices which fully present the relations between the components of electric and magnetic fields in the 3-axis coordinate systems. Moreover, if we take the nonlinear effect of materials into consideration, each component in the matrices could include both first order and higher order terms. For example, in the magneto-optic/gyrotropic effect, the permittivity is a 3×3 matrix with off-diagonal components

$$\varepsilon = \begin{bmatrix} \varepsilon'_{xx} & \varepsilon'_{xy} + ig_z & \varepsilon'_{xz} - ig_y \\ \varepsilon'_{yx} - ig_z & \varepsilon'_{yy} & \varepsilon'_{zy} + ig_x \\ \varepsilon'_{zx} + ig_y & \varepsilon'_{yz} - ig_x & \varepsilon'_{zz} \end{bmatrix} \tag{2.10}$$

Using our method, we could fully investigate the ε matrix with the complete measurement of all three components of the electric and magnetic fields. Moreover, we could extend our formula to the periodic aperture arrays in the magneto-optic media and study the influence factor of the gyration vector $\tilde{g}$.

2.6 Conclusion

In summary, we have measured the complex dielectric function ε(ω) at THz frequencies for random and periodic aperture arrays perforated in metallic films. We theoretically analyzed the extraction of the dielectric constants from the transmitted electric fields. From our previous studies, ε(ω) of the random aperture array consists of an effective 'plasma-like' response that is associated with the uncorrelated individual apertures. However, when the apertures are put into a periodic lattice, the discrete resonance oscillations are superimposed with the term of the random array, due to the launched SPP interference related to the reciprocal vectors of the underlying aperture arrays in the Fourier space. Therefore, the dielectric responses could be modeled quantitatively according to the geometric parameters. For instance, the effective plasma frequency is determined by the diameter of the individual apertures, and the transverse optical (TO) frequencies are described by the antiresonance (AR) dip frequencies which are attributed to the periodicity of the lattice. Based on these findings, we further noticed that the resonance peak frequencies should also contribute to the formula model, reflected in the longitudinal optical (LO) frequencies. Owing to this, we also modified the formula

based on the careful observation of the Fano-resonance shape, and obtained a better fit to the experimentally extracted dielectric response. Moreover, we demonstrated the generalized application of this modeling. With a full measurement of all the components of the electric and magnetic fields, the dielectric function, $\varepsilon(\omega)$, could construct a complete model of the plasmonic metamaterials and deepen our understanding of the underlying surface plasmonic mechanisms in a broader field.

2.7 References

1. U. Leonhardt, "Optical conformal mapping," Science **312**, 1777–1780 (2006).
2. J. B. Pendry, D. Schurig, and D. R. Smith, "Controlling electromagnetic fields," Science **312**, 1780–1782 (2006).
3. D. Schurig, J. J. Mock, B. J. Justice, S. A. Cummer, J. B. Pendry, A. F. Starr, and D. R. Smith, "Metamaterial electromagnetic cloak at microwave frequencies," Science **314**, 977–980 (2006).
4. R. Liu, C. Ji, J. J. Mock, J. Y. Chin, T. J. Cui, and D. R. Smith, "Broadband ground-plane cloak," Science **323**, 366–369 (2009).
5. J. Valentine, J. Li, T. Zentgraf, G. Bartal, and X. Zhang, "An optical cloak made of dielectrics," Nat. Mater. **8**, 568–571 (2009).
6. L. H. Gabrielli, J. Cardenas, C. B. Poitras, and M. Lipson, "Silicon nanostructure cloak operating at optical frequencies," Nat. Photonics **3**, 461–463 (2009).
7. M. Rahm, S. A. Cummer, D. Schurig, J. B. Pendry, and D. R. Smith, "Optical design of reflectionless complex media by finite embedded coordinate transformations," Phys. Rev. Lett. **100**, 063903 (2008).
8. D. Schurig, J. B. Pendry, and D. R. Smith, "Transformation-designed optical elements," Opt. Express **15**, 14772–14782 (2007).
9. A. V Kildishev and V. M. Shalaev, "Engineering space for light via transformation optics," Opt. Lett. **33**, 43–45 (2008).
10. M. Rahm, D. Schurig, D. A. Roberts, S. A. Cummer, D. R. Smith, and J. B. Pendry, "Design of electromagnetic cloaks and concentrators using form-invariant coordinate transformations of Maxwell's equations," Photonics Nanostructures - Fundam. Appl. **6**, 87–95 (2008).

11. Y. Luo, H. Chen, J. Zhang, L. Ran, and J. Kong, "Design and analytical full-wave validation of the invisibility cloaks, concentrators, and field rotators created with a general class of transformations," Phys. Rev. B **77**, 125127 (2008).

12. T. Yang, H. Chen, X. Luo, and H. Ma, "Superscatterer: Enhancement of scattering with complementary media," Opt. Express **16**, 18545–18550 (2008).

13. D. A. Roberts, M. Rahm, J. B. Pendry, and D. R. Smith, "Transformation-optical design of sharp waveguide bends and corners," Appl. Phys. Lett. **93**, 251111 (2008).

14. S. Han, Y. Xiong, D. Genov, Z. Liu, G. Bartal, and X. Zhang, "Ray optics at a deep-subwavelength scale: a transformation optics approach," Nano Lett. **8**, 4243–4247 (2008).

15. Y. Lai, J. Ng, H. Chen, D. Han, J. Xiao, Z.-Q. Zhang, and C. Chan, "Illusion optics: The optical transformation of an object into another object," Phys. Rev. Lett. **102**, 253902 (2009).

16. D. R. Smith, J. B. Pendry, and M. C. K. Wiltshire, "Metamaterials and negative refractive index," Science **305**, 788–792 (2004).

17. J. B. Pendry, L. Mart ń-Moreno, and F. J. Garcia-Vidal, "Mimicking surface plasmons with structured surfaces," Science **305**, 847–848 (2004).

18. A. Agrawal, Z. V Vardeny, and A. Nahata, "Engineering the dielectric function of plasmonic lattices," Opt. Express **16**, 9601–9613 (2008).

19. L. Duvillaret, F. Garet, and J.-L. Coutaz, "A reliable method for extraction of material parameters in terahertz time-domain spectroscopy," IEEE J. Sel. Top. Quantum Electron. **2**, 739–746 (1996).

20. F. J. Garcia-Vidal, L. Mart ń-Moreno, and J. B. Pendry, "Surfaces with holes in them: new plasmonic metamaterials," J. Opt. A Pure Appl. Opt. **7**, S97–S101 (2005).

21. T. Matsui, A. Agrawal, A. Nahata, and Z. V. Vardeny, "Transmission resonances through aperiodic arrays of subwavelength apertures.," Nature **446**, 517–521 (2007).

22. T. W. Ebbesen, H. J. Lezec, H. F. Ghaemi, T. Thio, and P. A. Wolff, "Extraordinary optical transmission through subwavelength hole arrays," Phys. Rev. Lett. **391**, 667–669 (1998).

23. W. L. Barnes, A. Dereux, and T. W. Ebbesen, "Surface plasmon subwavelength optics," Nature **424**, 824–830 (2003).

CHAPTER 3

ENGINEERING THE PROPERTIES OF TERAHERTZ FILTERS USING MULTILAYER APERTURE ARRAYS

3.1 Introduction

Technology development within the terahertz (THz) spectral range (1 THz = 10^{12} Hz) has lagged severely behind that of other regions of the electromagnetic spectrum [1,2]. While reasonable progress has been made in developing sources and detectors, other device technologies are still at a rather rudimentary stage [1,2]. A significant reason for this lies in the fact that dielectric materials typically used for passive and active device applications in microwave and optical applications tend to exhibit high loss at THz frequencies. Metals, on the other hand, are highly conductive at these frequencies [3], allowing for low propagation losses. The field of plasmonics [4], and the use of surface plasmon polaritons (SPPs), is therefore particularly attractive for THz device development. As an example, single layer periodic [5] and aperiodic [6] arrays of subwavelength apertures fabricated in metal films have been shown to exhibit resonantly enhanced transmission approaching unity [7,8], even for relatively small fractional aperture areas. Here we show that when two or more aperture arrays are placed in close proximity to one another, new transmission resonances arise that are associated with the gap spacing between the arrays, offering an additional mechanism for tailoring their optical properties. Importantly, proper design of these additional resonances requires that

the complex dielectric response of the single aperture array be determined. Furthermore, with appropriate layer spacing in multilayer structures, we obtained extremely high transmission at the primary resonance frequency, along with substantial suppression of the background transmission increasing the filtering fidelity.

The resonant optical properties of subwavelength aperture arrays (also known as ‘plasmonic lattices’ or ‘plasmonic metamaterials’) have been explained in terms of SPPs that mediate the metal-light interaction via coupling to corrugated metal surfaces [5], where the electromagnetic field associated with the SPPs decays exponentially from the metal-dielectric interface. While the nearly exclusive focus of both theoretical and experimental work has been on the transmission response of single layer plasmonic lattices [9], there have been a number of experimental and theoretical studies of double layer aperture arrays [10–15]. It was found that when the gap spacing, d between the two plasmonic lattices was large, the resulting transmission properties could be obtained by considering each array independently. However, when d becomes sufficiently small, it is expected that the coupling between the SPP waves on the inner, adjacent surfaces of the two layers would yield new and interesting spectral transmission characteristics. Here we show that this coupling forms additional resonances for small values of d that may be used in designing THz filters.

3.2 Experimental Details

We used the aperture arrays, periodic aperture arrays and random aperture arrays, which have the same designs as those in Chapter 2, while here the same type of aperture arrays were put together to form the multilayer aperture arrays. Again, the two-dimensional (2D) aperture arrays were fabricated in 75 μm thick, ~5×5 cm^2 area of

freestanding stainless steel metal foils and have the same fractional aperture area of ~19%. One aperture array pair consisted of 2D periodically spaced circular holes on a square lattice, while the other pair consisted of 2D randomly distributed circular holes. In Fig. 3.1, we show a schematic diagram of the double-layer aperture array with the relevant dimensions.

We used the same setup as in Chapter 2, THz time-domain spectroscopy (THz-TDS), to measure the optical transmission spectra $t(\omega)$ of the perforated metal films, where the THz frequency $\nu = \omega/2\pi$ [7]. A pair of off-axis paraboloidal mirrors was used to collect and collimate the THz radiation from the emitter, which was then normally incident on the aperture array structures. Each array was attached to a solid metal plate with a $5\ \text{cm} \times 5\ \text{cm}$ opening that was placed in the path of the collimated THz beam and placed on a translation stage to vary the distance between the arrays. The 1/e THz beam diameter was smaller than the aperture opening in the metal holders and the spatial extent of the aperture array structures, thereby minimizing edge effects due to the finite size of the array sample. Reference transmission spectra were taken with just the metal holders in the THz beam path using the same setup. The metallic foils were completely opaque prior to fabrication of the arrays. Therefore transmission through the perforated metallic films was uniquely due to the apertures. The detected transient photocurrent was then Fourier transformed and normalized to the reference transmission, yielding the electric field transmission spectrum, $t(\omega)$. THz-TDS allows for the direct measurement of the THz electric field, yielding both amplitude and phase information. By transforming the time-domain data to the frequency domain, we are able to determine independently both the magnitude and phase of the amplitude transmission coefficient, $t(\omega)$, using the

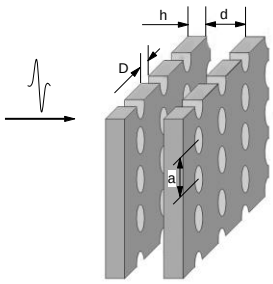

Figure 3.1. Schematic diagram of a double-layer aperture array with aperture diameter, D = 750 μm, periodicity, a =1500 μm, metal film thickness, h = 75 μm and gap spacing, d, taking on values between 0-3000 μm.

relation

$$t(\omega) = |t(\omega)| \exp[i\varphi(\omega)] = \frac{E_{transmitted}(\omega)}{E_{incident}(\omega)} \tag{3.1}$$

In this expression, $E_{incident}$ and $E_{transmitted}$ are the incident and transmitted THz fields, respectively, $|t(\omega)|$ and $\varphi(\omega)$ are the magnitude and phase of the amplitude transmission coefficient, respectively, and $\omega/2\pi$ is the THz frequency.

3.3 Experimental Results, Simulation and Discussion

Figure 3.2 summarizes our experimental studies on the periodically perforated metallic films. Based on the characterization of the single periodic aperture array, this plasmonic lattice with the center-to-center aperture spacing, a = 1.5 mm, forms a lowest order ($\pm$ 1,0) antiresonance (AR) frequency, $\omega(AR_1)/2\pi$ = 0.2 THz and second lowest ($\pm$ 1, $\pm$ 1) AR frequency, $\omega(AR_2)/2\pi$ = 0.28 THz, as shown in Fig. 3.2(a). We have shown previously that the AR feature (i.e., the sharp dip immediately to the right of the resonance peak) is directly related to the underlying structure factor [6]. We note that although the fractional aperture area is only ~19%, the absolute resonant transmission amplitude at the lowest resonance, R_1 is >80%. In Fig. 3.2(b), we show the

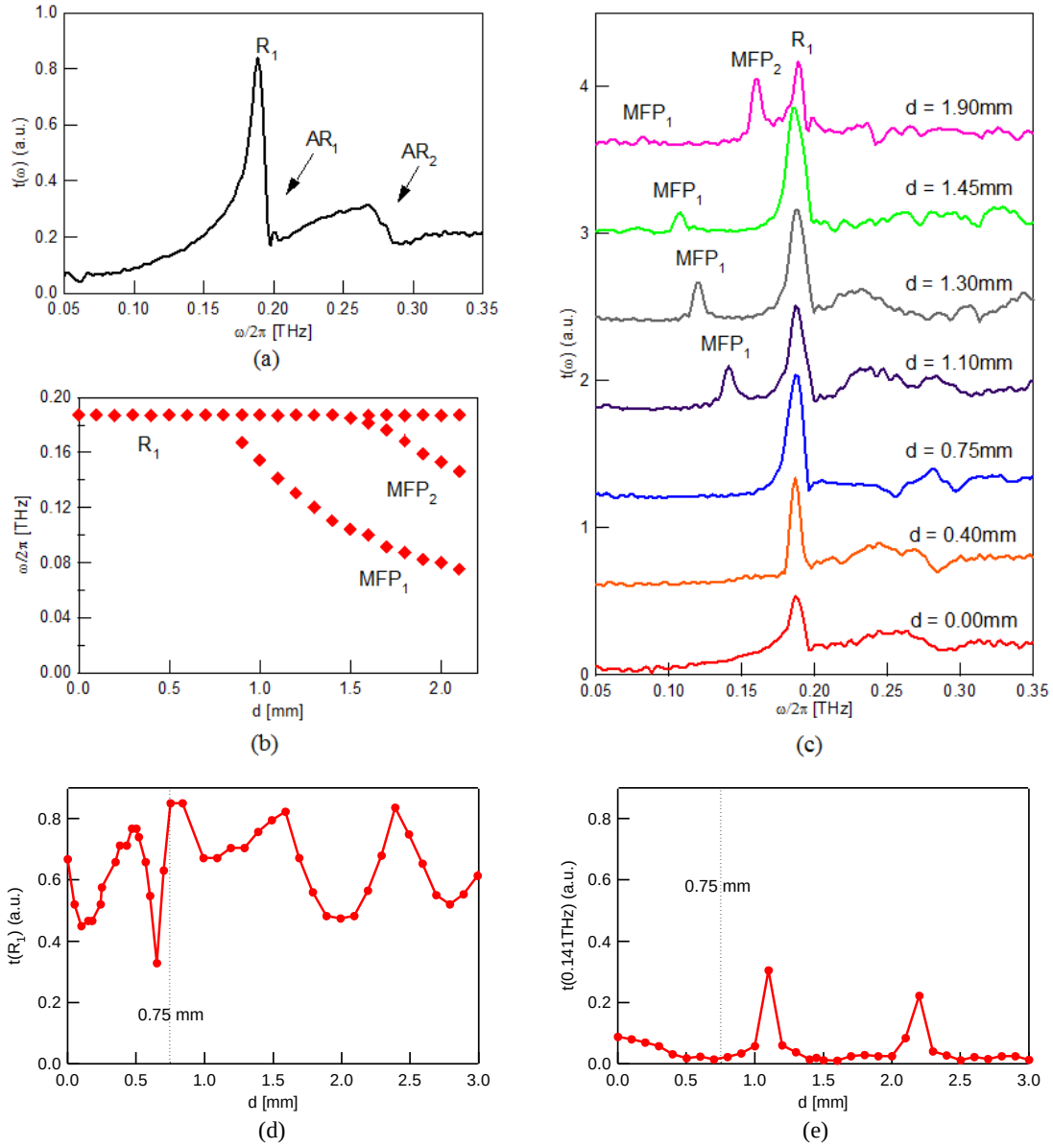

Figure 3.2. THz electric field transmission spectra, t(ω), using a double-layer periodic aperture array. (a) t(ω) of a single-layer periodic aperture array using the parameters given in Fig. 3.1, where the resonances (R_i) and antiresonances (AR_i) are denoted. (b) t(ω) for the double-layer structure as a function of the gap spacing, d. The new transmission bands are labeled MFP_1 and MFP_2 (see text). The plots are vertically offset from the origin in units of 0.6 for clarity. (c) Summary of the experimental resonant frequencies, $\omega/2\pi$, for R_1, MFP_1 and MFP_2 bands in t(ω) as a function of d. (d) Summary of the experimental transmission magnitude t(ω) at the lowest order resonance peak $\omega(R_1)/2\pi$ = 0.1886 THz, as a function of d. (e) Summary of the experimental transmission magnitude t(ω) at an arbitrarily selected frequency $\omega'/2\pi$ = 0.141 THz, as a function of d. In (d) and (e), the red lines between dots are used to guide eyes and the black dotted line indicates the position at d = 0.75 mm.

obtained THz transmission spectra for a double-layer plasmonic lattice structure versus the interlayer spacing, d. The basic features of the transmission spectra can be summarized as follows. For $d \leq d_1 = 0.75$ mm (where $d_1 = a/2$), $t(\omega)$ for the double-layer aperture array is similar to that of the corresponding single aperture array. Specifically, the resonance and antiresonance frequencies of the $(\pm 1,0)$ order resonance are identical for the single and double arrays [Figs. 3.2(a) and (b)], although the double-layer structure exhibits lower overall transmissivity. For values of $d > d_1$, however, we obtain additional transmission resonances in the double-layer array that are not present in the case of a single layer. We label these new resonances, meta-Fabry-Perot (MFP) resonances, as explained below. The new resonance, labeled MFP_1, appears at frequencies $\omega_1/2\pi < \omega(R_1)/2\pi$, and moves progressively to lower frequencies with increasing d. However when $d > d_2 = 1.5$ mm (where $d_2 = a$), we obtain a second new resonance, labeled MFP_2 [Fig. 3.2(b)] whose frequency, $\omega_2/2\pi$, also decreases with d. The various new resonance frequencies are summarized in Fig. 3.2(c). Also, we show the transmission magnitude at $\omega(R_1)/2\pi = 0.1886$ THz and $\omega'/2\pi = 0.141$ THz as a function of d, respectively in Figs. 3.2(d) and 3.2(e). We note that there are rules to follow the cycles, as discussed below.

In order to determine the origin of the additional MFP resonances and understand the underlying mechanisms of the transmission through the double-layer arrays, we perform numerical simulations based on the experimental parameters (Fig. 3.1) and the interlayer spacing, d. Since the MFP resonances emerge at array distances associated with integer values of a/2, namely $d_1 = (a/2)$ and $d_2 = 2(a/2)$, it is reasonable to consider Fabry-Perot reflections as the underlying mechanism. These reflections, however, need to be modified according to the dielectric response of the underlying plasmonic lattice, which

is actually a ‘metamaterial’. In the study of plasmonic lattices, a common approach for determining the transmission resonance frequencies is to use the dielectric properties of the (unperforated) metal film, although this typically yields only approximate resonance frequencies. In Fig. 3.3 we calculate the resulting transmission spectra, taking all Fabry-Perot reflections between the two aperture array films and a numerical resonance spectrum into account, assuming that the dielectric properties of the aperture arrays can be approximated by that of an unstructured metal film at THz frequencies having a dielectric response $\varepsilon \sim -3\times10^4 + i10^6$ [3]. The poor agreement with the experimental results demonstrates that a more sophisticated model for $\varepsilon(\omega)$ response of the plasmonic lattice needs to be considered.

In the last chapter, we extracted the dielectric response of the identical aperture array [Eq. (2.9) and Table 2.2]. Here we calculated the transmission spectra of the double-layer array using the modeled dielectric response [Fig. 3.4(a)], taking multiple reflections into account and assuming a single cycle broadband THz pulse at normal incidence. While contributions from Fabry-Perot reflections typically need to take all four surfaces of the double-layer structure into account, for $d > d_1$ we find that reflections between the inner array surfaces dominate. In Fig. 3.4(b), we show the resulting simulated spectra as a function of d; they are in good agreement with the experimental data. In Fig. 3.4(c), we plot the calculated frequencies associated with the R_1, MFP_1 and MFP_2 resonances as a function of d, and compare these to the experimental frequencies; once again, the excellent agreement between the simulation and experimental data validates our approach. There are a few points to be made here. If we consider Fabry-Perot reflections, when $d < d_1$, the constructive interference should show up above

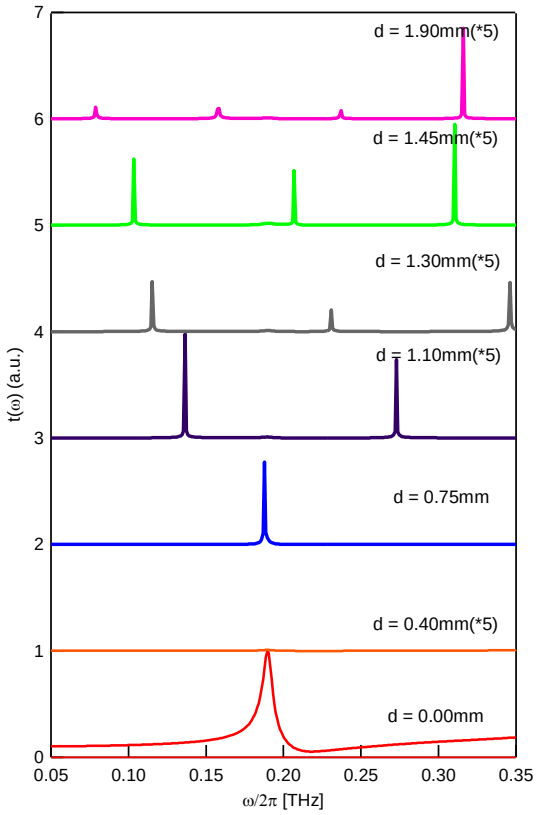

Figure 3.3. Numerical calculations of t(ω) for a double-layer periodic aperture array, assuming that ε(ω) is that of an unperforated metal at THz frequencies ($\varepsilon \sim -3\times10^4 + i10^6$). The spectra are offset from the origin in units of 1 for clarity and scaled to make the features clearer.

Figure 3.4. Numerical calculations of $t(\omega)$ for a double-layer periodic aperture array. (a) Real and imaginary components of the effective $\varepsilon(\omega)$ response for a single-layer periodic aperture array extracted from the amplitude and phase of $t(\omega)$ (red traces). The fit (blue traces) is calculated using Eq. (2.9). (b) Numerical simulation of the transmission spectra for the double-layer structure using the modeled dielectric properties obtained in Fig. 3.4(a). MFP_1, MFP_2 and R_1 resonances are denoted. (c) Summary of the experimental [red diamonds from Fig. 3.2(c)] and calculated (blue triangles) resonant frequencies $\omega/2\pi$ for R_1, MFP_1 and MFP_2 bands in $t(\omega)$ spectra, as a function of d. (d) Summary of the experimental (red trace) and calculated (blue trace) transmission magnitude $t(\omega)$ at the lowest order resonance peak $\omega(R_1)/2\pi$ = 0.1886 THz, as a function of d. (e) Summary of the experimental (red trace) and calculated (blue trace) transmission magnitude $t(\omega)$ at an arbitrarily selected frequency $\omega'/2\pi$ = 0.141 THz, as a function of d. In (d) and (e), the red lines between dots are used to guide eyes and the black dotted line indicates the position at d = 0.75 mm.

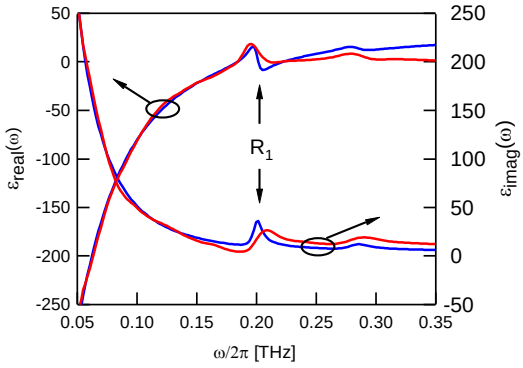
ε_real(ω)
ε_imag(ω)
R1
ω/2π [THz]

(a)

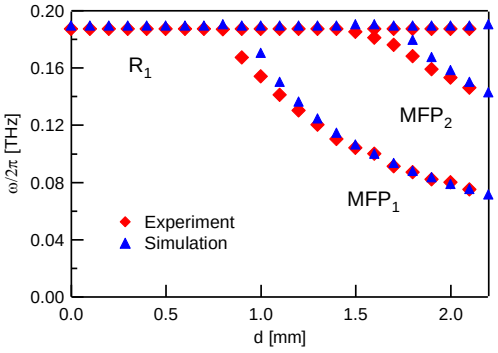
R1
MFP2
MFP1
Experiment
Simulation
ω/2π [THz]
d [mm]

(b)

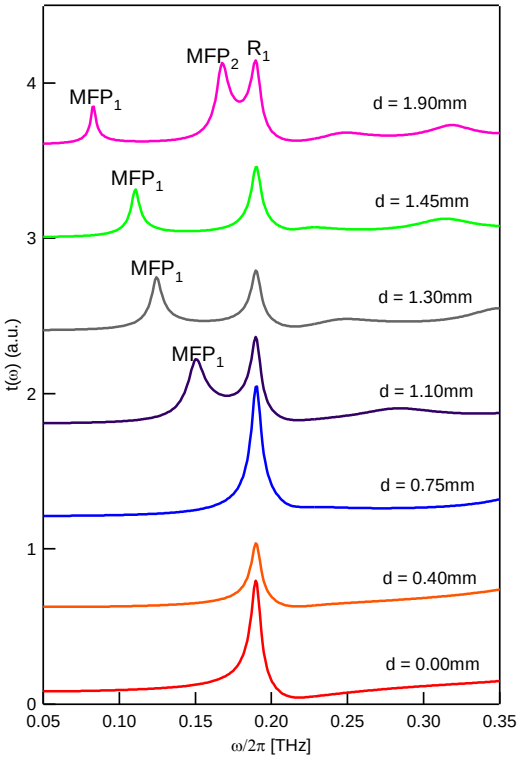
MFP1
MFP2
R1
d = 1.90mm
d = 1.45mm
d = 1.30mm
d = 1.10mm
d = 0.75mm
d = 0.40mm
d = 0.00mm
t(ω) (a.u.)
ω/2π [THz]

(c)

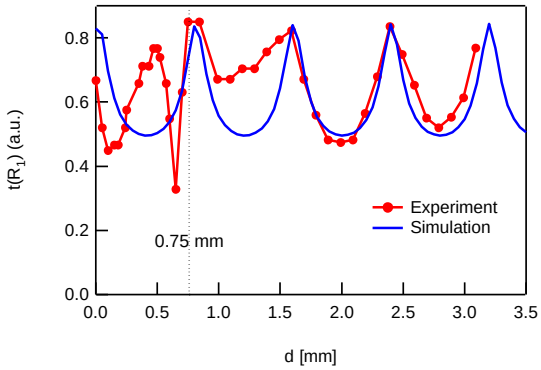
t(R1) (a.u.)
0.75 mm
Experiment
Simulation
d [mm]

(d)

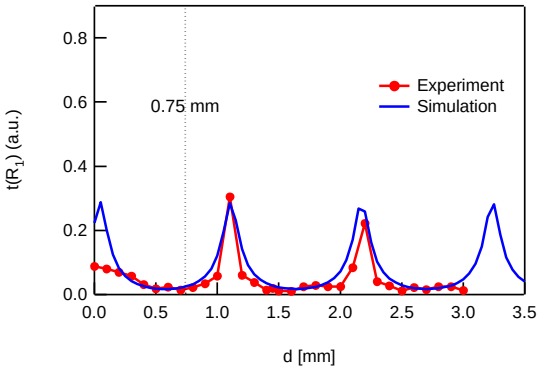
t(R1) (a.u.)
0.75 mm
Experiment
Simulation
d [mm]

(e)

$\omega(AR_1)/2\pi$ = 0.2 THz, or even when $d > d_1$, some of the higher order resonances would show up above 0.2 THz. We can also roughly observe more dips on the right side of the lowest order peak in Fig. 3.2(b). However, the resonances from the constructive interference of the reflected radiation are more obvious when they are situated below the lowest order resonance frequency. However, there should be other mechanisms besides the Fabry-Perot reflections, if we pay attention to the fluctuation trends in Figs. 3.2(d) and 3.2(e). In order to make our finding clearer, we lay the calculated magnitude at the same frequencies atop the plots in Figs. 3.2(d) and 3.2(e), also taking multiple reflections into account, and display them in Figs. 3.4(d) and 3.4(e). Apparently, compared to the regular cycles associated with the calculated plots, the experimental data exhibit cyclical changes when $d > d_1$, but the trend for $d < d_1$ is not regular. We assume that when the two layers are very close, there is coupling between surface waves on the two inner surfaces. This phenomenon leads to more complicated mechanisms and needs greater study.

In order to further demonstrate that the emergence of the MFP transmission resonances can be explained by using the correct complex dielectric function of the perforated metal film rather than the unperforated metallic response, we measured the transmission properties of a commensurate pair of random aperture arrays. First, we show the transmission spectrum of a single random array [Fig. 3.5(a)]. As expected, the transmission spectrum does not show evidence of any resonance, which is consistent with the fact that the Fourier transform of this geometry does not contain any discrete Fourier components. When two such arrays are separated by d, however we observe broad resonances in the otherwise smoothly varying transmission spectrum, as shown in Fig. 3.5(b). Again using the effective $\varepsilon(\omega)$ of the identical array from last chapter [Eq. (2.7)

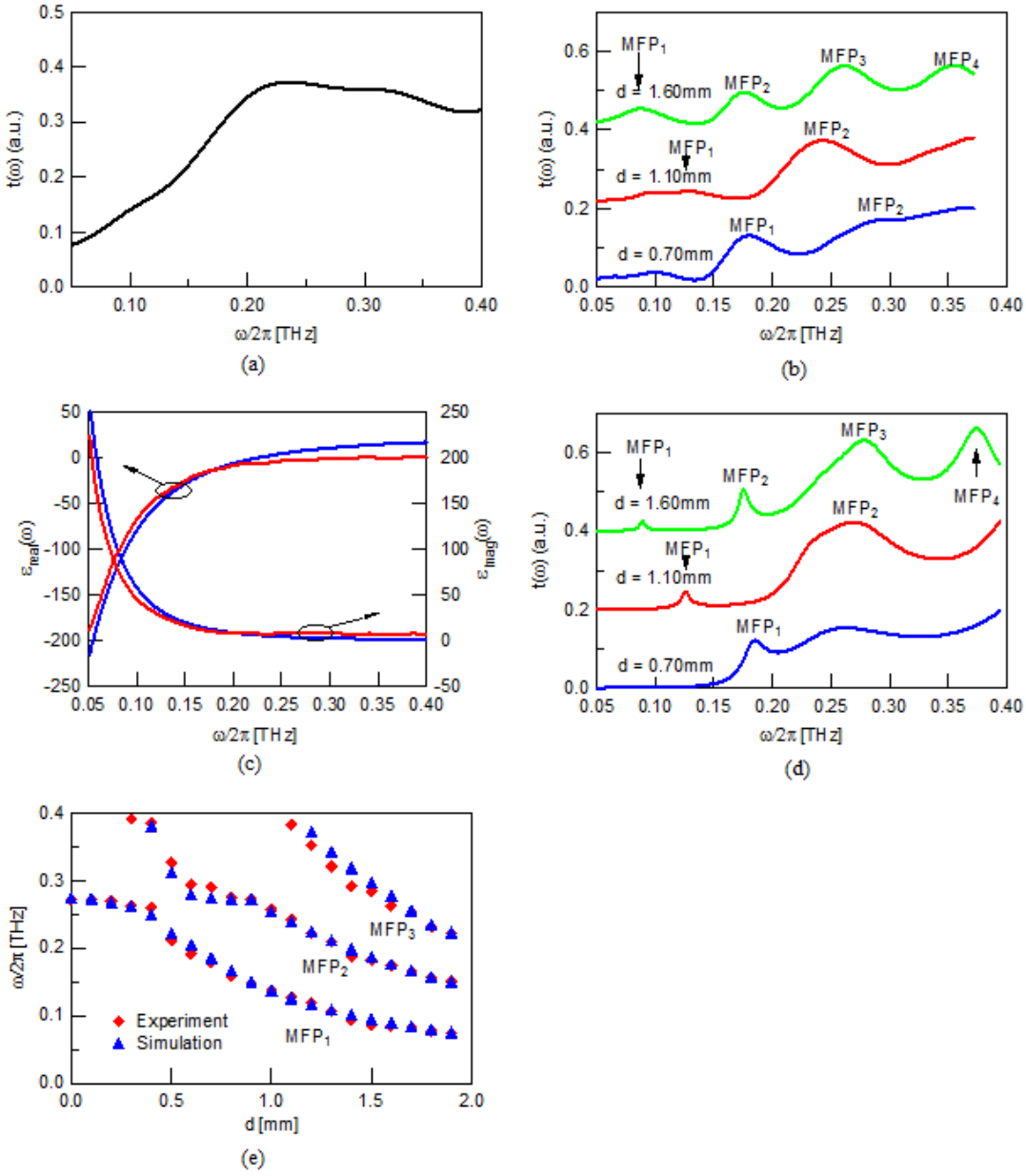

Figure 3.5. Electric field transmission spectra, t(ω), as in Figs. 3.2 and 3.4, but for a commensurate double-layer random hole array with apertures of diameter, D = 750 μm, metal thickness, h = 75 μm and spacing, d that varies between 0-3000 μm. (a) Experimentally measured t(ω) of a single-layer random aperture array. (b) Experimentally measured t(ω) of the double-layer structure for three different values of d. MFP_1 through MFP_4 represent the different orders of MFP resonances. (c) Experimental (red line) and calculated (blue line) real and imaginary ε(ω) components of the individual random array extracted from t(ω) in Fig. 3.5(a). (d) Numerical simulation of t(ω) for the double-layer hole array structure using the same parameters as in Fig. 3.5(c). (e) Summary of the experimental (red diamonds) and calculated (blue triangles) resonant frequencies, ω/2π for the MFP_1 through MFP_4 bands in t(ω) as a function of d.

and Table 2.1], as shown in Fig. 3.5(c), we repeated the simulation mentioned above to obtain t(ω) as a function of d, as shown in Fig. 3.5(d), and summarized in Fig. 3.5(e). We again see excellent agreement between our experimental data and numerical computations. In contrast to what was observed with the periodic arrays, there does not appear to be a minimum d associated with the appearance of MFP resonances. This is consistent with the lack of periodicity in this double-layer structure.

Based on enhancement of resonances between closely spaced aperture arrays, we are now able to extend this general idea for demonstrating highly efficient free-space THz filters, as summarized in Fig. 3.6. In Fig. 3.6(a), we show the transmission properties of a single-layer periodic array and two 0.75 mm thick periodic arrays having d = 0 and d = 0.75 mm, respectively. For d = 0, the double-layer aperture array is equivalent to a single, 1.5 mm thick periodic aperture array. In fact the transmission spectrum is identical to what is observed for a single-layer array, albeit with somewhat reduced amplitude. For d = 0.75 mm, no distinct MFPs are expected. However, since d = 0.75 mm corresponds to a local maxima in t(ω) vs. d for the (± 1,0) resonance [Fig. 3.2(d)], we expect larger transmission compared with that for d = 0. In fact, the R_1 transmission amplitude is nearly identical to that of the single-layer array, although t(ω) at other frequencies above and below the R_1 resonance is dramatically reduced. Similar behavior is expected for other array spacings that correspond to local maxima (i.e., the reflections yield constructive interference). The notion of maintaining high transmission response for the R_1 resonance while reducing the background transmission can be implemented also using multiple arrays.

In this case, the spacing between the arrays is significantly larger (~1 cm), as

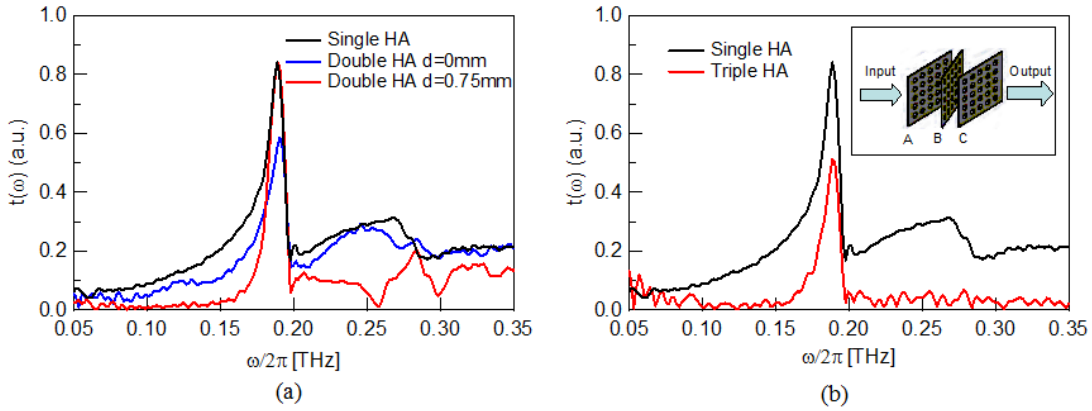

Figure 3.6. t(ω) spectra of multilayer periodic aperture arrays. (a) Comparison between a single-layer structure (black line) and a double-layer structure with spacing d = 0 (blue line) and d = 0.75 mm (red line). (b) Comparison between a single-layer aperture array (black line) and a triple-layer aperture array structure (red line) with d ~ 1 cm. (Inset) Schematic diagram of the triple-layer transmission measurement. The middle plate is rotated from the normal by 5 °.

shown in Fig. 3.6(b). We introduce a small 5 ° rotation in the center array to further minimize the transmission away from the R_1 resonance [16,17]. While the R_1 transmission for the triple array is slightly smaller than that of the single array, the resonance quality factor is higher, and the transmission away from the R_1 resonance is dramatically minimized compared with a single array.

3.4 Conclusion

Our results demonstrate that carefully designed multilayer aperture arrays can allow for two important device capabilities: (1) the introduction of additional resonances associated with the layer spacing, which may be used to generate more complex THz spectral filtering properties, and (2) the ability to create high quality narrow bandpass THz filters. These capabilities were illustrated primarily using double-layer aperture arrays, although multilayer structures may allow for additional refinement of the

transmission properties. In addition, the use of aperiodic geometries [6] as well as conductive nonmetallic materials [18] may allow for greater control over the MFP resonance frequencies, as well as the potential for active THz optoelectronic device applications. Finally, it should be noted that interesting "three dimensional" structures using stacks of aperture array layers in a variety of geometries might give rise to new and interesting optical interference phenomena.

3.5 References

1. M. Tonouchi, "Cutting-edge terahertz technology," Nat. Photonics **1**(2), 97–105 (2007).

2. B. Ferguson and X.-C. Zhang, "Materials for terahertz science and technology," Nat. Mater. **1**(1), 26–33 (2002).

3. M. A. Ordal, L. L. Long, R. J. Bell, S. E. Bell, R. R. Bell, R. W. Alexander, Jr., and C. A. Ward, "Optical properties of the metals Al, Co, Cu, Au, Fe, Pb, Ni, Pd, Pt, Ag, Ti, and W in the infrared and far infrared," Appl. Opt. **22**(7), 1099–1020 (1983).

4. W. L. Barnes, A. Dereux, and T. W. Ebbesen, "Surface plasmon subwavelength optics," Nature **424**(6950), 824– 830 (2003).

5. T. W. Ebbesen, H. J. Lezec, H. F. Ghaemi, T. Thio, and P. Wolff, "Extraordinary optical transmission through sub-wavelength hole arrays," Nature **391**(6668), 667–669 (1998).

6. T. Matsui, A. Agrawal, A. Nahata, and Z. V. Vardeny, "Transmission resonances through aperiodic arrays of subwavelength apertures," Nature **446**(7135), 517–521 (2007).

7. H. Cao and A. Nahata, "Resonantly enhanced transmission of terahertz radiation through a periodic array of subwavelength apertures," Opt. Express **12**(6), 1004–1010 (2004).

8. J. W. Lee, M. A. Seo, J. Y. Sohn, Y. H. Ahn, D. S. Kim, S. C. Jeoung, Ch. Lienau, and Q.-H. Park, "Invisible plasmonic meta-materials through impedance matching to vacuum," Opt. Express **13**(26), 10681–10687 (2005).

9. F. J. Garcia-Vidal, T. W. Ebbesen, and L. Kuipers, "Light passing through subwavelength apertures," Rev. Mod. Phys. **82**(1), 729–787 (2010).

10. A. P. Hibbins, J. R. Sambles, C. R. Lawrence, and J. R. Brown, "Squeezing

millimeter waves into microns," Phys. Rev. Lett. **92**(14), 143904 (2004).

11. H. B. Chan, Z. Marcet, K. Woo, D. B. Tanner, D. W. Carr, J. E. Bower, R. A. Cirelli, E. Ferry, F. Klemens, J. Miner, C. S. Pai, and J. A. Taylor, "Optical transmission through double-layer metallic subwavelength slit arrays," Opt. Lett. **31**(4), 516–518 (2006).

12. F. Miyamaru and M. Hangyo, "Anomalous terahertz transmission through double-layer metal hole arrays by coupling of surface plasmon polaritons," Phys. Rev. B **71**(16), 165408 (2005).

13. Y. H. Ye and J. Y. Zhang, "Enhanced light transmission through cascaded metal films perforated with periodic hole arrays," Opt. Lett. **30**(12), 1521–1523 (2005).

14. H. Li, S. Xie, R. Zhou, Q. Liu, X. Zhou, and M. Yuan, "Two different transmission tunnels of light through double-layer gold nanohole arrays," J. Phys. Condens. Matter **20**(41), 415223 (2008).

15. R. Ortuño, C. García-Meca, F. J. Rodríguez-Fortuño, J. Martí, and A. Martínez, "Role of surface plasmon polaritons on optical transmission through double layer metallic hole arrays," Phys. Rev. B **79**(7), 075425 (2009).

16. A. Agrawal, Z. V. Vardeny, and A. Nahata, "Engineering the dielectric function of plasmonic lattices," Opt. Express **16**(13), 9601–9613 (2008).

17. T. D. Nguyen, A. Nahata, and Z. V. Vardeny, "THz anomalous transmission in plasmonic lattices: incidence angle dependence," Proc. SPIE **7394**, 73940H (2009).

18. T. Matsui, Z. V. Vardeny, A. Agrawal, A. Nahata, and R. Menon, "Resonantly-enhanced transmission through a periodic array of subwavelength apertures in heavily-doped conducting polymer films," Appl. Phys. Lett. **88**(7), 071101 (2006).

CHAPTER 4

TERAHERTZ PLASMONIC PROPERTIES OF HIGHLY ORIENTED PYROLYTIC GRAPHITE

4.1 Introduction

The many different allotropes of carbon are fascinating in that they can possess remarkably different transport and optical properties. Among the various allotropes, graphene has elicited the most interest in recent years. Single layer graphene exhibits a constant 2.3% absorption at normal incidence, and its infrared absorption can be tuned by electrically tuning the Fermi level [1–3]. While a number of interesting device implementations have been demonstrated recently using graphene [3–7], the high transmissivity of graphene limits its utility in terahertz (THz) plasmonics applications.

Multilayer graphene, in the form of graphite, is perhaps the most common allotrope of carbon and is readily available in thick film form. In fact, the optical properties of graphite have been well studied across the entire electromagnetic spectrum [8–12]. However reflection measurements are usually required because of the highly absorbing nature of graphite, which arises from its unique electronic properties, where the intraband and interband optical transitions within the p electron band extend up to 7 eV [8]. In these measurements, since only the reflected optical power is readily measured, Kramers-Kronig (K-K) relations are necessary to compute the complex dielectric constant $\varepsilon(\omega)$. Given the limitations in spectral measurements, the use of such a

transformation often yields data that have limited accuracy. Despite the strong interest in the optical properties of graphite over the years, optical studies using transmission spectroscopy through thin graphite films, which yields a more accurate $\varepsilon(\omega)$, have not been demonstrated.

Within the field of plasmonics, the phenomenon of enhanced optical transmission (EOT) through perforated metal films with periodic subwavelength hole arrays (HAs) [or plasmonic lattices] has also been extensively studied over the last two decades [13–15]. The EOT spectrum consists of a number of relatively sharp resonances and correlated antiresonance features, which are closely related with the reciprocal vectors in the HA structure factor [15]. The EOT resonances are more pronounced for good conductors such as silver and gold at visible frequencies. However at THz frequencies, even relatively poor metals such as stainless steel [15] and lead [16] have very high THz conductivities and therefore support surface plasmon polariton (SPP) excitations, a precursor for obtaining EOT through the perforated film. In fact, a broad range of exotic metals that include heavily doped conducting polymers [17] and one dimensional multiwalled carbon nanotube sheets [18] have been found to support relatively low loss SPP propagation and thus may be useful for THz optoelectronics technology in the near future.

We characterized the THz optical spectra of a thin highly oriented pyrolytic graphite (HOPG) film using THz time-domain spectroscopy (THz-TDS). Using incident radiation that was polarized perpendicular to the c axis of the graphite film, we obtained the complex $\varepsilon(\omega)$ spectrum of the material without the need for K-K approximations. This was possible because the THz electric field was measured in this type of

spectroscopy, which yielded both the transmission amplitude and phase spectra. The graphite plasma frequency, ν_p = 34 THz, was obtained by simultaneously fitting the real ε'(ω) and imaginary ε"(ω) part of the dielectric constant ε(ω) [= ε'(ω) + iε"(ω)] using the Drude model approximation, in agreement with the theoretical value. We also studied THz EOT through perforated graphite films with periodic subwavelength HAs and showed that graphite supports SPP excitations. The "effective" dielectric constant ε*(ω) of the obtained plasmonic lattice was investigated in comparison with ε*(ω) of a corresponding stainless steel plasmonic lattice. From this comparison we concluded that despite the fact that graphite exhibits a lower conductivity compared to that of conventional metals such as stainless steel, the transmission properties of their plasmonic lattice structures are, in fact, similar in nature.

4.2 Experimental Details, Results and Discussion

The HOPG with dimension of 10mm×10mm×1mm was purchased from SPI Supplies. It is a relatively new form of high purity graphite that consists of a lamellar structure of stacked graphene planes, which yields the relatively easy "exfoliation properties" of the material. The reported intraplane electrical resistivity is $\rho = \sim 4 \times 10^{-5}$ Ωcm, whereas the interplane ρ = ~0.2 Ωcm; four orders of magnitude difference in ρ shows the known marked anisotropic physical properties of the graphite. Graphite has a relatively low carrier density of $\sim 10^{19}$ cm^{-3} at room temperature because of its semimetal characteristics [19]. In order to obtain a thin graphite film, we used the well-developed scotch tape technique with a smooth surface; this method formed films of ~7-10 μm thick and 1×1cm^2 area. The film roughness was measured by a profilometer to be on the order of a few tens of nanometers. For the graphite HA fabrication, we used an excimer laser to

mill holes in the graphite sheets. We fabricated a 12×12 square HA structure that consisted of 0.3mm diameter circular holes having lattice constant (or nearest neighbor hole distance) a = 0.7mm.

We used a THz-TDS setup for measuring the optical transmission spectra t(ω) of the unperforated and perforated graphite films. Photoconductive devices were utilized for both emission and coherent detection of the THz field (see the detail in Ref. [15]). The detected transient photocurrent PC(τ) was recorded as a function of the pump/probe translation stage path that determined the time delay, τ, between the "pump" beam that hits the emitter and the "probe" beam that arrives at the detector. PC(τ) was subsequently Fourier transformed and normalized to a reference transmission, yielding both the electric field transmission amplitude and phase t(ω) in the spectral range of ~0.1 THz–0.5 THz for the plasmonic lattice measurements, and 0.4 THz–1.8 THz for the unperforated films. These different spectral ranges were obtained using different THz systems, which were required because of the significantly different transmission properties of the two types of structures. The resulting Fourier transformed data were described by the relation

$$t(\omega) = |t(\omega)| \exp[i\varphi(\omega)] = \frac{E_{transmitted}(\omega)}{E_{incident}(\omega)}. \qquad (4.1)$$

In this expression $E_{incident}$ and $E_{transmitted}$ are the incident and transmitted THz fields, respectively, and the respective |t(ω)| and φ(ω) are the amplitude and phase of the transmission. From t(ω) both real and imaginary components of the refractive index $n_{complex}(\omega)$ can be directly obtained without the need for K-K approximations, where somewhat arbitrary assumptions about asymptotic behavior are typically made.

We first present the obtained transmission spectra of a ~7.5 μm thick HOPG film, where the THz beam polarization is perpendicular to the graphite c axis. The Fourier

transform of the transmission in the time domain (not shown here) yields the transmission amplitude and phase spectra shown in Fig. 4.1(a). Since the graphite film is quite thick, a small transmission of less than ~0.4% was obtained in the THz range. Based on the fact that a single layer graphene sheet exhibits a constant transmission of ~98% [1,2], we estimate that our HOPG film consists of about a thousand graphene layers, in fair agreement with the estimated film thickness. From the obtained transmission amplitude and phase spectra, we could readily calculate the complex index of refraction $n_{complex}(\omega)$ spectrum $n(\omega) + i\kappa(\omega)$, as shown in Fig. 4.1(b). Both n and κ increase at low frequencies, in agreement with previous measurements of the graphite refractive index obtained using reflectivity measurements [12]. The absorption coefficient spectrum is given by the relation $\alpha(\nu) = 2\pi\nu\kappa(\nu)/c$, where the electric field decay is given by $\exp[-\alpha(\nu)d])$, ν is the THz frequency, and c is the speed of light in a vacuum. Based on the data in Fig. 4.1(b), $\alpha(\nu)$ increases at low photon energy, which is also in agreement with previous studies [12].

Next we calculated both $\varepsilon'(\omega)$ and $\varepsilon''(\omega)$ spectra from $n(\omega)$ and $\kappa(\omega)$ spectra, as shown in Fig. 4.2. In order for a medium to support SPP excitations, it is necessary that $\varepsilon'(\omega)$ $(= n^2 - \kappa^2)$ be negative [20]. Based on the spectrum in Fig. 4.2, $\varepsilon'(\omega)$ is indeed negative over the entire THz spectral range studied here, demonstrating that SPPs may be supported in our HOPG film. To obtain the plasma frequency of the HOPG film, we simultaneously fit $\varepsilon'(\omega)$ and $\varepsilon''(\omega)$ spectra using the Drude model for the conductivity of carriers subjected to the momentum relaxation rate γ:

$$\tilde{\varepsilon}(\omega) = \varepsilon_{\infty}\left(1 - \frac{\tilde{\omega}_p^2}{\omega^2 + i\gamma\omega}\right), \tag{4.2}$$

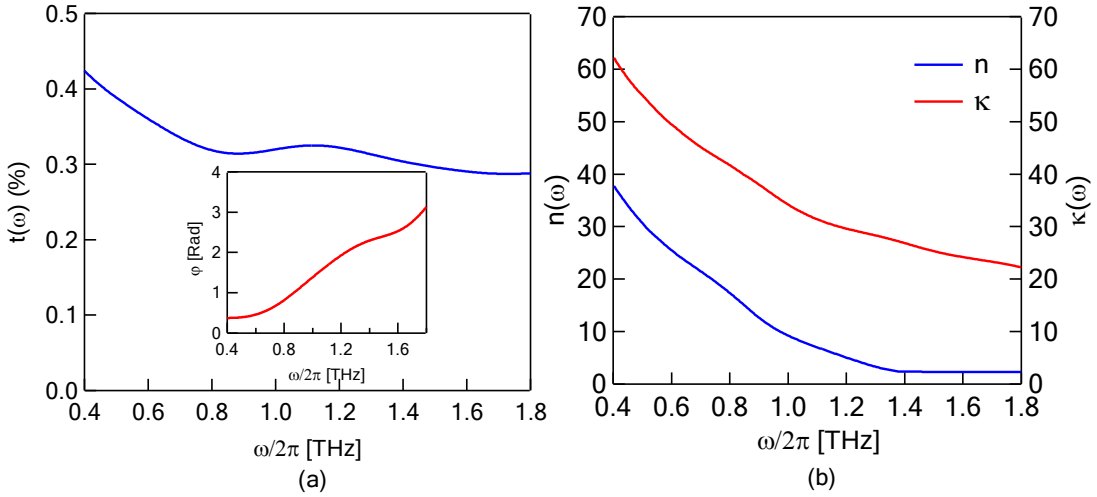

Figure 4.1. Transmission properties of a ~7.5 μm thick HOPG film obtained from THz time domain measurements. (a) The spectra of the THz electric field transmission amplitude t(ω) (blue) and phase φ(ω) (red, inset) through the graphite film. (b) The complex refractive index spectra, n(ω) and κ(ω), of the graphite film obtained from the data in Fig. 4.1(a).

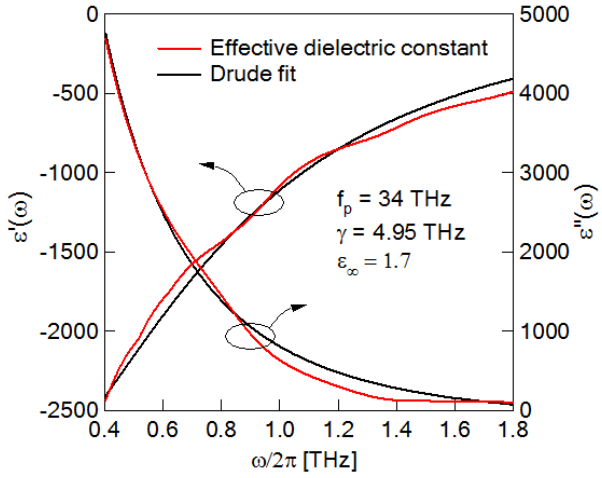

Figure 4.2. The real ε'(ω) and imaginary ε"(ω) components (red lines) of the graphite complex dielectric constant, obtained from the data in Fig. 4.1. The black lines show the best fit of the data using a Drude model approximation [Eq. (4.2)], where the fit parameters are noted.

where $\omega = 2\pi\nu$, ε_∞ is ε' at high frequency, and ω_p is the plasma frequency of the material. Figure 4.2 shows the best fit of $\varepsilon(\omega)$ using the Drude model [Eq. (4.2)], where the fitting parameters are all provided in the figure. The best-fit plasma frequency is ω_p = 213.6 rad/ps (corresponding to ν_p = 34 THz or 136 meV), which is more than a factor of 40 smaller than the plasma frequency of typical metals such as Al and Ag. The reason for the small ω_p is that graphite has a significantly smaller carrier density $N \sim 10^{19}/cm^3$ due to its semimetal characteristics. Our fitted plasma frequency is in good agreement with some values reported in the literature [19,21]. We note that in spite of the complicated graphite band structure at the Fermi energy, the obtained ω_p is consistent with the simple plasma frequency formula, namely $\omega_p = (4\pi Ne^2/m^*\varepsilon)^{1/2}$, taking into account the graphite DC dielectric constant ε and an effective electron mass $m^* \sim 0.1m_e$.

It is interesting to study SPP propagation in graphite, where the conductivity anisotropy is large. A simple way to study this is via the EOT spectrum on a perforated graphite sheet, since SPP propagation is needed for the transmission enhancement. Figure 4.3(a) shows the THz transmission spectrum through a graphite plasmonic lattice having a hole diameter D = 0.3 mm and lattice constant a = 0.7 mm. The occurrence of EOT resonances confirms that graphite indeed supports SPPs due to its "metallic properties." For comparison, we fabricated an identical plasmonic lattice on a stainless steel foil and studied its THz transmission [Fig. 4.3(a)]. Comparing the EOT spectra of the two plasmonic lattices, Figure 4.3(a) clearly shows that the low energy antiresonance feature occurs exactly at the same frequency $\nu_{ar} \sim$ 0.43 THz. This is the expected frequency for the (1,0) plasmonic lattice mode that corresponds to the plasmonic lattice constant a = 0.7 mm, with $\nu_{ar} = c/a$. However, as clearly seen in Fig. 4.3(a), the graphite (1,0) resonance is

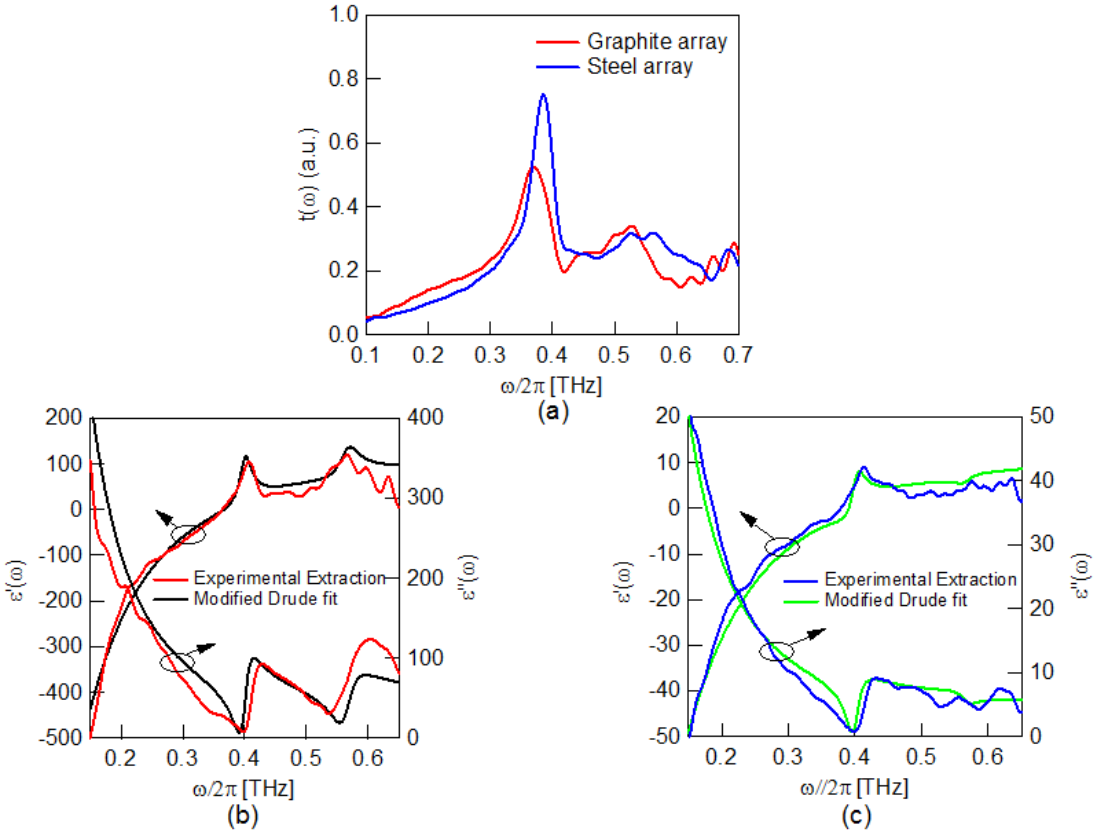

Figure 4.3. THz transmission properties of a periodic hole array having lattice constant a = 0.7 mm and hole diameter D = 0.3 mm fabricated on films of graphite and stainless steel. (a) The THz electric field transmission spectra t(ω) of the graphite hole array (red line) and the stainless steel hole array (blue line). (b), (c) The effective dielectric spectra ε*(ω) obtained from the transmission spectra in Fig. 4.3(a), where the red lines are the effective dielectric constants of the graphite hole array and the blue lines are those of the stainless steel hole array. The black and green lines show the best fits using the effective dielectric constant model [Eq. (4.3)]; the fit parameters are given in Table 4.1.

weaker and broader than that in the stainless steel and, in addition, is red-shifted compared to the stainless steel resonance. These differences in the resonant mode are probably due to different strengths of the SPP loss in the two materials [17], which determines the resonance shape. The higher loss in the graphite film may be due to its poorer metallic properties and small intraplane conductivity that results in larger skin depth.

In order to more quantitatively compare the EOT spectra of the two fabricated plasmonic lattices, we studied the effective complex dielectric constant ε*(ω) of the graphite and stainless steel HA structures. Figures 4.3(b) and 4.3(c) show the real and imaginary components of ε*(ω) in graphite and stainless steel HAs calculated from the amplitude and phase of their respective EOT spectra, obtained the same way as for the unperforated graphite film discussed above. It is clear that ε*(ω) spectra are similar in the two plasmonic lattices, even though the optical properties of graphite and stainless steel are very different from each other. Using the theoretical approach that is described in Chapter 2, we modeled ε*(ω) spectra of the two plasmonic lattices using the following formulae [20]:

$$\tilde{\varepsilon}^{*}(\omega)=\varepsilon_{r}^{*}\left(1-\frac{\left(\tilde{\omega}_{p}^{*}\right)^{2}}{\omega^{2}+i\gamma^{*}\omega}\right)+\sum_{j} i\varepsilon_{pj}^{*}\frac{\left(\omega_{Lj}^{*}\right)^{2}-\omega^{2}}{\left(\omega_{Tj}^{*}\right)^{2}-\omega^{2}-i\gamma_{j}^{*}\omega}, \tag{4.3}$$

where ε_{r}^{*}, γ^{*} and $\tilde{\omega}_{p}^{*}$ are the effective parameters that correspond to the Drude model [Eq. (4.2)] and ε_{pj}^{*} are associated with the relative contributions of each of the EOT resonances. As discussed in Ref. [20], ω_{Lj}^{*} and ω_{Tj}^{*} in Eq. (4.3) are the respective longitudinal and transverse frequencies of the resonant mode j, analogous to phonon and

exciton contributions in semiconductors to ε(ω) at resonance conditions. The fit of ε*(ω) using Eq. (4.3) is shown in Figs. 4.3(b) and 4.3(c) for the graphite and stainless steel plasmonic lattice, respectively, whereas the best fit parameters are given in Table 4.1. Surprisingly, most of the fit parameters in the two plasmonic lattices are similar; this shows that the plasmonic lattices in the THz range are not very sensitive to the underlying metal. The exception is the ε_r^* parameter, where ε_r^* for graphite is an order of magnitude larger than in stainless steel. The reason for that is not clear at the present time.

4.3 Conclusion

We investigated the THz transmission through a ~7.5 μm thick HOPG film using THz time-domain spectroscopy with the incident radiation polarized perpendicular to the graphite c axis. We obtained the complex refraction index and ε(ω) spectra using the measured transmission amplitude and phase, without the need of Kramer-Kronig transformations and related approximations. The ε(ω) spectrum was fit with the Drude model, from which we obtained the graphite plasma frequency ν_p = 34 THz; this value is consistent with the low carrier density of graphite at room temperature. Despite the low plasma frequency, graphite clearly supports SPP excitations in the THz spectral range. To prove this we perforated the graphite film with periodic subwavelength HAs and measured resonant enhanced transmission, which arise from interference between SPPs on the film surfaces. Although graphite exhibits a lower conductivity than other conventional metals such as stainless steel, the resonant transmission properties are similar in nature. This demonstrates that a broad range of similar materials may be useful for THz plasmonic applications.

Table 4.1. The best fit parameters of the effective dielectric to describe the enhanced THz transmission spectrum in graphite and stainless steel plasmonic lattices. Description of the various parameters is given in the text. Except for ε_r^* and ε_{pj}^*, all other parameters are given in units of rad/ps.

Material	ε_r^*	$\widetilde{\omega}_p^*$	γ^*	ε_{p1}^*	ω_{L1}^*	ω_{T1}^*	γ_1^*	ε_{p2}^*	ω_{L2}^*	ω_{T2}^*	γ_2^*
Graphite	130	2.39	0.65	30	2.26	2.51	0.15	30	3.31	3.55	0.25
Stainless Steel	15	2.39	0.7	7	2.45	2.51	0.15	1	3.69	3.55	0.2

4.4 References

1. R. R. Nair, P. Blake, A. N. Grigorenko, K. S. Novoselov, T. J. Booth, T. Stauber, N. M. R. Peres, and A. K. Geim, "Fine structure constant defines visual transparency of graphene," Science **320**(5881), 1308 (2008).

2. K. F. Mak, M. Y. Sfeir, Y. Wu, C. H. Lui, J. A. Misewich, and T. F. Heinz, "Measurement of the optical conductivity of graphene," Phys. Rev. Lett. **101**, 196405 (2008).

3. Y. Zhang, T.-T. Tang, C. Girit, Z. Hao, M. C. Martin, A. Zettl, M. F. Crommie, Y. R. Shen, and F. Wang, "Direct observation of a widely tunable bandgap in bilayer graphene," Nature (London) **459**, 820–823 (2009).

4. F. Rana, "Graphene terahertz plasmon oscillators," IEEE Trans. Nanotechnol. **7**(1), 91–99 (2008).

5. M. Liu, X. Yin, E. Ulin-Avila, B. Geng, T. Zentgraf, L. Ju, F. Wang, and X. Zhang, "A graphene-based broadband optical modulator," Nature (London) **474**, 64–67 (2011).

6. H. Yan, X. Li, B. Chandra, G. Tulevski, Y. Wu, M. Freitag, W. Zhu, P. Avouris, and F. Xia, "Tunable infrared plasmonic devices using graphene/insulator stacks," Nat Nanotechnol. **7**, 330–334 (2012).

7. B. Sensale-Rodriguez, R. Yan, M. M. Kelly, T. Fang, K. Tahy, W. S. Hwang, D. Jena, L. Liu, and H. G. Xing, "Broadband graphene terahertz modulators enabled by intraband transitions," Nature Commun. **3**, 780 (2012).

8. E. A. Taft and H. R. Philipp, "Optical properties of graphite," Phys. Rev. **138**(1A), A197–A202 (1965).

9. L. G. Johnson and G. Dresselhaus, "Optical properties of graphite," Phys. Rev. B **7**(6), 2275–2285 (1973).

10. T. Uda, "Optical properties of graphite in the far-infrared region," J. Phys. Soc. Jpn. **28**(4), 946–954 (1970).

11. G. Ramakrishnan, R. Chakkittakandy, and P. C. M. Planken, "Terahertz generation from graphite," Opt. Express **17**(18), 16092–16099 (2009).

12. A. B. Djurišić and E. H. Li, "Optical properties of graphite," J. Appl. Phys. **85**(10), 7404–7410 (1999).

13. T. W. Ebbesen, H. J. Lezec, H. F. Ghaemi, T. Thio, and P. A. Wolff, "Extraordinary optical transmission through sub-wavelength hole arrays," Nature (London) **391**, 667–669 (1998).

14. J. B. Pendry, L. Mart ń-Moreno, and F. J. Garcia-Vidal, "Mimicking surface plasmons with structured surfaces," Science **305**(5685), 847–848 (2004).

15. T. Matsui, A. Agrawal, A. Nahata, and Z. V. Vardeny, "Transmission resonances through aperiodic arrays of subwavelength apertures," Nature (London) **446**(7135), 517–521 (2007).

16. T. D. Nguyen, Z. V. Vardeny, and A. Nahata, "Concentration of terahertz radiation through a conically tapered aperture," Opt. Express **18**(24), 25441–25448 (2010).

17. T. Matsui, Z. V. Vardeny, A. Agrawal, A. Nahata, and R. Menon, 'Resonantly-enhanced transmission through a periodic array of subwavelength apertures in heavily-doped conducting polymer films," Appl. Phys. Lett. **88**(7), 071101 (2006).

18. T. D. Nguyen, S. Liu, M. D. Lima, S. Fang, R. H. Baughman, A. Nahata, and Z. V. Vardeny, "Terahertz surface plasmon polaritons on freestanding multi-walled carbon nanotube aerogel sheets," Opt. Mater. Express **2**(6), 782–788 (2012).

19. C. A. Klein and W. D. Straub, "Carrier densities and mobilities in pyrolytic graphite," Phys. Rev. **123**(5), 1581–1583 (1961).

20. A. Agrawal, Z. V. Vardeny, and A. Nahata, "Engineering the dielectric function of plasmonic lattices," Opt. Express **16**(13), 9601–9613 (2008).

21. H. R. Philipp, "Infrared optical properties of graphite," Phys. Rev. B **16**(6), 2896–2900 (1977).

CHAPTER 5

TERAHERTZ SURFACE PLASMON POLARITONS ON FREESTANDING MULTIWALLED CARBON NANOTUBE AEROGEL SHEETS

5.1 Introduction

Carbon nanotubes (CNTs) have attracted significant attention because of their unique electrical, optical and mechanical properties [1–3]. Recently, there has been growing interest in studying the physical properties of highly aligned carbon nanotube sheets [3–9]. A unique aspect of these materials is the fact that this structure has high electrical and optical anisotropy that results from their large aspect ratio, making CNTs a nearly ideal quasi-one-dimensional system. This anisotropy manifests itself in numerous different ways. For example, ellipsometry measurements at optical frequencies have demonstrated the highly anisotropic nature of the dielectric constants and conductivities of aligned CNTs [9,10]. The polarized absorption of single-walled carbon nanotubes (SWCNTs) have been reported, which has allowed for the determination of the nematic order parameters of the sample [11]. The polarization-dependent Raman scattering measurements of substantially aligned SWCNT fibers showed dramatic reduction of the Raman intensities in all spectra for the perpendicular excitation compared to those in parallel excitation, while the relative intensities of the radial and the tangential modes remained unchanged [12]. In measurements of the anisotropic conductivity of SWCNT

films [4–6] and multiwalled CNT (MWCNT) films [7], it was found that it follows a Drude-like behavior for lossy metals at THz frequency. In both materials, however, the samples were prepared on glass slides or Si wafers. This ambient environment may affect the optical and electrical properties of the materials.

We characterized the THz optical spectra of free standing MWCNT films using terahertz time-domain spectroscopy (THz-TDS) for incident radiation polarized parallel and perpendicular to the nanotube axis. While there was strong anisotropy in the extracted dielectric constants, the medium exhibited metallic behavior for both orientations, which was a necessary condition for supporting surface plasmon-polaritons (SPPs). Based on this finding, we fabricated an array of subwavelength apertures in 25 μm and 60 μm thick sheets of MWCNTs. In the case of the thinner CNT sheet, we observed enhanced optical transmission [13,14] only when the incident radiation was polarized parallel to the CNT axis. However, for the slightly thicker sheet, we did not observe enhanced transmission with either orientation. This suggested that absorption within the apertures was significant in this material.

5.2 Experimental Details

A MWCNT 'forest' was synthesized by catalytic chemical vapor deposition [3]. The CNT sheet was drawn from a sidewall of the forest on steel washers with an inner diameter of ~2 cm. Multiple forest-drawn MWCNT films can be made by stacking together parallel sheets so that the nanotubes are oriented parallel to each other. The CNT sheet thickness was determined by counting the number of layers. We studied two different MWCNT sheets: a 25 μm thick sheet having 12 layers and a 60 μm thick sheet composed of 30 layers. From the thickness and measured areal sheet density, the

volumetric density was calculated to be very light, ~0.0015 g/cm3. In Fig. 5.1(a), we show a photograph of a portion of an aperture array fabricated in the 30-layer, 60 μm thick freestanding CNT sheet drawn on top of a steel washer. For the CNT hole array (HA) fabrication, we used an excimer laser to mill holes in the CNT sheets. The array consisted of 0.65 mm diameter circular holes fabricated on a square lattice with a periodicity of 1.2 mm.

We used a THz-TDS setup [shown in Fig. 5.1(b)] for measuring the optical transmission spectra, $t(\omega)$ of the unperforated and perforated MWCNT films, where the THz frequency $\nu = \omega/2\pi$. Photoconductive devices were utilized for both emission and coherent detection of the THz field. Two off-axis paraboloidal mirrors were used to collect and collimate the linearly polarized THz beam from the emitter and focus the beam to the detector. The samples were attached to a solid metal plate with a 2 cm × 2 cm opening that is significantly larger than the THz beam size, and placed in the path of the collimated THz beam. The detected transient photocurrent, $PC(\tau)$, was recorded as a function of the translation stage path that determined the time delay, τ, between the 'pump' beam that hits the emitter and the 'probe' beam that arrives at the detector. $PC(\tau)$ was subsequently Fourier transformed and normalized to a reference transmission, yielding both the electric field transmission magnitude and phase, $t(\omega)$ in the range ~0.1 THz - 0.5 THz. The resulting Fourier transformed data may be described by the relation:

$$t(\omega) = |t(\omega)| \exp[i\varphi(\omega)] = \frac{E_{transmitted}(\omega)}{E_{incident}(\omega)}. \qquad (5.1)$$

In this expression $E_{incident}$ and $E_{transmitted}$ are the incident and transmitted THz fields, respectively, and $|t(\omega)|$ and $\varphi(\omega)$ are the magnitude and phase of the amplitude transmission coefficients, respectively. The THz-TDS technique is unique in that it

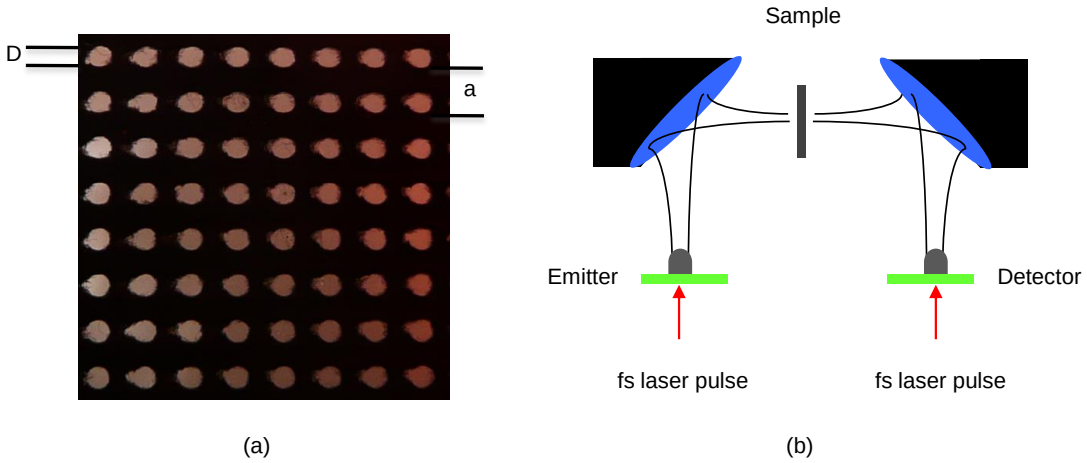

Figure 5.1. Experimental details of the temporal transmission measurement of the MWCNT films. (a) Photograph of the perforated carbon nanotube sheet with 30 CNT layers. The circular apertures have a diameter, D, of 0.65 mm and a periodic spacing, a, of 1.2 mm arranged in a square lattice. (b) Schematic drawing of the THz-TDS experimental geometry.

allows for a direct measurement of the transient THz electric field transmitted through the structures, yielding both amplitude and phase information. From such spectra both real and imaginary components of the refractive index, $n_{complex}(\omega)$ can be directly obtained without the need for Kramers-Kronig transformations, where somewhat arbitrary assumptions about asymptotic behavior are typically made.

5.3 Results and Discussion

In order to study SPP propagation on perforated MWCNT sheets, we first need to fully characterize the complex dielectric properties of the unperforated MWCNT sheets. In Fig. 5.2(a) we show the measured THz time-domain waveforms transmitted through a 25 μm MWCNT sheet, where the nanotubes are aligned parallel or perpendicular to the incident THz polarization (hereafter, these will be referred to as 'parallel' and 'perpendicular'). For reference purposes, we also show the time-domain waveform

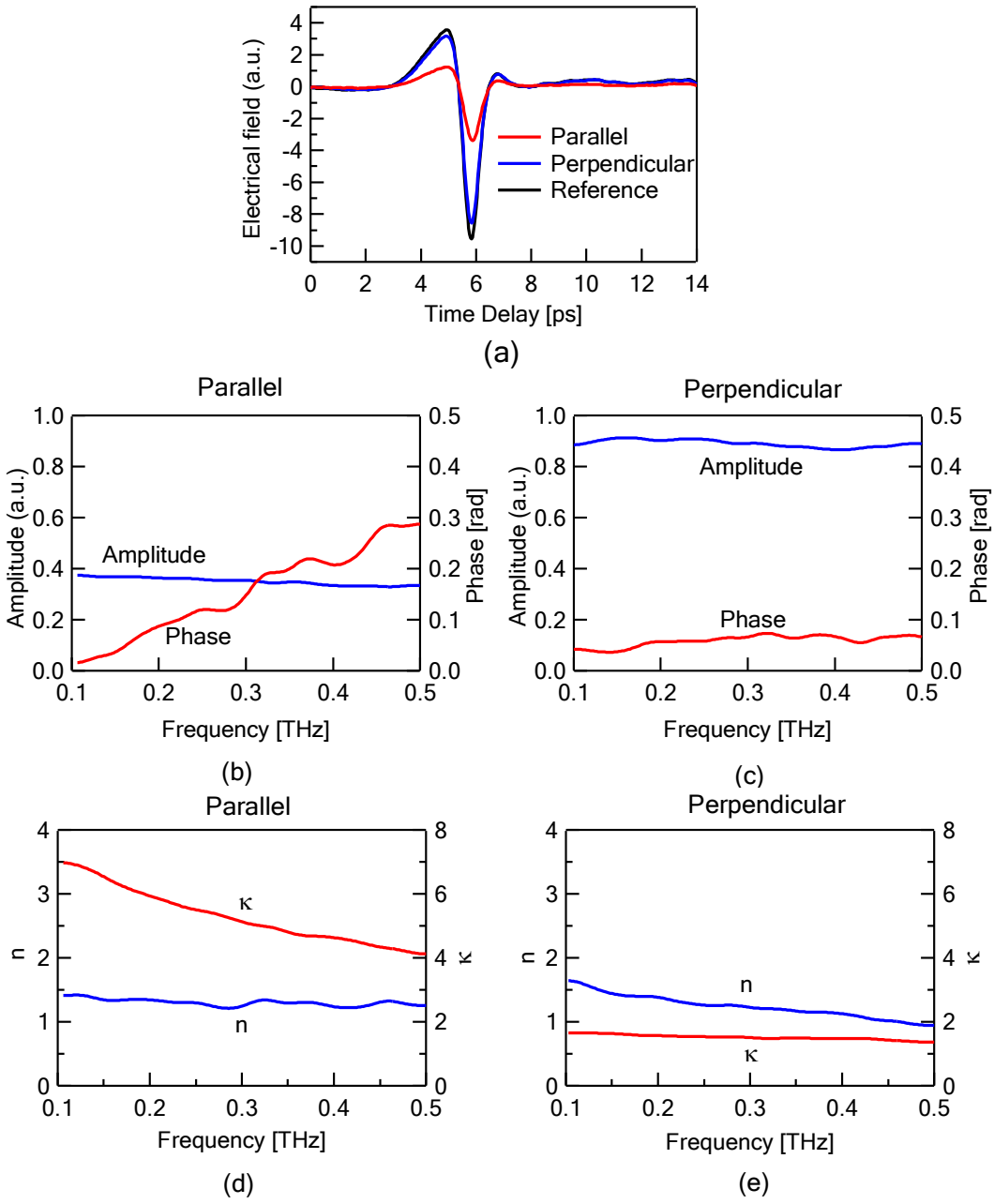

Figure 5.2. Transmission and dielectric properties of a 25 μm thick unperforated MWCNT sheet. (a) THz time-domain waveforms of the transmission through the MWCNT sheet for parallel and perpendicular orientations. The transmission spectra (b,c) and complex refractive index components, n and κ (d,e) in the parallel (b,d) and perpendicular (c,e) orientations, respectively, as obtained from Fig. 5.2(a). Note the scale difference between n and κ.

associated with the incident THz beam. It is apparent that the transmission properties are strongly dependent on the orientation of the nanotubes. This polarization dependence can be more clearly seen when the transient photocurrent in Fig. 5.2(a) is Fourier transformed to yield the normalized amplitude and phase spectra in the frequency domain [see Eq. (5.1)], as shown in Figs. 5.2(b) and 5.2(c), respectively. Using these two orientations, we observe an extinction ratio ($T_{\perp}/T_{//}$) of ~2. Similar THz polarization behavior in CNT sheets has been observed previously by several groups [4–9].

From the amplitude and phase information of the transmission, we can readily calculate the frequency-dependent complex index of refraction, n and κ, as shown in Figs. 5.2(d) and 5.2(e). While the real component, n, of the refraction index for the two nanotube orientations is similar, there is a large difference in the imaginary index of refraction, κ, which is related to the absorption coefficient. The frequency dependent absorption coefficient is given by the relation $\alpha(\nu) = 2\pi\nu\kappa/c$, where the electric field decay is given by $\exp[-\alpha(\nu)d]$, ν is the THz frequency and c is the speed of light in a vacuum. Based on the data in Figs. 5.2(d) and 5.2(e), the absorption coefficient is smaller at lower photon energy, which is in agreement with previous studies [4–6]. In order for a medium to support SPPs, the sign of the real component of the dielectric constant, $\varepsilon_r = n^2 - \kappa^2$, must be negative. Based on the data in Figs. 5.2(d) and 5.2(e), ε_r is negative for both orientations over the entire THz spectral range studied here, demonstrating that SPPs can be supported in principle.

It is well known [13,14] that gratings having periodic or aperiodic order may be used to compensate for the momentum mismatch between the incident light and SPP dispersion. In the case of subwavelength hole arrays, this results in SPP-induced

enhancement of the transmission at several resonant frequencies. With this in mind, we fabricated periodic hole arrays with periodicity of 1.2 mm and circular hole diameter of 0.65 mm in the nanotube sheets via laser ablation. In Fig. 5.3(a), we show the measured THz waveforms transmitted through a CNT hole array using a CNT sheet with a thickness of 25 μm and with the nanotubes aligned parallel to the incident THz polarization. The transmission spectrum shows that only ~50% of the THz field is transmitted.

In Fig. 5.3(b), we show the corresponding amplitude and phase spectra. Though weak, there is a clear resonance in the transmission spectra at ~0.25 THz. In order to explain the location of this resonance, we note that the antiresonance (AR) frequencies (as opposed to the resonance frequencies) can be found directly from the spatial Fourier transform of the real space aperture geometry [14]. In the case of a periodic array, the AR frequencies are given analytically by [13]:

$$\nu_{AR} = \frac{c}{an_{SPP}}\sqrt{i^2 + j^2}\,, \tag{5.2}$$

where

$$n_{SPP} = \left[\frac{\varepsilon_m \varepsilon_d}{\varepsilon_m + \varepsilon_d}\right]^{\frac{1}{2}}. \tag{5.3}$$

In these equations, n_{SPP} is the effective refractive index for the propagating SPP, ε_m and ε_d are the complex dielectric constants of the array medium and the adjacent dielectric media, respectively, a is the aperture periodicity, and i and j are integers that index the resonance order. Using the data in Fig. 5.2(d), we find that $n_{SPP} \cong n_{air} \approx 1.015$. From Eq. (5.2), we calculate the lowest order AR frequency, corresponding to $i = \pm 1$ and $j = 0$, to occur at a frequency $\nu_{AR} \approx 0.25$ THz. The associated transmission resonance

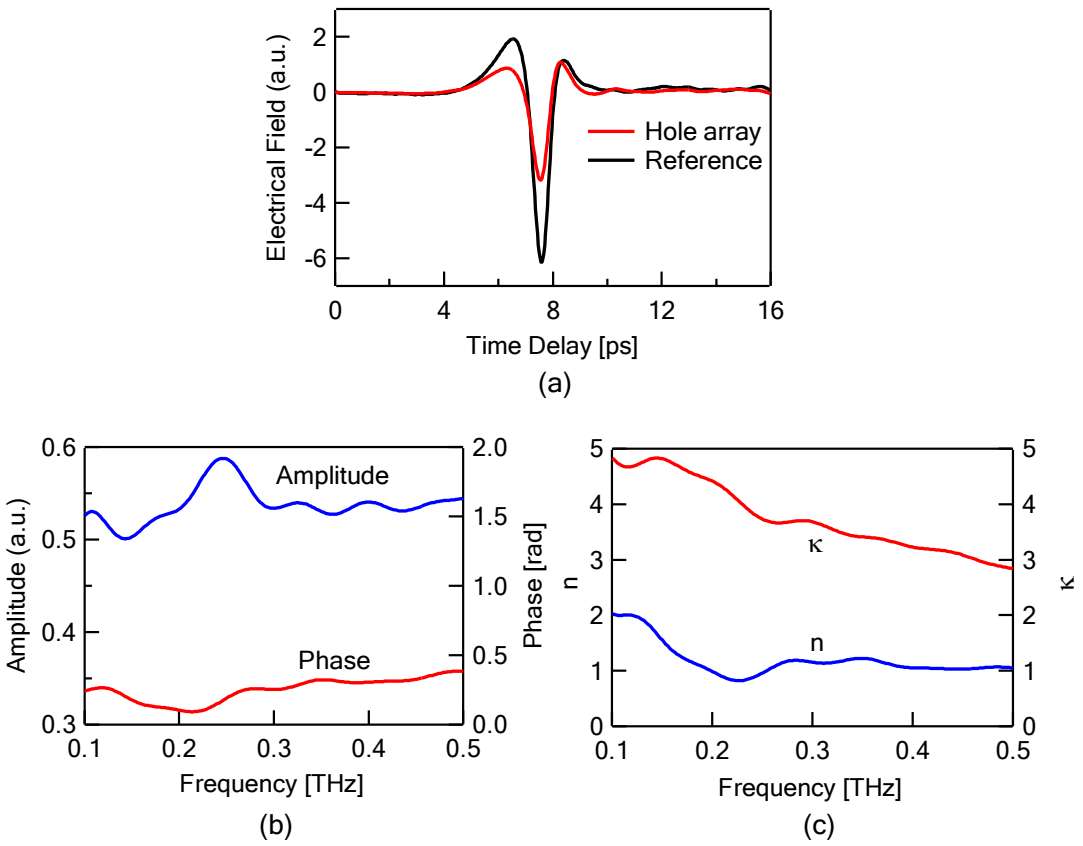

Figure 5.3. Transmission and dielectric properties of a 25 μm thick MWCNT hole array with 0.65 mm diameter holes and 1.2 mm periodicity in a parallel orientation. (a) THz time-domain waveforms measured after transmission through the MWCNT hole array in the parallel orientation, along with the reference. (b) Amplitude and phase spectra obtained from Fig. 5.3(a). (c) Calculated complex refractive index spectra, n and κ obtained from Fig. 5.3(b).

peak appears at a frequency that is just slightly smaller than this value. Although a clear AR is not apparent in Fig. 5.3(b), the computed value is in good agreement with our observations.

The transmission resonance further demonstrates that SPP excitations do exist and propagate on the one-dimensional nanotube structure. In contrast to the resonantly enhanced light transmission in a stainless steel structure, the transmission peak here is much weaker because of the greater THz absorption [15,16]. Furthermore, the transmission peak is quite broad and does not clearly show an antiresonance dip at the frequency higher than the resonance peak frequency. This indicates, more generally, that carbon nanotubes are lossy at THz frequencies, in agreement with the conclusions of Katsounaros et al. [6]. The effective imaginary component, κ of the refractive index for the structure in Fig. 5.3(c) clearly shows that the absorption at the resonance peak frequency is smaller than at other frequencies, corresponding to a larger transmission. Nevertheless, the observed resonance transmission of around 8% is encouraging, when taking into account the very low density of the MWCNT sheet ($0.0015 mg/cm^3$). We also examined the electric field transmission properties of the MWCNT HA with perpendicular orientation (not shown). We found that the resonantly enhanced light transmission through the CNT sheet does not occur in this case. The probable reasons are: (i) very low conductivity along this direction over this frequency range [see Figs. 5.2(c) and 5.2(e)]; and (ii) SPPs do not exist for directions orthogonal to the nanotube axis, because it is a nearly ideal quasi-one-dimensional system.

Up to this point, we have only examined the 25 μm thick MWCNT sheet. In Fig. 5.4(a) we show the strong THz transmission anisotropy for a 60 μm MWCNT sheet. In

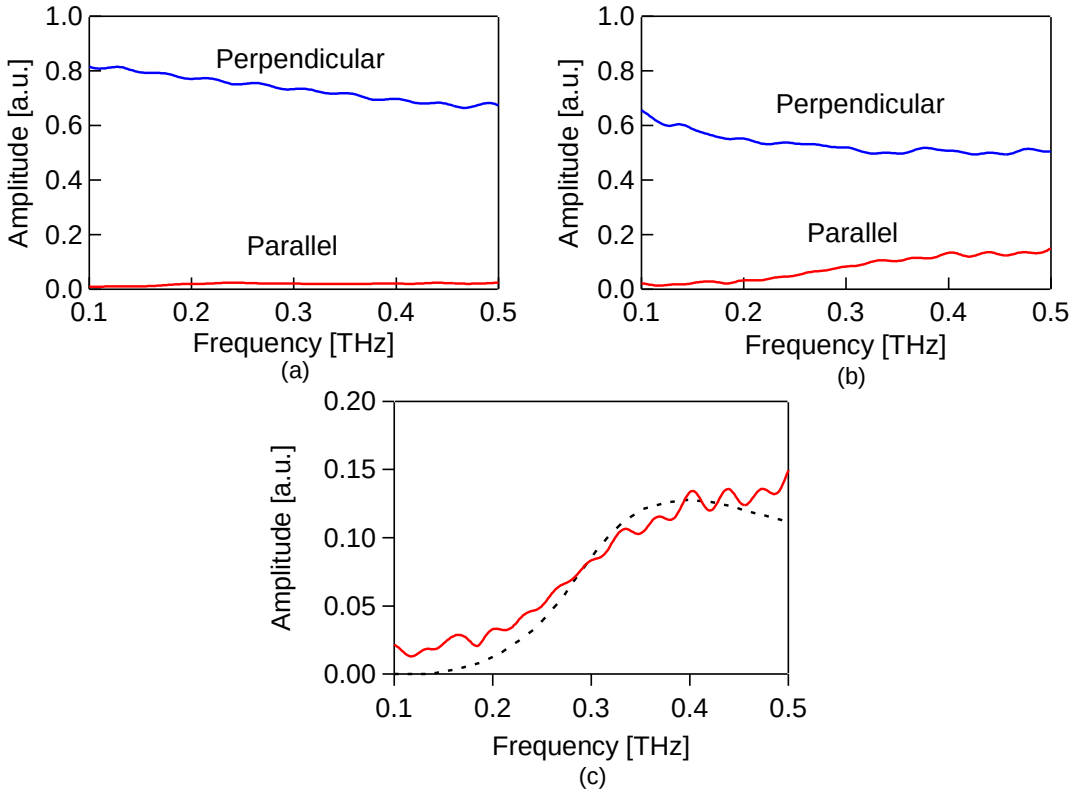

Figure 5.4. THz transmission properties of 60 μm thick MWCNT sheets. (a) Transmission spectra of an unperforated MWCNT sheet. (b) Transmission spectra of the film perforated with a periodic hole array with 0.65 mm diameter apertures and 1.2 mm periodicity on a square lattice, for both parallel (red) and perpendicular (blue) orientations. (c) The transmission spectrum for the hole array [parallel orientation from Fig. 5.4(b)] [red line] and the calculated normalized transmission for a single aperture (dashed black line) plotted in an extended scale.

this case, the extinction ratio ($T_{\perp}/T_{//}$) is nearly 40, which is more than an order of magnitude larger than the value obtained with the 25μm MWCNT sheet, and in good agreement with the literature [7,8]. Based on the high absorption for the parallel orientation [see Fig. 5.4(a)] we fabricated an array of subwavelength apertures with parameters identical to those for the 25 μm thick film. However, in this case we did not observe any resonantly enhanced transmission in either orientation, as can be seen from the transmission spectra shown in Fig. 5.4(b). This indicates that although the THz absorption from the film is high because of the high conductivity, the energy launched from the apertures in the form of SPP waves is probably reabsorbed in the thick MWCNT material. This places a practical limit on the thickness of MWCNT sheets for plasmonics applications. Nevertheless it is clearly seen that the transmission spectrum of the perforated film in the parallel geometry increases for $\nu > \sim 0.2$ THz, indicating that the individual holes still act as transmission enhancers [14], even though there is no SPP interference between the holes, which is necessary to yield transmission resonances [15]. In order to clarify this point, in Fig. 5.4(c) we plot the transmission spectra for the parallel orientation in Fig. 5.4(b) along with the calculated (normalized) transmission expected for a single aperture [14,17]. The good agreement between the data and model calculation confirms that the apertures act as individual transmission enhancers, but do not communicate with other apertures via launched SPPs, because of the large attenuation that hampers SPP propagation on the film surfaces.

5.4 Conclusion

We fabricated sub 100 μm-thick freestanding and highly oriented MWCNT sheets using the catalytic chemical vapor deposition method. Using THz-TDS we measured the

complex index of refraction spectra of the sheets for two orthogonal nanotube orientations. We found that the thick CNT sheet shows highly anisotropic THz polarization behavior with extinction ratio values of ~40. We investigated the existence and propagation of SPP excitations at THz frequencies by studying the resonantly enhanced transmission spectra through periodic aperture arrays fabricated on the MWCNT sheets. We found that CNTs support SPP propagation along the tubes. However, no SPP-related enhanced transmission was detected in the perpendicular direction. Furthermore we found that the resonantly enhanced transmission is absent in aperture arrays fabricated on a thick MWCNT sheet, although the individual apertures still act as transmission enhancers. These somewhat contradictory results can be explained by the strong reabsorption of the SPP excitations on the CNT sheet that prevents SPP propagation along the surfaces.

5.5 References

1. M. A. McCarthy, B. Liu, E. P. Donoghue, I. Kravchenko, D. Y. Kim, F. So, and A. G. Rinzler, "Low-voltage, low-power, organic light-emitting transistors for active matrix displays," Science **332**(6029), 570–573 (2011).

2. Z. Wu, Z. Chen, X. Du, J. M. Logan, J. Sippel, M. Nikolou, K. Kamaras, J. R. Reynolds, D. B. Tanner, A. F. Hebard, and A. G. Rinzler, "Transparent, conductive carbon nanotube films," Science **305**(5688), 1273–1276 (2004).

3. M. Zhang, S. Fang, A. A. Zakhidov, S. B. Lee, A. E. Aliev, C. D. Williams, K. R. Atkinson, and R. H. Baughman, "Strong, transparent, multifunctional, carbon nanotube sheets," Science **309**(5738), 1215–1219 (2005).

4. T.-I. Jeon, K.-J. Kim, C. Kang, I. H. Maeng, J.-H. Son, K. H. An, J. Y. Lee, and Y. H. Lee, "Optical and electrical properties of preferentially anisotropic single-walled carbon-nanotube films in terahertz region," J. Appl. Phys. **95**(10), 5736–5740 (2004).

5. T.-I. Jeon, K.-J. Kim, C. Kang, S.-J. Oh, J.-H. Son, K. H. An, D. J. Bae, and Y. H. Lee, "Terahertz conductivity of anisotropic single walled carbon nanotube films," Appl. Phys. Lett. **80**(18), 3403–3405 (2002).

6. M. Liang, Z. Wu, L. Chen, L. Song, P. Ajayan, and H. Xin, "Terahertz characterization of single-walled carbon nanotube and graphene on-substrate thin films," IEEE Trans. Microw. Theory Tech. **59**(10), 2719–2725 (2011).

7. A. Katsounaros, M. Mann, M. Naftaly, K. Z. Rajab, Y. Hao, and W. I. Milne, "Terahertz time-domain spectroscopy characterization of vertically aligned carbon nanotube films," Carbon **50**(3), 939–942 (2012).

8. J. Kyoung, E. Y. Jang, M. D. Lima, H.-R. Park, R. O. Robles, X. Lepró, Y. H. Kim, R. H. Baughman, and D.-S. Kim, "A reel-wound carbon nanotube polarizer for terahertz frequencies," Nano Lett. **11**(10), 4227–4231 (2011).

9. L. Ren, C. L. Pint, L. G. Booshehri, W. D. Rice, X. Wang, D. J. Hilton, K. Takeya, I. Kawayama, M. Tonouchi, R. H. Hauge, and J. Kono, "Carbon nanotube terahertz polarizer," Nano Lett. **9**(7), 2610–2613 (2009).

10. W. A. deHeer, W. S. Bacsa, A. Châtelain, T. Gerfin, R. Humphrey-Baker, L. Forro, and D. Ugarte, "Aligned carbon nanotube films: production and optical and electronic properties," Science **268**(5212), 845–847 (1995).

11. M. F. Islam, D. E. Milkie, C. L. Kane, A. G. Yodh, and J. M. Kikkawa, "Direct measurement of the polarized optical absorption cross section of single-wall carbon nanotubes," Phys. Rev. Lett. **93**(3), 037404 (2004).

12. H. H. Gommans, J. W. Alldredge, H. Tashiro, J. Park, J. Magnuson, and A. G. Rinzler, "Fibers of aligned singlewalled carbon nanotubes: Polarized Raman spectroscopy," J. Appl. Phys. **88**(5), 2509–2514 (2000).

13. T. W. Ebbesen, H. J. Lezec, H. F. Ghaemi, T. Thio, and P. A. Wolff, "Extraordinary optical transmission through sub-wavelength hole arrays," Nature **391**(6668), 667–669 (1998).

14. T. Matsui, A. Agrawal, A. Nahata, and Z. V. Vardeny, "Transmission resonances through aperiodic arrays of subwavelength apertures," Nature **446**(7135), 517–521 (2007).

15. A. Agrawal, Z. V. Vardeny, and A. Nahata, "Engineering the dielectric function of plasmonic lattices," Opt. Express **16**(13), 9601–9613 (2008).

16. T. Matsui, Z. V. Vardeny, A. Agrawal, A. Nahata, and R. Menon, "Resonantly-enhanced transmission through a periodic array of subwavelength apertures in heavily-doped conducting polymer films," Appl. Phys. Lett. **88**(7), 071101 (2006).

17. F. J. García de Abajo, J. J. Sáenz, I. Campillo, and J. S. Dolado, "Site and lattice resonances in metallic hole arrays," Opt. Express **14**(1), 7–18 (2006).

CHAPTER 6

COHERENT DETECTION OF MULTIBAND TERAHERTZ RADIATION USING A SURFACE PLASMON-POLARITON BASED PHOTOCONDUCTIVE ANTENNA

6.1 Introduction

Terahertz time-domain spectroscopy (THz-TDS) is an extremely important and increasingly popular technique for spectroscopic and imaging applications in the far-infrared [1]. A commonly used approach for generating broadband terahertz (THz) radiation involves the use of photoconductive devices, such as Hertzian dipole antennas fabricated on semiconductor substrates in which the carrier recombination times are extremely short [2,3]. While much of the focus in this area has been on broadband applications, numerous applications require only narrowband THz capabilities. As examples, the ability to differentiate between materials based on their spectral fingerprints [4,5] or to observe its conformational state in a time-resolved manner [6] typically only requires that spectral information be measured at a few select frequencies. Thus, a coherent multiband THz detector that exhibits greater sensitivity at those select frequencies may be more useful than a broadband detector for such applications. Such a photoconductive device could also be used as a multiband THz emitter.

While there are a number of viable approaches to developing such detectors [7–9], some of the developments within the field of plasmonics seem particularly relevant.

Corrugated metal surfaces are well known to allow for narrowband propagation of surface plasmon-polaritons (SPPs) [10]. Of particular relevance here, when a concentric circular grating surrounds a subwavelength aperture, the radiation transmitted through the aperture can be strongly enhanced at specific frequencies related to the periodicity of the corrugation [11]. While the initial demonstrations using these so-called bullseye structures were performed at optical frequencies [11,12], related observations have been made at THz [13] and microwave [14] frequencies. These bullseye structures have been used to improve the sensitivity of photodiodes [15,16], the throughput of surface emitting lasers [17], and the coupling to microwave [17] and THz waveguides [18].

We experimentally demonstrated enhanced narrowband detection using a dipole antenna surrounded by an electrically isolated portion of a bullseye structure relative to a dipole antenna without the surrounding structure. We found that the frequency associated with sensitivity enhancement was directly related to the corrugation periodicity, while its magnitude was related to the number of annular grooves. We performed numerical finite-difference time-domain (FDTD) simulations of these geometries and found good agreement with the observations. Based on these results, we designed a dipole antenna with a modified bullseye structure that allowed for enhanced multiband detection sensitivity.

6.2 Experimental Details

Figure 6.1 shows schematic diagrams of the dipole antennas. We fabricated two dipole antennas on a silicon-on-sapphire (SOS) substrate that had a 0.6 μm thick silicon layer using standard lithographic techniques and aluminum metallization. In both devices, the dipole antenna is 100 μm wide with tip spacing of 5 μm and metal line width of 20

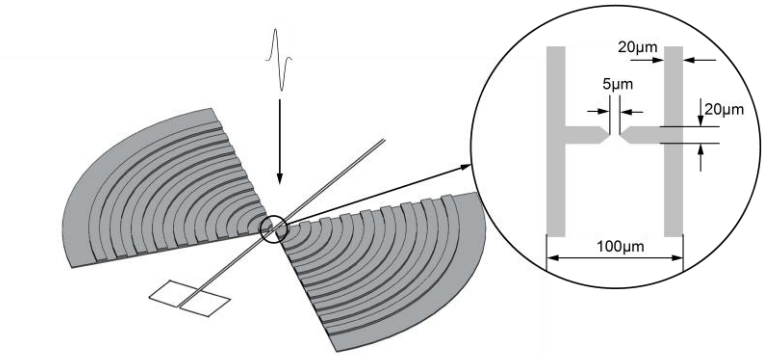

(a)

(b)

Figure 6.1. Schematic diagram of the fabricated bullseye dipole antenna. (a) Schematic diagram of the bullseye dipole antenna with an expanded view of the dipole section of the antenna. The dipole antenna is 100 μm wide with tip spacing of 5 μm and metal line width of 20 μm. (b) Schematic cross-section of the right quadrant of the bullseye, showing the 500 μm circular opening on the left side. The bullseye pattern consists of eight concentric annular grooves that span 90 °, centered on the dipole. The rectangular cross-section annular grooves are 100 μm deep and 500 μm wide, with a periodic spacing of 1 mm.

μm. One antenna was used as the reference and we fabricated a portion of a bullseye structure on the other. As shown in Fig. 6.1(a), two quadrants of a bullseye pattern are placed to the left and right of the dipole with the center of the circular pattern lying at the center of the dipole. Since the antenna is overwhelmingly sensitive to incident THz radiation polarized parallel to the dipole, the contributions of the top and bottom quadrants of the bullseye are negligible.

To form the bullseye structures, a 100 μm thick layer of SU-8 2025 negative photoresist was spun-cast to define the annular protrusions. We then deposited a 400 nm-thick layer of aluminum to fully define the bullseye pattern. It should be noted that with metal thicknesses that are greater than ~ 2 skin depths (δ ~ 150 nm for Al at THz frequencies [19]), the dielectric properties of the underlying medium do not affect the SPP propagation properties [20]. As shown in Fig. 6.1(b), the bullseye pattern consists of a single 500 μm diameter circular opening surrounded by eight concentric annular grooves that span 90°. The rectangular cross-section annular grooves are 100 μm deep and 500 μm wide, with a periodic spacing of 1 mm. The central opening in the bullseye pattern ensures that the structure is not electrically connected to the dipole. This is important, since the frequency response of the antenna is associated with the effective dipole length. The gap in metallization between the bullseye and the dipole does not significantly reduce the coupling of SPPs to the dipole. Both dipoles were used as detectors, while only a standard dipole antenna was used as the broadband THz emitter.

6.3 Experimental Results, Simulation and Discussion

Figure 6.2 summarizes the experimental and numerical results. In Fig. 6.2(a), we show the temporal waveforms measured with a collimated broadband incident THz beam

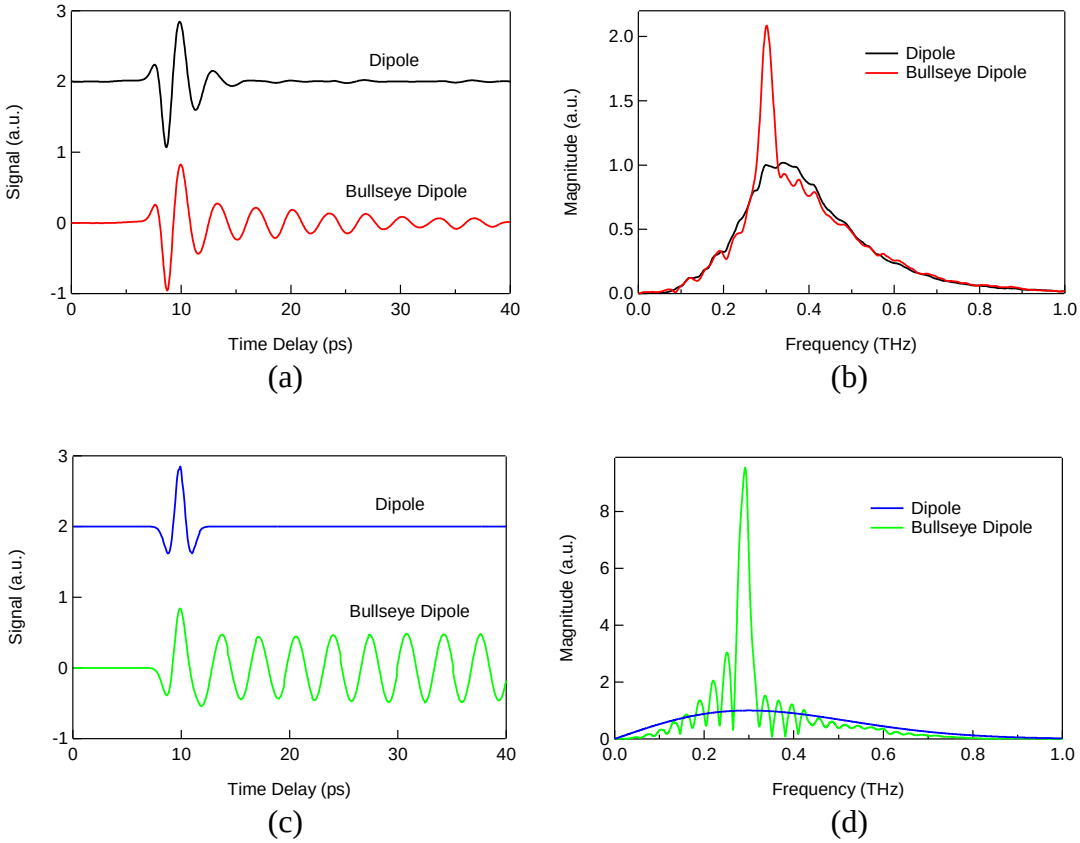

Figure 6.2. Time-domain waveforms and corresponding amplitude spectra of the two dipole antennas. (a) Experimentally measured time-domain waveforms for the reference dipole (red trace) and the bullseye dipole (black trace). The temporal waveforms have been offset from the origin for clarity. (b) The corresponding amplitude spectra of Fig. 6.2(a). (c) Numerically simulated time-domain waveforms for the same structures as in Fig. 6.2(a). The temporal waveforms have also been offset from the origin for clarity. (d) The corresponding amplitude spectra of Fig. 6.2(c).

for the reference dipole and bullseye dipole antennas. No substrate lenses or other focusing lenses were used in either case. It is obvious from the data that the waveform associated with the reference antenna is made up of only a single bipolar pulse, while the waveform associated with the bullseye dipole antenna is comprised of the initial bipolar waveform and eight time-delayed oscillations (one per groove). This is consistent with our earlier demonstration that the transmitted time-domain waveform through a bullseye structure consists of a nonresonant contribution related to direct propagation through the subwavelength opening and a resonant contribution related to the phase-coherent interaction of the THz pulse with the structured metal surface [13]. Therefore, by performing the measurement in this manner (i.e., without any lenses), the role of the bullseye pattern in the detected signal is clearly evident. As seen in corresponding amplitude spectra, shown in Fig. 6.2(b), the reference antenna exhibits broadband response, while the bullseye antenna exhibits a factor of approximately two enhancement relative to that of the reference dipole at the resonant frequency of 0.3 THz. It is worth noting that the bullseye structure does not appear to reduce the frequency response of the dipole, as seen in Fig. 6.2(b). Also, because the bullseye corrugation "collects" THz radiation over a larger area than the dipole, no substrate lens [2,21] is needed.

In order to confirm these results, we performed FDTD simulations. In Fig. 6.2(c), we show the simulated time-domain waveforms for the two antennas. The waveform associated with the bullseye dipole contains an initial single cycle waveform followed by eight phase-coherent oscillations (one per groove); however, these oscillations are larger in magnitude than in Fig. 6.2(a). This arises from two assumptions made in the simulations: (1) we assume that the metal can be modeled as a perfect electrical

conductor, so there is no absorption loss, and (2) the incident beam is modeled as a plane wave, while in the experiment the beam has a Gaussian spatial distribution. The corresponding amplitude spectra are shown in Fig. 6.2(d). Based on these assumptions, the spectrum for the bullseye dipole antenna exhibits stronger enhancement at the resonant frequency of 0.3 THz.

With these initial results in mind, we now describe modifications to the bullseye dipole that will enable enhanced sensitivity at multiple frequencies. The simplest implementation involves creating a superposition of two separate periodicities. As shown in Fig. 6.3(a), we can combine two separate geometries: structure 1 with the 200 μm wide grooves periodically spaced by 600 μm, and structure 2 with 600 μm wide grooves periodically spaced by 1.2 mm. In both cases, the grooves are 50 μm deep. To implement this idea, we numerically simulated the signal of the structure shown in Fig. 6.3(b). Within these simulations, we also altered the dimension of the central opening, as shown in Fig. 6.3(c), since we found that this parameter could alter the relative magnitudes of the resulting resonances.

In Fig. 6.3(d), we show the amplitude spectra associated with each of the bullseye dipole antennas normalized by the response of a simple dipole antenna. It is clear that there are three resonance peaks at 0.25 THz, 0.5 THz and 0.75 THz (and a weak peak at 1 THz), where structure 2 (1.2 mm periodicity) contributes to all of the peaks (fundamental, second harmonic, third harmonic and a weak fourth harmonic), while structure 1 (400 μm periodicity) only contributes to the 0.75 THz resonance (fundamental). Since the harmonics associated with structure 2 become increasingly weak for higher orders, we introduce structure 1 to increase the magnitude of the resonance at 0.75 THz. In the

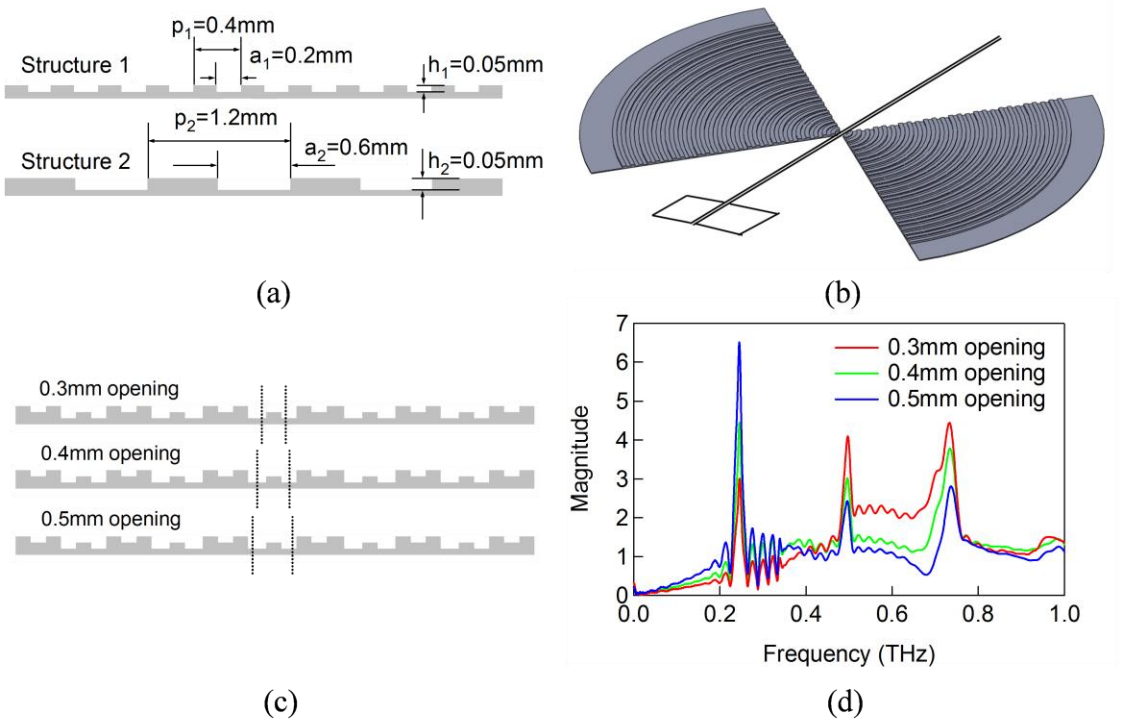

Figure 6.3. Numerical simulations of structures designed for multiple frequency enhancements. (a) Decomposition of the structure into two sections: structure 1 with groove width, a_1 (200 μm), periodicity, p_1 (600 μm), and structure 2 with groove width, a_2 (600 μm), periodicity, p_2 (1.2 mm), both with groove depth, (h_1 and h_2, 50 μm). (b) Schematic diagram of the resulting bullseye dipole antenna. (c) The composite structures with different opening diameters of 300 μm, 400 μm and 500 μm. The dotted lines denote where metal would be removed. (d) Normalized amplitude spectra showing sensitivity enhancement relative to a simple dipole antenna.

implementation above, the periodicities of the superposed structures are related to one another. However, the general procedure is equally valid for the superposition of arbitrary periodicities. In addition to the placement of the individual grooves, there are several other parameters that can be tuned to vary the properties of each resonance. These include variation of the size of the central opening and the cross-sectional parameters of each individual groove [22].

As a final point, we discuss the spectral properties of the individual resonances. As we have previously discussed, each annular groove couples essentially the entire bandwidth of the incident THz wave to surface waves, a portion of which then propagates towards the dipole. Therefore, the resulting detected THz time-domain waveform, E_{total}, may be written as

$$E_{total}(t) = E_b(t) + \sum_{n=1} c_n E_b(t - T_o - T_n). \tag{6.1}$$

Here, $E_b(t)$ is the component of the incident THz pulse measured by the dipole detector, n corresponds to the groove number, c_n is a scale factor that accounts for the SPP coupling and any associated propagation loss, T_n accounts for the time delay associated with the propagation distance, and To accounts for a time delay between the initial waveform, $E_b(t)$, and the delayed oscillations. It is apparent from Eq. (6.1) that the superposition of square structures with different periodicities will introduce multiple sinc (sin x / x) function-like resonances, and the time-delayed oscillations will modify the resonance frequencies and their corresponding amplitudes and lineshapes.

6.4 Conclusion

In conclusion, we have experimentally demonstrated a coherent SPP based narrowband THz detector by fabricating a portion of a circular grating about a conventional dipole antenna. We observe a factor of two enhancement at the design frequency, although numerical simulations suggest that much larger enhancement factors can be obtained. The grating allows for collection of incident radiation outside of the dipole region via coupling to SPPs, obviating the need for a substrate lens. By superimposing multiple periodicities and varying the details of the grooves, it is possible to obtain enhanced detection sensitivity at multiple frequencies. In the current work, these antennas have only been used for coherent detection. They should work equally well as narrowband or multiband THz emitters.

6.5 References

1. M. Tonouchi, "Cutting-edge terahertz technology," Nature Photon. **1**, 97–105 (2007).
2. D. H. Auston, K. P. Cheung, and P. R. Smith, "Picosecond photoconducting Hertzian dipoles," Appl. Phys. Lett. **45**(3), 284–286 (1984).
3. Ch. Fattinger and D. Grischkowsky, "Terahertz beams," Appl. Phys. Lett. **54**(6), 490–492 (1989).
4. M. Walther, B. Fischer, M. Schall, H. Helm, and P. Uhd Jepsen, "Far-infrared vibrational spectra of all-trans, 9-cis and 13-cisretinal measured by THz time-domain spectroscopy," Chem. Phys. Lett. **332**, 389–395 (2000).
5. K. Kawase, Y. Ogawa, and Y. Watanabe, "Non-destructive terahertz imaging of illicit drugs using spectral fingerprints," Opt. Express **11**(20), 2549–2554 (2003).
6. M. C. Beard, G. M. Turner and C. A. Schmuttenmaer, *Liquid Dynamics: Experiment, Simulation, and Theory. J.T. Fourkas* (Ed. American Chemical Society: Washington D.C., 2002).
7. A. S. Weling, B. B. Hu, N. M. Froberg, and D. H. Auston, "Generation of tunable narrow-band THz radiation from large aperture photoconducting antennas," Appl. Phys. Lett. **64**(2), 137–139 (1994).

8. F. Miyamaru, Y. Saito, M. W. Takeda, L. Liu, B. Hou, W. Wen, and P. Sheng, "Emission of terahertz radiations from fractal antennas," Appl. Phys. Lett. **95**(22), 221111 (2009).

9. P. Maraghechi and A. Y. Elezzabi, "Enhanced THz radiation emission from plasmonic complementary Sierpinski fractal emitters," Opt. Express **18**(26), 27336–27345 (2010).

10. H. Raether, *Surface Plasmons on Smooth and Rough Surfaces and on Gratings* (Springer-Verlag: Berlin, 1988).

11. T. Thio, K. M. Pellerin, R. A. Linke, H. J. Lezec, and T. W. Ebbesen, "Enhanced light transmission through a single subwavelength aperture," Opt. Lett. **26**(24), 1972–1974 (2001).

12. H. J. Lezec, A. Degiron, E. Devaux, R. A. Linke, L. Martin-Moreno, F. J. Garcia-Vidal, and T. W. Ebbesen, "Beaming light from a subwavelength aperture," Science **297**, 820–822 (2002).

13. H. Cao, A. Agrawal, and A. Nahata, "Controlling the transmission resonance lineshape of a single subwavelength aperture," Opt. Express **13**(3), 763–769 (2005).

14. M. J. Lockyear, A. P. Hibbins, J. R. Sambles, and C. R. Lawrence, "Enhanced microwave transmission through a single subwavelength aperture surrounded by concentric grooves," J. Opt. A: Pure Appl. Opt. **7**, 152–158 (2005).

15. T. Ishi, J. Fujikata, K. Makita, T. Baba, and K. Ohashi, "Si nano-photodiode with a surface plasmon antenna," Jpn J. Appl. Phys. **44**(12), 364–366 (2005).

16. R. D. Bhat, N. C. Panoiu, S. R. Brueck, and R. M. Osgood, "Enhancing the signal-to-noise ratio of an infrared photodetector with a circular metal grating," Opt. Express **16**(7), 4588–4596 (2008).

17. M. Beruete, I. Campillo, J. S. Dolado, J. E. Rodriguez-Secco, E. Perea, F. Falcone, and M. Sorolla, "Very low-profile "bull's eye" feeder antenna," IEEE Ant. Wireless Propag. Lett. **4**, 365–368 (2005).

18. A. Agrawal and A. Nahata, "Coupling terahertz radiation onto a metal wire using a subwavelength coaxial aperture," Opt. Express **15**(14), 9022–9028 (2007).

19. M. A. Ordal, L. L. Long, R. J. Bell, S. E. Bell, R. R. Bell, R. W. Alexander, Jr., and C. A. Ward, "Optical properties of the metals Al, Co, Cu, Au, Fe, Pb, Ni, Pd, Pt, Ag, Ti, and W in the infrared and far infrared," Appl. Opt. **22**(7), 1099–1120 (1983).

20. X. Shou, A. Agrawal, and A. Nahata, "Role of metal film thickness on the enhanced transmission properties of a periodic array of subwavelength apertures," Opt. Express **13**(24), 9834–9840 (2005).

21. D. B. Rutledge and M. S. Muha, “Imaging antenna arrays,” IEEE Trans. Antennas Propag. **AP-30**(4), 535–540 (1982).

22. A. Agrawal, H. Cao, and A. Nahata, “Excitation and scattering of surface plasmon-polaritons on structured metal films and their application to pulse shaping and enhanced transmission,” New J. Phys. **7**, 249 (2005).

CHAPTER 7

OPTIMIZATION OF GEOMETRICAL PARAMETERS OF INDIVIDUAL CONICALLY TAPERED APERTURES

7.1 Introduction

The ability to concentrate optical radiation is a topic of long-standing interest that has utility in a broad range of applications [1-4]. In the case of freely propagating radiation, the diffraction limit constrains the minimum spot size to a dimension that is on the order of the free space wavelength. One approach to circumvent this limitation is through the use of Plasmonics. Surface plasmon-polaritons (SPPs) are surface electromagnetic waves that propagate along the interface between a metal and a dielectric and are characterized by dispersion properties that differ dramatically from those of free space radiation. Using SPPs, there have been numerous theoretical and experimental studies that rely on metallic structures to focus or concentrate electromagnetic radiation to dimensions much smaller than the associated free space wavelength [5]. Common implementations of this have relied on tapered wires [6-8], holes [9-12] and plates [13-15].

As an example, we recently demonstrated that individual conically tapered apertures (TAs) could be used to efficiently concentrate broadband terahertz (THz) radiation [11]. In that work, we kept the input aperture diameter and the taper angle fixed and found that as the diameter of the exit plane aperture was decreased, we obtained an increase in the magnitude of the transmitted THz electric field, which varied inversely

with the output aperture diameter. For the smallest aperture that we fabricated, we obtained a ~50 fold increase in the transmitted THz intensity.

However, several important issues regarding the tapered structures still need to be resolved. For example, although it is clear enough that the decrease of the output dimensions could result in a larger field enhancement [11,13,15], only a few papers studied other parameters that characterize the geometrical dimensions of the tapered structures [16,17], and the optimal parameters seem strongly dependent on the geometrical shapes. Therefore, the aim of this work is to further examine the properties of a conical TA and optimize its geometrical parameters. In the earlier publication [11], we kept the input aperture diameter and the taper angle fixed, but varied the thickness of the structure and the output diameter. However, in most practical applications, the working distance of the equipment cannot be changed, demanding that the thickness of the structure be fixed. Moreover, since the output diameter determines the resolution, it is also an important parameter that we don't want to alter randomly.

We describe the optimization of the geometrical properties of individual apertures, while keeping the output aperture diameter and the structure thickness fixed. As expected, we found that there was an optimal taper angle that maximizes the optical throughput. We also confirmed that effective cutoff frequency associated with a closed hole is determined by both the diameter of the output aperture and the taper angle.

7.2 Experimental Details

We fabricated a series of individual TAs in 3-mm-thick stainless steel disks using wire electrical discharge machining (wire EDM). Each TA was fabricated on a separate metal disk and consisted of a circular output aperture with a fixed diameter, D_2, of 400 μm and a conical taper full angle, α, of 15 °, 30 °, 45 °, 60 °, 75 °, or 90 °. Therefore, the

diameter, D_1, of the circular input aperture varied as a function of α and took on values of 1.19 mm, 2.00 mm, 2.88 mm, 3.86 mm, 5.00 mm, and 6.40 mm, respectively. For reference purposes, we also fabricated a 400 μm diameter aperture in a 75 μm thick free-standing stainless steel foil and a TA with a taper angle α of 0°, corresponding to a straight 400-μm-diameter aperture, in the 3-mm-thick metal disk. These are shown schematically in Fig. 7.1 (a).

To characterize these samples, we used a THz time-domain spectroscopy (THz-TDS) setup as shown schematically in Fig. 7.1(b). Details of the experimental setup and the advantageous properties of this approach have been discussed previously [18], and thus are presented only briefly here. Photoconductive devices were used for both emission and coherent detection. An off-axis paraboloidal mirror was used to collect and collimate the THz radiation as it propagated from the emitter to the sample, resulting in a 1/e THz beam diameter of ~ 8 mm, which was larger than the cross-sectional area of the input apertures. In all cases, the THz beam was incident on the input surface of the samples at normal incidence. Coherent THz pulses radiated from the output face of the apertures were collected by a hyper-hemispherical-silicon-lens-coupled photoconductive dipole detector that was located ~ 10 mm from the output plane of the apertures. The detected transient photocurrent was then Fourier transformed and normalized to the reference transmission; using this procedure, we obtained an electric field transmission spectrum that spanned the frequency range of ~ 0.05 - 0.8 THz.

We also performed numerical finite-difference time-domain (FDTD) simulations of the SPP propagation properties, where the metal was modeled as a perfect electrical conductor (PEC), since metal conductivities are typically high at THz frequencies, while the surrounding dielectric medium was assumed to be air. We used a spatial grid size of

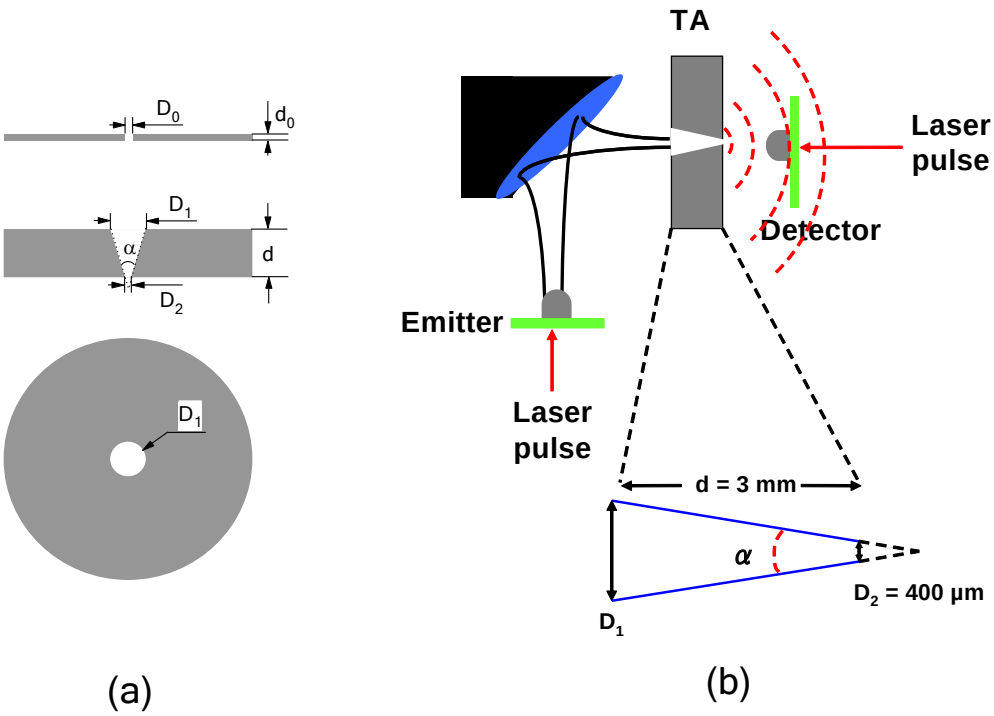

Figure 7.1. Schematic diagram of the experimental details. (a) Schematic diagram of the individual conically tapered apertures with different taper angles. Top: cross-section of the reference aperture with an aperture diameter, D_o = 400 μm and metal thickness, d_o = 75 μm. Middle and bottom: cross-section and top view, respectively, of a single tapered aperture with a variable taper full angle, α, and a fixed output aperture diameter, D_2 = 400 μm. The taper angle determines the input aperture diameter, D_1. The thickness of the metal disk is d = 3 mm. (b) Schematic diagram of the THz time-domain spectroscopy system. A collimated THz beam was normally incident on the sample. The radiated electromagnetic wave was detected using a photoconductive device for coherent broadband THz detection.

50 μm, which was sufficient to ensure convergence of the numerical calculations, and perfectly matched layer absorbing boundary conditions for all boundaries. For the input electric field, we used a plane wave that was modeled temporally as the derivative of a Gaussian pulse. The resulting bipolar THz pulse had the same bandwidth and approximately the same pulse shape as was available in the experimental work. All of the simulated results were measured at specific spatial points in the vicinity of the output plane of the structure.

7.3 Experimental Results, Simulation and Discussion

Figure 7.2 summarizes the basic concentration properties of individual TAs as a function of the taper full angle, α. In Fig. 7.2(a), we show the spectral field amplitude concentration factor, $f_E(\nu)$, for each tapered aperture, which is defined as

$$f_E(\nu) = \frac{t_\alpha(\nu)}{t_{ref}(\nu)}, \tag{7.1}$$

where $t_\alpha(\nu)$ is the measured transmission amplitude spectrum through an individual 3-mm-thick TA of angle α, and $t_{ref}(\nu)$ is the measured transmission amplitude spectrum through an individual cylindrical reference aperture of 400-μm diameter fabricated in a 75-μm-thick stainless steel foil. There are several points to note regarding these data. For a TA with $\alpha = 0°$ (i.e., a straight 400-μm-diameter aperture in a 3-mm-thick metal disk), the transmission enhancement below ~ 0.5 THz appears to be strongly suppressed and there is essentially no transmission through the TA below ~ 0.4 THz. This behavior is reasonable for a circular aperture, where we would expect increasingly suppressed transmission below the cutoff frequency, ν_c [$= 1.841c/(\pi D_2)$] [19], where c is the speed of light in a vacuum). In the case of the 400-μm-diameter reference aperture, the film thickness (75 μm) is sufficiently small that frequencies below ν_c (~ 0.44 THz) exhibit

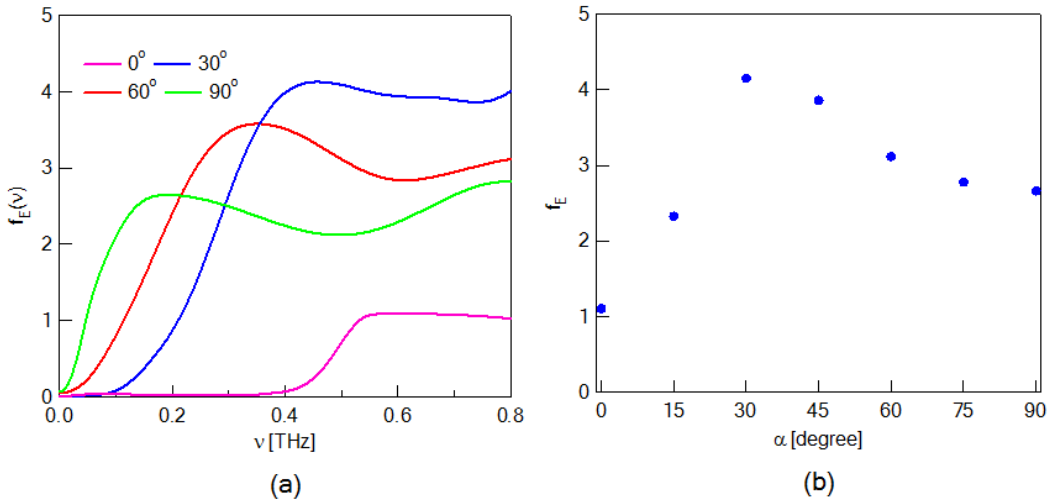

Figure 7.2. The experimentally measured spectral transmission properties of an individual tapered aperture structure as a function of the taper full angle, α. (a) Spectra of the field amplitude concentration factor, $f_E(\nu)$, with respect to α, as noted. (b) Electric field concentration maximum, f_E, as a function of the taper angle, α.

only modest transmission suppression. However, in the TA structure with 0 ° taper angle (i.e., the straight aperture in the 3-mm-thick disk), the waveguide cutoff phenomenon is more evident because of the metal thickness. Moreover, above ~ 0.6 THz, the transmission enhancement is ~ 1. Above the cutoff frequency the propagation constant is largely real, since the high conductivity of metals allows for low loss propagation through the aperture. Therefore there is relatively little difference between the 75-μm-thick reference aperture and the 3 mm thick straight aperture at frequencies well above cutoff.

As the taper angle increases, the spectral concentration factor changes both in shape and amplitude. The shape of the concentration spectrum is related to the cutoff characteristics of the TA and is discussed in greater detail below. For the concentration amplitude, we can define a concentration factor maximum, f_E [shown in Fig. 7.2(b)], that corresponds to the maximum value of $f_E(\nu)$; we plot $f_E(\nu)$ as a function of α in Fig. 7.2(a). It is clearly seen that $f_E(\nu)$ is maximized for a taper angle $\alpha = 30°$. Below 30 ° the small taper angle corresponds to an input aperture diameter that is only slightly larger than the output aperture diameter, thus limiting the maximum concentration factor. Above 30 °, although the input aperture diameter becomes larger, there is increased reflectivity from the aperture sidewalls, which reduces the measured concentration factor.

In order to confirm the experimental observations, we used analytical calculations as well as 3D FDTD simulations. In both cases we based our calculation on geometrical parameters that were used in the experiments. As we noted above, the effective cutoff frequencies for the TAs appear to red shift with increasing taper angle, in apparent contradiction with the more usual view that the cutoff frequency is associated only with the diameter of the output aperture. This red shift can be readily explained by the fact that the TA diameter varies along the length of the aperture. Consequently, for a straight

400 μm diameter aperture (i.e., $\alpha = 0°$), the cutoff frequency is $\nu_c = 1.841c/(\pi D) = 0.44$ THz along the entire length of the aperture. However, for $\alpha = 90°$, the TA input aperture diameter is 6.4 mm, corresponding to $\nu_c = 0.03$ THz, while the output aperture diameter is 400 μm, corresponding to $\nu_c = 0.44$ THz. Therefore, the incident radiation experiences a continuously varying diameter as it propagates through the aperture.

In order to model this geometry analytically, we analyzed the propagation properties of the lowest order mode of a cylindrical waveguide [20] as the waveguide diameter varied continuously, using the geometrical parameters of the TA. The resulting spectral concentration factors are shown in Fig. 7.3 (see Suppl. Inf. for the mathematical details of this analysis). In order to compare the calculated and experimental spectral properties, each curve in Fig. 7.3 was scaled to match the maximum amplitude shown in Fig. 7.2(a). From the good agreement between the analytical calculations and experimental data, we conclude that the red shift in the effective cutoff frequency can be attributed to the aperture variation of the TA with α.

While the analytical model describes well the shift in the spectral transmission properties with α, it does not properly predict the concentration factor amplitude as a function of α. In order to model this property, we used 3D FDTD simulations for each of the TAs studied. As an example of the comparison between experiment and simulation, we show in Fig. 7.4(a) the spectral concentration factor for a TA with $\alpha = 30°$. The model calculation agrees very well with the experiment, both in terms of spectral shape and amplitude. In Fig. 7.4(b) we show f_E as a function of α obtained using these simulations, compared with the experimental values from Fig. 7.2(b). The agreement is good for all taper angles and demonstrates again that $\alpha = 30°$ is indeed the optimal TA angle. While the data presented correspond to a specific metal thickness, we have performed additional

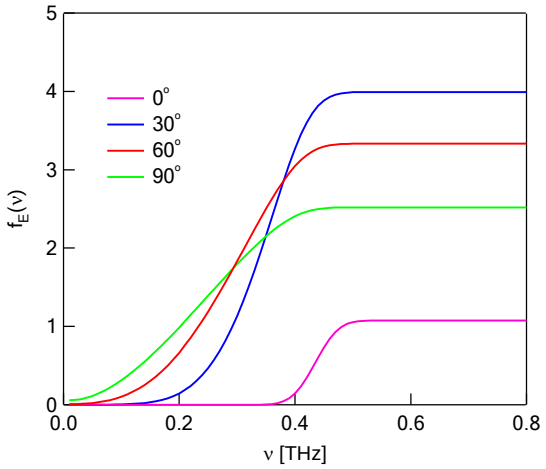

Figure 7.3. Calculated $f_E(\nu)$ spectra of single tapered apertures for various full taper angles, α, as given. The calculation is based on cylindrical waveguide theory as described in the text. The result for each α was scaled to match the experimental concentration amplitude shown in Fig. 7.2(a).

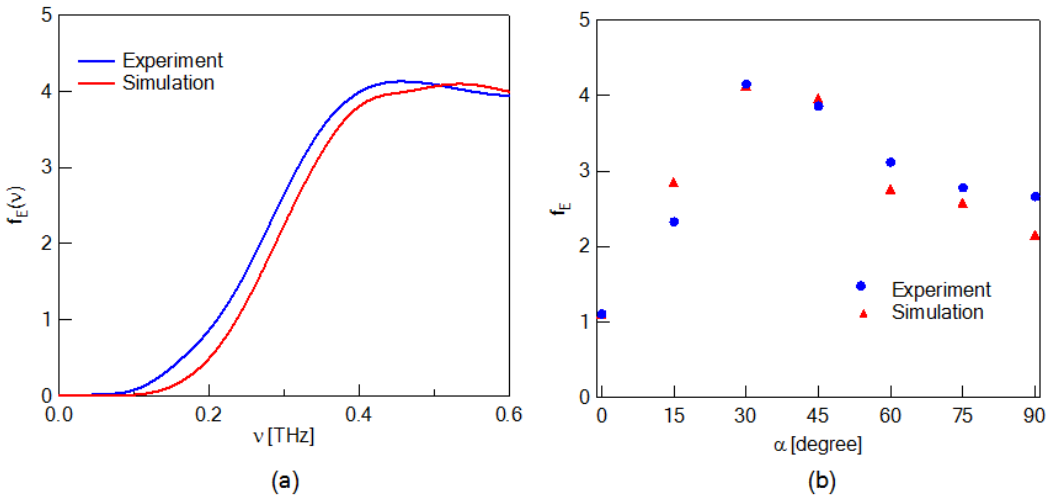

Figure 7.4. Numerical simulations of the field properties for individual tapered aperture structures. (a) The enhancement spectrum $f_E(\nu)$ for a TA with $\alpha = 30°$ from simulation (red trace) and experiment (blue trace). (b) Field concentration factor maximum, f_E, of the TAs with various α obtained from simulation (red dots); the experimental f_E results from Fig. 7.2(b) are shown for comparison (blue dots).

numerical simulations with different taper lengths between 3 and 10 mm and found that 30° appears to be the optimal taper angle in each case. Moreover, we found that in the simulations the increase of the length did not enhance the concentration much. From Ref. [6], when the free space radiation is coupled into the TA, the wave evolves and the energy transfers among different modes during propagation. Then the oscillation becomes weaker and tends to be more and more stable. Thus the length of the TA may also influence its concentration effect by whether the propagation evolves into the stable state, and further investigation regarding this point would also be interesting. Finally, according to our simulation, the optimal taper full angle also appears $\sim 30^\circ$ for the tapered parallel plate waveguide with two planar plates tilted to form a smaller output slit of 100-μm plate spacing.

7.4 Supplementary Information

We studied the relation between the geometrical parameters of the tapered apertures (TAs) and the resulting cutoff frequencies, and found that the effective cutoff frequencies were not only dependent on the output aperture diameter but also on the taper angle. In order to analytically examine the transmission properties of the TAs, we modeled this geometry as a waveguide with continuously varying diameter, using the actual parameters in the experiment. During the calculation, we merely analyzed the propagation properties of the lowest order mode of a cylindrical waveguide, since the lowest order mode is a constraint that determines the cutoff-frequency, as explained below.

We started the process by solving the propagating modes in cylindrical waveguide from Maxwell's equations using cylindrical coordinates. The detailed solution can be easily found in most electromagnetic books [20] and is beyond the scope of this

dissertation. According to the cutoff frequency associated with each TE or TM mode in the cylindrical waveguide, the lowest order mode, TE_{11}, defines the value of the cutoff frequency. Thus for simplicity, we watch tense on the TE_{11} mode hereafter.

The electrical field components of the TE_{mn} mode in the cylindrical coordinates can be written as [20]

$$E_\rho = -A_{mn}\frac{m}{\varepsilon\rho}J_m(\beta_\rho\rho)[-C_m\sin(m\varphi)+D_m\cos(m\varphi)]e^{-ik_z z}, \tag{7.2}$$

$$E_\varphi = A_{mn}\frac{\beta_\rho}{\varepsilon}J_m'(\beta_\rho\rho)[C_m\cos(m\varphi)+D_m\sin(m\varphi)]e^{-ik_z z}, \tag{7.3}$$

$$E_z = 0, \tag{7.4}$$

where $J_m(x)$ is the Bessel function, A_{mn}, C_m, and D_m are the coefficients. Besides, $\beta_\rho = \frac{\chi_{mn}}{r}$, in which χ_{mn} is the nth zero of $J_m(x)$ and r is the radius of the waveguide.

In addition, k_z is the wave vector along z axis, $k_\rho^2 + k_z^2 = k^2$ and $k = 2\pi\nu/c_0$, and thus

$$k_z = \begin{cases} \sqrt{k^2 - k_\rho^2}, k \ge k_\rho \\ -i\sqrt{k_\rho^2 - k^2}, k < k_\rho \end{cases} = -i\sqrt{k_\rho^2 - k^2}\,. \tag{7.5}$$

In our experiment, the incident beam is linearly polarized, E_x and E_y should be equivalent. Assume the polarization is along x, the corresponding electrical field can be expressed as [21]:

$$E_x = E_\rho\cos(\varphi) - E_\varphi\sin(\varphi), \tag{7.6}$$

When m = 1, n = 1 (for TE_{11} mode which determines the cutoff frequency),

$$\begin{aligned} E_x = &-A_{11}\frac{1}{\varepsilon}\frac{J_1(\beta_\rho\rho)}{\rho}[-C_1\sin(\varphi)\cos(\varphi)+D_1\cos(\varphi)\cos(\varphi)]e^{-i\beta_z z} \\ &-A_{11}\frac{\beta_\rho}{\varepsilon}J_1'(\beta_\rho\rho)[C_1\cos(\varphi)\sin(\varphi)+D_1\sin(\varphi)\sin(\varphi)]e^{-i\beta_z z} \end{aligned}. \tag{7.7}$$

For far field measurement, the detected signal includes the electrical field integrated over the whole plane [22], so

$$E(z)=\int_0^{2\pi}\int_0^{r} E_x d\rho d\varphi = -A_{11}D_1\frac{\pi}{\varepsilon}e^{-i\beta_z z}\left\{\beta_\rho r J_0(\beta_\rho r)+\frac{\pi\beta_\rho r}{2}\left[J_1(\beta_\rho r)\mathrm{H}_0(\beta_\rho r)-J_0(\beta_\rho r)\mathrm{H}_1(\beta_\rho r)\right]\right\}. \quad (7.8)$$

Here, H is the struve function.

Since in Eq. (7.8) for the TE_{11} mode, $\beta_\rho r=\chi_{11}=1.8412$ is a constant, the electrical field could be evaluated based on the phase term $e^{-i\beta_z z}$.

$$t=A'\int_0^d e^{-i\beta_z z}dz=A'\int_0^d e^{-\sqrt{\left(\frac{\chi_{11}}{r_0+z\tan\left(\frac{\theta}{2}\right)}\right)^2-\left(\frac{2\pi\nu}{c_0}\right)^2}z}dz\,. \quad (7.9)$$

To obtain the transmission coefficient of the TA structure, the aperture with continuously varying radius could be divided into thin cylindrical apertures with constant radius and infinitesimal thickness, and analyzed discretely, supposing that the wave could evolve into the stable state within that small distance.

7.5 Conclusion

In summary, we have experimentally studied individual aperture parameters, specifically the determination of the optimal taper angle. Interestingly, the effective cutoff frequency red shifted with increasing taper angle, which was a consequence of the rate of change in a continuously varying aperture diameter. Further numerical characterization of the tapered aperture structure also confirmed our findings. This investigation provided us with further understanding of the tapered apertures and "best parameters" for the next step of the research.

7.6 References

1. E. Betzig, M. Isaacson, and A. Lewis, "Collection mode near-field scanning optical microscopy," Appl. Phys. Lett. **51**, 2088-2090 (1987).

2. S. Hunsche, M. Koch, I. Brener, and M. C. Nuss, "THz near-field imaging," Opt. Comm. **150**, 22-26 (1998).

3. J. Villatoro, D. Monzón-Hernández, and D. Talavera, "High resolution refractive index sensing with cladded multimode tapered optical fibre," Electron. Lett. **40**, 106-107 (2004).

4. K. S. Paul, E. Barclay, and O. Painter, "Nonlinear response of silicon photonic crystal microresonators excited via an integrated waveguide and fiber taper," Opt. Express **13**, 801-820 (2005).

5. J. A. Schuller, E. S. Barnard, W. Cai, Y. C. Jun, J. S. White and M. l. Brongersma, "Plasmonics for extreme light concentration and manipulation," Nat. Mater. **9**, 193-204 (2012).

6. N. A. Janunts, K. S. Baghdasaryan, K. V Nerkararyan and B. Hecht, "Excitation and superfocusing of surface plasmon polaritons on a silver-coated optical fiber tip," Opt. Comm. **253**, 118-124 (2005).

7. M. I. Stockman, "Nanofocusing of optical energy in tapered plasmonic waveguides," Phys. Rev. Lett. **93**, 137404 (2004).

8. M. Awad, M. Nagel, and H. Kurz, "Tapered Sommerfeld wire terahertz near-field imaging," Appl. Phys. Lett. **94**, 051107 (2009).

9. A. J. Babadjanyan, N. L. Margaryan, and K. V. Nerkararyan, "Superfocusing of surface polaritons in the conical structure," J. Appl. Phys. **87**, 3785-3788 (2000).

10. A. Rusina, M. Durach, K. A. Nelson, and M. I. Stockman, "Nanoconcentration of terahertz radiation in plasmonic waveguides," Opt. Express **16**, 18576-18589 (2008).

11. T. D. Nguyen, Z. V. Vardeny, and A. Nahata, "Concentration of terahertz radiation through a conically tapered aperture," Opt. Express **18**, 25441-25448 (2010).

12. M. C. Schaafsma, H. Starmans, A. Berrier, and J. Gómez Rivas, "Enhanced terahertz extinction of single plasmonic antennas with conically tapered waveguides," New Journal of Physics **15**, 015006 (2013).

13. V. Astley, R. Mendis, and D. M. Mittleman, "Characterization of terahertz field confinement at the end of a tapered metal wire waveguide," Appl. Phys. Lett. **95**, 031104 (2009).

14. H. Choi, D. F. P. Pile, S. Nam, G. Bartal and X. Zhang, "Compressing surface plasmons for nano-scale optical focusing," Opt. Express **17**, 7519-7524 (2009).

15. K. Iwaszczuk, A. Andryieuski, A. Lavrinenko, X.-C. Zhang, and P. U. Jepsen, "Terahertz field enhancement to the MV/cm regime in a tapered parallel plate waveguide," Opt. Express **20**, 8344-8355 (2012).

16. S. Kim, E. Lee, Y. Ji, and T. Jeon, "Improvement of THz coupling using a tapered parallel-plate waveguide," Opt. Express **18**, 2779–2783 (2010).

17. D. Gramotnev, D. Pile, M. Vogel, and X. Zhang, "Local electric field enhancement

during nanofocusing of plasmons by a tapered gap," Phys. Rev. B **75**, 035431 (2007).

18. H. Cao, A. Agrawal, and A. Nahata, "Controlling the transmission resonance lineshape of a single subwavelength aperture," Opt. Express **13**, 763-769 (2005)

19. N. Marcuvitz, *Waveguide Handbook* (New York: McGraw-Hill, 1951).

20. C. A. Balanis, *Engineering Electromagnetics* (John Wiley & Sons, 1989).

21. G. B. Arfken, and H. J. Weber, *Mathematical Methods for Physicists* (Elsevier Academic Press, 2005).

22. I. S. Gradshteyn, and I. M. Ryzhik, *Table of Integrals, Series and Products* (Elsevier Academic Press, 2007).

CHAPTER 8

CONCENTRATION OF BROADBAND TERAHERTZ RADIATION USING A PERIODIC ARRAY OF CONICALLY TAPERED APERTURES

8.1 Introduction

Tapered structures have long been applied in a variety of fields to concentrate and focus electromagnetic radiation. While individual tapered structures are useful for applications such as raster scanned near-field imaging [1,2], the sequential acquisition of single pixel data greatly reduces the overall collection efficiency of the system, thereby increasing the total acquisition time. In such cases, the use of multiple identical structures may allow for parallel acquisition. Furthermore, if the radiation from arrays of tapered structures can be focused, it may allow for enhanced nonlinear optical conversion efficiency. In recent years, there have only been a few reports associated with 'plasmonic lattices' in which the individual elements are tapered [3,4]. In both cases, since thin metal films with small taper angles were used, the individual transmission resonances were enhanced and the narrowband nature of the enhancement remained unchanged.

We demonstrated that periodic arrays of conically tapered cylindrical apertures concentrate broadband THz radiation for frequencies above an effective cutoff frequency. We fabricated a hexagonal array containing 19 apertures with the optimal taper angle demonstrated earlier in [5] and showed that the transmitted radiation was also broadband. In contrast to prior work [3,4,6], the large metal thickness allowed for large differences

between the input and output aperture diameters, while maintaining taper angles that could be relatively small. As we showed, a consequence of this design is that the transmission of each aperture was effectively independent of all of the other apertures. Further concentration of the transmitted radiation could be obtained by tilting the tapered apertures (TAs) toward the array center, thereby decreasing the effective output cross-sectional area, or by cascading the TA structures.

8.2 Experimental Details

We fabricated an individual TA in a 3-mm-thick stainless steel disk as a reference, using wire electrical discharge machining (wire EDM). It consisted of a circular output aperture with a diameter, D_2, of 400 μm and a conical taper full angle, α, of 30°, which was identified as the optimal taper angle in our earlier studies [5]. Therefore, the diameter, D_1, of the circular input aperture is 2.0 mm, as shown schematically in the lower left portion of Fig. 8.1(a). We also fabricated a periodic array of 19 TAs that were placed in a hexagonal lattice, as shown in the lower right portion of Fig. 8.1(a). Each TA in this array was identical and the same as the reference TA, having a 400-μm-diameter (D_2) output aperture and a 30° full angle (α) taper, corresponding to a 2.0-mm-diameter (D_1) input aperture, with the aperture axis normal to the disk surface. The center-to-center spacing between the TAs was also 2.0 mm. Photographs of the array input and output faces are shown in Fig. 8.1(b). For reference purposes, we also fabricated a 400-μm-diameter aperture in a 75-μm-thick free-standing stainless steel foil. It is shown schematically in the top portion of Fig. 8.1 (a).

To characterize these samples, we used a THz time-domain spectroscopy (THz-TDS) setup as shown schematically in Fig. 8.1(c). Details of the experimental setup and the advantageous properties of this approach have been discussed previously [5,7], and

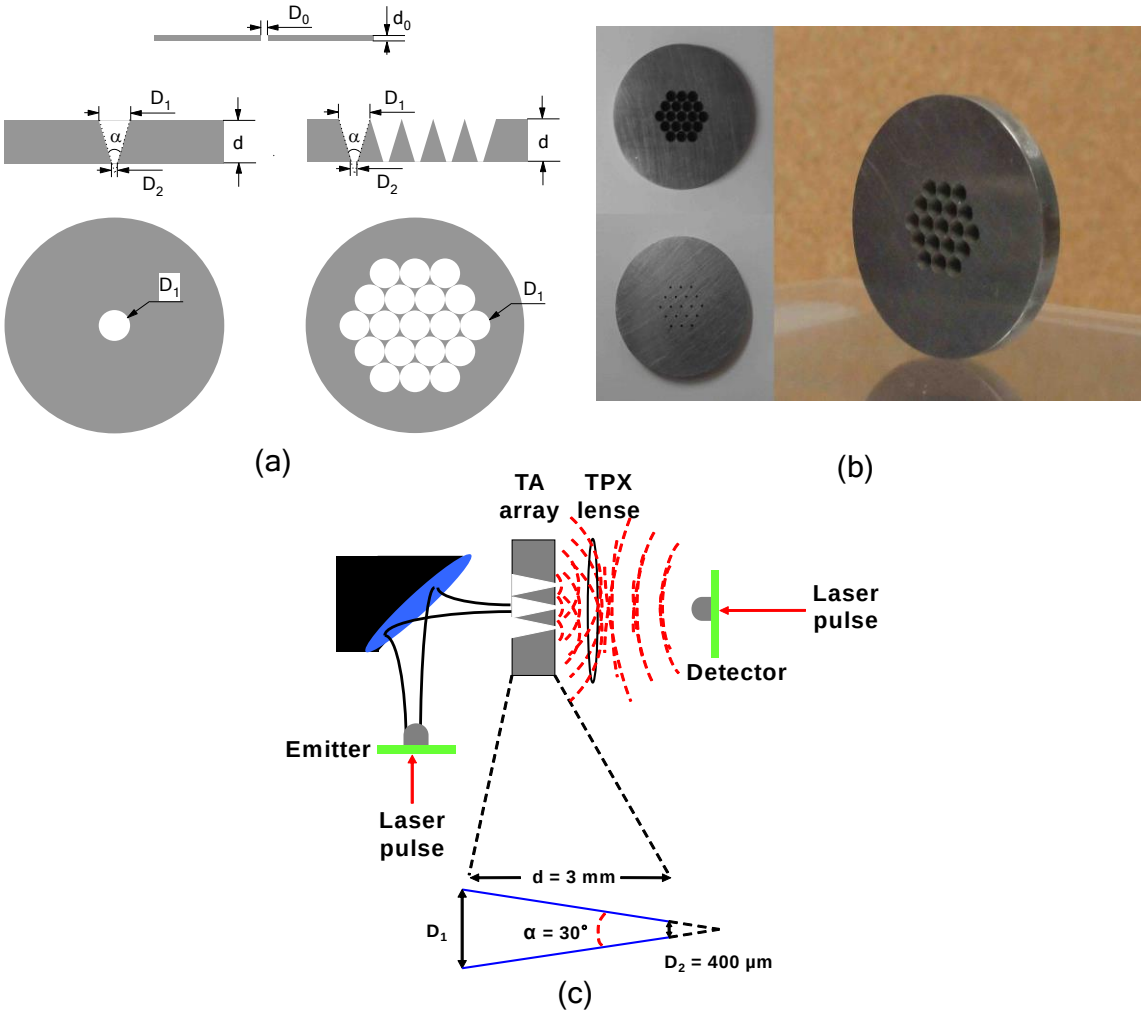

Figure 8.1. Details of the experimental design. (a) Schematic diagram of the different aperture structures studied. Top: cross-section of the reference aperture with an aperture diameter, D_o = 400 μm and metal thickness, d_o = 75 μm. Middle left and bottom left: cross-section and top view, respectively, of a single tapered aperture with a taper full angle, α = 30°, and an output aperture diameter, D_2 = 400 μm. The taper angle determines the input aperture diameter, D_1 = 2.0 mm. The thickness of the metal disk is d = 3 mm. Middle right and bottom right: cross-section and top view, respectively, of the hexagonal lattice of tapered aperture arrays with nineteen apertures, fabricated normal to the disk surface, with tapered apertures identical to the single tapered aperture and spaced from center to center by 2.0 mm. Once again, the thickness of the metal disk is d = 3 mm. (b) Photographs of the stainless steel tapered aperture array structure from Fig. 8.1(a) with 19 apertures, each with α = 30°. (c) Schematic diagram of the THz time-domain spectroscopy system. A collimated THz beam was normally incident on the sample. The radiated electromagnetic wave was detected using a photoconductive device for coherent broadband THz detection.

thus are presented only briefly here. Photoconductive devices were used for both emission and coherent detection. An off-axis paraboloidal mirror was used to collect and collimate the THz radiation as it propagated from the emitter to the sample. To accommodate the larger cross-sectional areas of the TA arrays, two changes were made in the setup. We used a larger paraboloidal mirror to form a 1/e THz beam diameter of ~ 12 mm, which was larger than the cross-sectional area of the input apertures. Since the cross-sectional area of the output surface of this structure is also significantly larger than the single TA, we now inserted a 50-mm-focal-length TPX lens between the sample and detector for all of the samples, close to the output surface of the samples to ensure the efficient collection of the radiation from all the apertures in the TA array. Coherent THz pulses radiated from the output face of the apertures were focused onto a hyper-hemispherical-silicon-lens-coupled photoconductive dipole detector that was located ~ 50 mm from the output plane of the apertures. The detected transient photocurrent was then Fourier transformed and normalized to the reference transmission; using this procedure, we obtained an electric field transmission spectrum that spanned the frequency range of ~ 0.05 - 0.8 THz.

We also performed numerical finite-difference time-domain (FDTD) simulations of the SPP propagation properties, where the metal was modeled as a perfect electrical conductor (PEC), since metal conductivities are typically high at THz frequencies, while the surrounding dielectric medium was assumed to be air. We used a spatial grid size of 50 μm, which was sufficient to ensure convergence of the numerical calculations, and perfectly matched layer absorbing boundary conditions for all boundaries. For the input electric field, we used a plane wave that was modeled temporally as the derivative of a Gaussian pulse. The resulting bipolar THz pulse had the same bandwidth and

approximately the same pulse shape as was available in the experimental work. All of the simulated results were measured at specific spatial points in the vicinity of the output plane of the structure or averaged across area of the output aperture(s).

8.3 Experimental Results, Simulation and Discussion

As demonstrated in last chapter and also Ref. [5], for an individual TA having $\alpha = 30°$ and an output aperture diameter of 400 μm in a 3-mm-thick metal slab, we find that the electric field concentration factor is ~ 4. Again the spectral field amplitude concentration factor, $f_E(\nu)$, is defined as

$$f_E(\nu) = \frac{t_\alpha(\nu)}{t_{ref}(\nu)}, \tag{8.1}$$

where $t_\alpha(\nu)$ is the measured transmission amplitude spectrum through a 3-mm-thick sample with a TA or TAs of angle α, and $t_{ref}(\nu)$ is the measured transmission amplitude spectrum through an individual cylindrical reference aperture of 400-μm diameter fabricated in a 75-μm-thick stainless steel foil. Since an input aperture of an individual TA is typically much smaller than the incident THz beam, the overall optical throughput is limited. In such cases, it may be advantageous to use multiple apertures simultaneously and thereby more fully utilize the incident THz beam. With this in mind, we fabricated a periodic array of TAs placed in a close-packed hexagonal geometry, where the aperture axes are all normal to the metallic disk surface [Fig. 8.1(b)]. In measuring the field amplitude concentration factor $f_E(\nu)$ for the TA array and single TA, both sets of data were normalized using the spectrum of the same single reference aperture.

In Fig. 8.2, we show the spectral concentration factor for a single TA and TA array containing 19 TAs in a hexagonal pattern. In both cases, the apertures had a taper angle of $\alpha = 30°$. Similar to the single TA that exhibits a relatively flat spectrum well

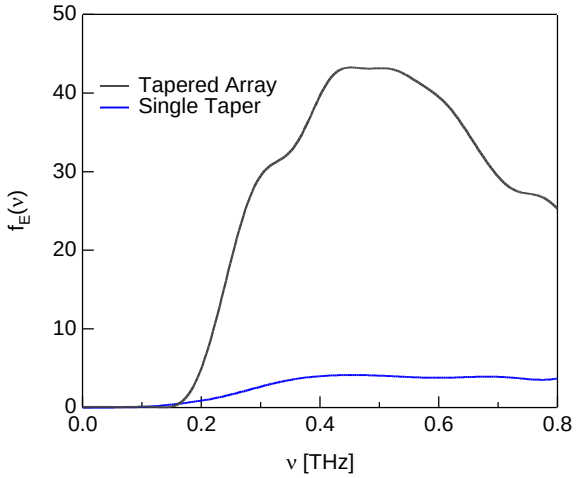

Figure 8.2. The spectral amplitude concentration factors, $f_E(\nu)$ measured for the tapered aperture array and a single TA having $\alpha = 30°$ full angle. Both spectra were normalized by the transmitted field of the same reference obtained from a single cylindrical aperture.

above a cutoff frequency, the spectrum associated with the TA array also appears to be rather broad. However there is a decrease in the enhancement factor at high frequencies. Furthermore the concentration enhancement for the TA array at ~ 0.5 THz is only ~ 10 times larger than that observed for a single TA, rather than the factor of 19 expected from the number of apertures in the array. Both of these observations can be readily explained by the fact that the incident THz beam has a frequency-dependent Gaussian spatial profile. We noted that the 1/e THz beam diameter used here was ~ 12 mm, but this only corresponds to the beam diameter at ~ 0.3 THz. For higher frequencies, the beam diameter is correspondingly smaller. Thus, the factor of 19 enhancement could only be achieved if the incident beam was uniform over the array area. The fact that the beam becomes increasingly smaller with increasing THz frequency may also explain why the enhancement is not flat above ~ 0.5 THz. We therefore conclude that, while a larger concentration enhancement can be achieved using a larger TA array, it is also necessary

that the incident beam be larger than the input cross-sectional area of the array at all relevant THz frequencies.

Given that the apertures in the array are placed in a periodic geometry, it is reasonable to determine whether or not any transmission resonances should be present based on the excitation of surface plasmon-polaritons (SPPs). These resonances arise from constructive interference between SPPs scattered from discontinuities (apertures, in this case) that are present on both the input and output faces of the structure. In a conventional hexagonal array of subwavelength apertures, we expect well-defined transmission resonances at wavelengths given by [6]

$$\lambda_{res} = \frac{P}{\left[\frac{4}{3}(i^2 + ij + j^2)\right]^{\frac{1}{2}}} n_{SPP}, \tag{8.2}$$

where P is the periodic spacing between apertures, i and j are integers, and n_{SPP} is the effective refractive index for a propagating SPP (for a metal-air interface, $n_{SPP} \sim 1$ at THz frequencies). Thus the lowest order resonance (i=$\pm$1, j=0) is expected to occur at $\lambda_{res} \approx \sqrt{3}P/2$, which for P = 2 mm corresponds to 0.17 THz. This frequency, however lies in the low transmission regime of the TA array and, therefore, has minimal impact on the resulting spectrum. The next two higher order resonances are expected to occur at $\nu = 0.3$ THz (i=$\pm$1, j=$\pm$1) and $\nu = 0.34$ THz (i=$\pm$2, j=0 or i=0, j=$\pm$2). However, these resonances are also suppressed and are not clearly present in the data. This suppression arises primarily from the fact that the output aperture diameter (400 μm) is significantly smaller than the periodic spacing (2 mm), resulting in weak resonances below the cutoff frequency, ν_c [$= 1.841c/(\pi D_2)$] = ~ 0.44 THz [8], where c is the speed of light in vacuum, associated with the output aperture [9].

Based on the available enhancement with a TA array, it is reasonable to consider

modifications to the geometry that would allow for tighter focusing. Specifically, for the TA array discussed above, the input cross-sectional area and the output cross-sectional area are approximately the same. Thus, there is minimal spatial focusing caused by such structures. We now consider the effect of tilting the axes of the outer TAs in the array towards the array center, thereby reducing the output span of the apertures, which allows for radiation concentration to a smaller area on the output plane. By maintaining the hexagonal geometry and tilting the axes of the outer TAs (inclination angle, θ with regard to the normal axis), we maintain a six-fold rotationally symmetric pattern on the output surface of the array. In this case, the input surface has a periodic spacing p_1 = 2 mm, while the output surface has a periodic spacing p_2, which is determined by the tilt angle θ. This is shown schematically in Fig. 8.3(a). Figure 8.3(b) displays a snapshot of the electric field pattern near the exit plane of a TA array structure with p_2 = 1.0 mm. It can be seen that the field strength of the six outer TAs is weaker than that of the central TA. Since these are time-domain simulations, it is also worth noting that the transit time through the tilted apertures is slightly longer than the apertures that are not tilted. Therefore, the field maxima are not present in the output plane at the same time for the central aperture and the outer apertures. Nevertheless, as we show below, tilting the apertures reduces the optical throughput.

Clearly, there is a need to consider the optimal tilt angle and what effect an aperture tilt has on the polarization properties of an individual TA. In Fig. 8.3(c), we show the concentration enhancement, f_E, for a tapered aperture with input diameter, D_1= 2 mm, and output diameter, D_2 = 400 μm, which is tilted by an angle θ along the x-axis for incident THz radiation that is polarized along the x- and y-axes. Here we present an angle range from 0 ° to 33.7 °. For an aperture with no tilt, the transmission properties are

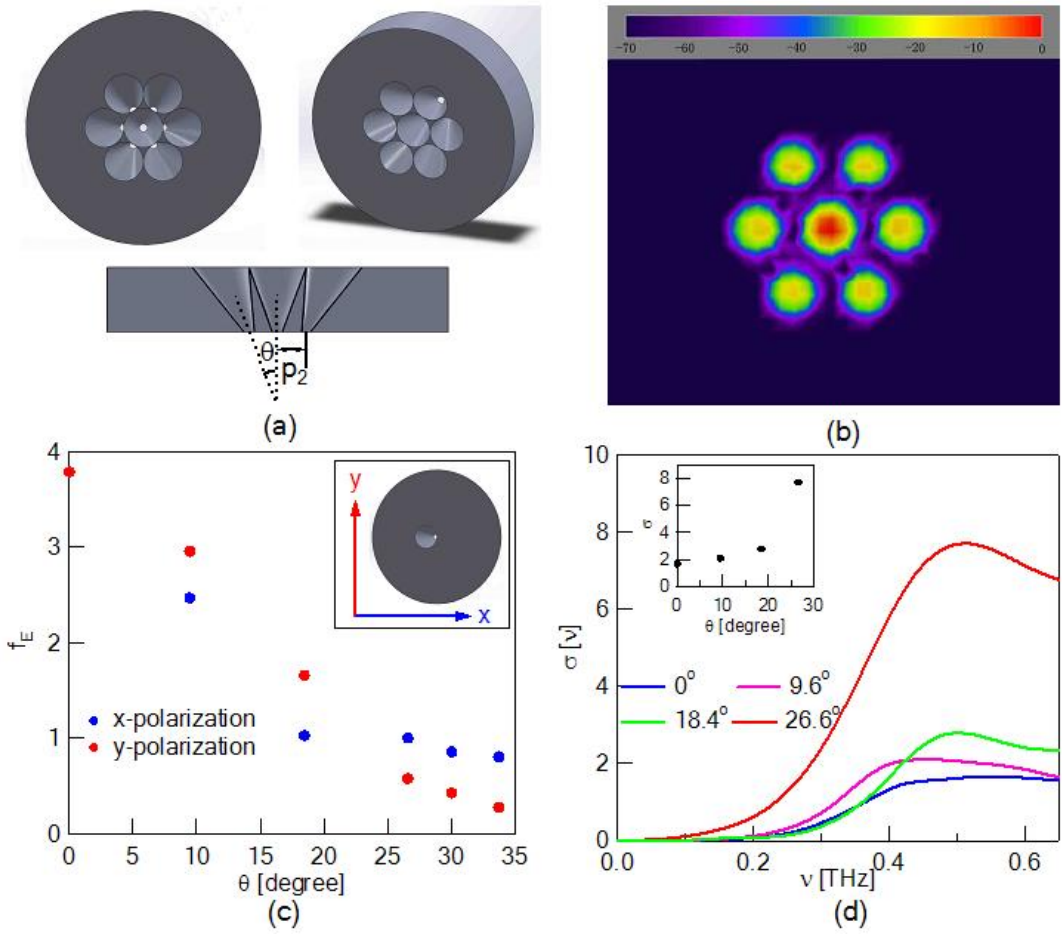

Figure 8.3. Numerical simulations of structures designed for tighter field focusing. (a) Schematic diagram of the hexagonal tapered aperture array with seven apertures, where the axes of the outer apertures were tilted with an inclination angle, θ. The reduced spacing of the output apertures, p_2, is shown in the top view on top left, cross-section on the bottom and isometric view on top right. For all the apertures, the input diameter, D_1', is 2 mm and the output diameter, D_2, is 400 μm. (b) A snapshot of the planar electric field distribution near the output surface. (c) Maximum value of f_E calculated for an individual TA with tilted axes of different inclination angles, θ, for the two orthogonal THz field polarizations. (d) Spectra of field concentration density, σ(ν), of TA arrays for various θ as given. The inset shows the maximum σ value extracted from σ(ν) at various values of θ.

independent of the polarization and the two orthogonal polarizations exhibit identical characteristics, as expected. As the incline angle increases, f_E becomes increasingly smaller. Interestingly, y-polarized radiation exhibits higher throughput for low tilt angles and there is a crossover between $20°$ and $25°$. This behavior is reversed for TAs tilted along the y-axis, as expected by symmetry. We expect that this crossover is related to the reflection properties associated with the two polarizations.

We now consider the concentration properties of a TA array that consists of 7 TAs placed in a hexagonal geometry with variable tilt angles. The issue now is not simply calculating the concentration enhancement, f_E, of the array, but rather whether that enhanced transmission can be focused to a smaller output area. Therefore, we define a spectral field concentration density, given by

$$\sigma(\nu) = \frac{f_E(\nu)}{\lambda^2}, \tag{8.3}$$

where ℓ is the longest distance in the array between centers of the output apertures. For a hexagonal lattice that contains only 7 TAs, $\ell = 2p_2$. In Fig. 8.3(d), we show the spectra of the field concentration density, as a function of the tilt angle, θ. If we consider the maximum value of $\sigma(\nu)$, which we define as σ, it increases with increasing tilt angle, as shown in the inset of Fig. 8.3(d), despite the fact that the propagation throughput becomes progressively reduced.

The notion that an array based on tilted TAs can be used to concentrate and focus radiation suggests that cascaded structures may be useful in increasing the optical throughput further. In Fig. 8.4, we sketch one possible example of such a combination. More generally, through appropriate design, the TA array in the top layer could be used to focus the field into the input aperture in the lower layer. Such an approach may circumvent practical limitations and allow for greater flexibility in the design of

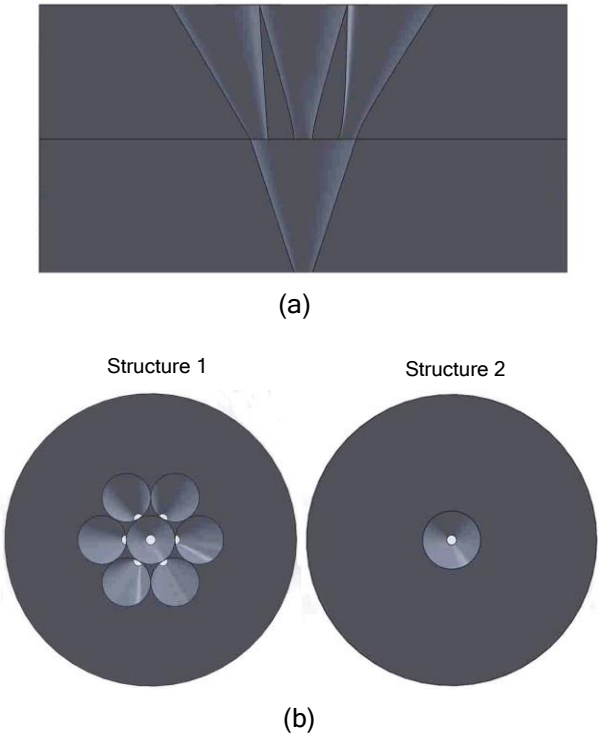

Figure 8.4. Schematic diagram for a proposed cascaded taper structure. (a) Cross-section of the structure. The diameter of the input aperture (2.4 mm) on the bottom layer is equal to the longest distance between the edges of the output apertures on the top layer. (b) Analysis of the structure into two sections: Structure 1 consists of seven tapered apertures forming a hexagonal array with input aperture diameters of 2 mm, output aperture diameters of 400 μm and axis inclination angle of 18.4°; Structure 2 consists of a single tapered aperture with input aperture diameter of 2.4 mm, output aperture diameter of 400 μm and taper full angle of 36.9 °.

structures for the concentration of radiation.

8.4 Conclusion

In summary, we have demonstrated experimentally that periodic arrays of tapered apertures are able to concentrate broadband THz radiation. With the optimal taper angle we studied earlier, we constructed a hexagonal lattice of nineteen TAs that led to a factor of ~ 10 increase in the broadband THz throughput for frequencies above the effective cutoff frequency. Further concentration of the transmitted radiation with higher field density was shown to be possible by tilting the apertures in an array toward the array center. Such a demonstration suggests that cascaded TA structures may allow for an even greater level of field concentration than any single layer structure is capable of providing.

8.5 References

1. E. Betzig, M. Isaacson, and A. Lewis, "Collection mode near-field scanning optical microscopy," Appl. Phys. Lett. **51**, 2088-2090 (1987).

2. S. Hunsche, M. Koch, I. Brener, and M. C. Nuss, "THz near-field imaging," Opt. Comm. **150**, 22-26 (1998).

3. M. Diwekar, S. Blair, and M. Davis, "Increased light gathering capacity of sub-wavelength conical metallic apertures," J. Nanophoton. **4**, 043504/1-11 (2010).

4. J. Beermann, T. Søndergaard, S. M. Novikov, S. I. Bozhevolnyi, E. Devaux, and T. W. Ebbesen, "Field enhancement and extraordinary optical transmission by tapered periodic slits in gold films," New J. Phys. **13**, 063029 (2011).

5. S. Liu, Z. V. Vardeny, and A. Nahata, "Concentration of broadband terahertz radiation using a periodic array of conically tapered apertures," Opt. Express **21**(10), 12363-12372 (2013).

6. T. Thio, H. F. Ghaemi, H. J. Lezec, P. A. Wolff, and T. W. Ebbesen, "Surface-plasmon-enhanced transmission through hole arrays in Cr films," J. Opt. Soc. Am. B **16**, 1743–1748 (1999).

7. H. Cao, A. Agrawal, and A. Nahata, "Controlling the transmission resonance lineshape of a single subwavelength aperture," Opt. Express **13**, 763-769 (2005)

8. N. Marcuvitz, *Waveguide Handbook* (New York: McGraw-Hill, 1951).

9. A. Agrawal, Z. V. Vardeny, and A. Nahata, “Engineering the dielectric function of plasmonic lattices,” Opt. Express **16**, 9601-9613 (2008).

CHAPTER 9

TRANSMISSION BLEACHING AND COUPLING CROSSOVER IN A SPLIT TAPERED APERTURE

9.1 Introduction

Conically tapered metallic apertures have been widely used in the area of near-field optical microscopy to enhance the lateral imaging resolution beyond the diffraction limit [1]. Tapered metal-clad waveguides have also been used to improve the coupling between devices with different allowed modes [2-4]. In these implementations, the output dimension and mode overlap are usually the parameters of primary concern. However, such tapered structures also allow for concentration of the incident radiation [5-7]. With this latter application in mind, a number of different approaches have been implemented using tapered wires [6-10], holes [11-13] and plates [5,14-16].

Although localization of radiation in two-dimensions has been demonstrated in tapered wires [8-10] and tapered plate waveguides [15,16], tapered apertures (TAs) can, in principle, more tightly confine such radiation based on the geometry of the output surface. Given the rather simple nature of the aperture on the output surface of a TA, the addition of other geometrical features within the structure may yield valuable new capabilities. Examples include the introduction of splits, slots, and corrugated features [17-19]. In the case where the TA has been split [17], the resulting structure has been used to apply a strongly localized in-plane electrical field while maintaining a relatively small spot size, whereas in the latter two cases [18,19], the modifications on the

metalized surface were used to detect the magnetic field with high spatial resolution.

While such additional features offer the likelihood of new functionalities, a simple TA suffers from the fact that the closed circular nature of the opening imposes a cutoff frequency associated with the aperture diameter. More generally, any aperture fabricated using a single continuous conductor (i.e., no electrical discontinuities) cannot support the propagation of a transverse electromagnetic (TEM) mode [20]. However, when two conductors are electrically separated, as is the case with a parallel plate waveguide or two needles, broadband TEM mode propagation can be supported [21-23]. Thus, the inclusion of a split into a TA may be able to combine the advantages associated with cylindrical TAs and parallel plate waveguides, allowing for high field concentration (and, thus, high field transmission) and broadband operation. We note that in previous work with similar structures [17-19], the spectral transmission properties were not explored. Thus, in order to fully utilize such structures, it is essential to explore their properties in greater detail.

We experimentally and numerically characterized the transmission properties of a conical TA in a 3-mm-thick metallic plate split in two halves with a variable distance gap between them. We used THz time-domain spectroscopy (THz-TDS) to characterize the spectral response of the transmitted radiation and find that the introduction of a gap reduces the cutoff effect that exists for a TA with no gap. Nevertheless, for small gap spacings (~ 10 μm), we found that the cutoff effect was still clearly present. As the separation between the two halves increases to ~ 30 - 40 μm, the bandwidth of the transmitted radiation broadened dramatically due to transmission of the field components below the cutoff of the TA. The transmitted pulse spectrum could be described as a superposition of the TA spectrum and the parallel plate waveguide (PPWG) spectrum. The gap, however, also introduced a channel for the radiation to escape from the aperture,

limiting the degree of the field confinement. We proposed a conical shell structure made of two isolated halves to minimize the radiation leakage and found that a high level of field confinement was possible. We confirmed these conclusions using numerical simulations to model the transmitted THz electric field properties.

9.2 Experimental Details

We fabricated two separate devices for this work. The first device was a conical TA fabricated in a 3-mm-thick stainless steel plate, which was used as a reference. It consisted of a circular input aperture with a diameter, D_1, of 2.0 mm, a circular output aperture with a diameter， D_2， of 400 μm, and a taper full angle, α, of 30°, which we have previously found to be the optimal taper angle [13]. The second structure was nearly identical to the first. However, in this case, the stainless steel plate was initially cut into two pieces, polished, and clamped together, so that a TA identical to the reference and centered on the gap between the two pieces could be fabricated. Both samples are shown schematically and graphically in Figs. 9.1(a) and 9.1(b). Finally, we used two polished 3-mm-thick stainless steel plates to create a PPWG with variable spacing (not shown).

The structures were characterized experimentally using a conventional THz-TDS setup, as shown schematically in Fig. 9.1(c). Details of the experimental setup and the advantageous properties of this approach have been discussed previously [24]. Photoconductive devices were used for both emission and coherent detection. An off-axis paraboloidal mirror was used to collect and collimate the THz radiation as it propagated from the emitter to the sample, resulting in a 1/e beam diameter of ~ 5 mm that was normally incident onto the input surfaces of the structures. In all cases, the incident and transmitted THz radiation was polarized perpendicular to the gap. It is worth noting that the beam size was larger than the cross-sectional area of the input aperture but smaller

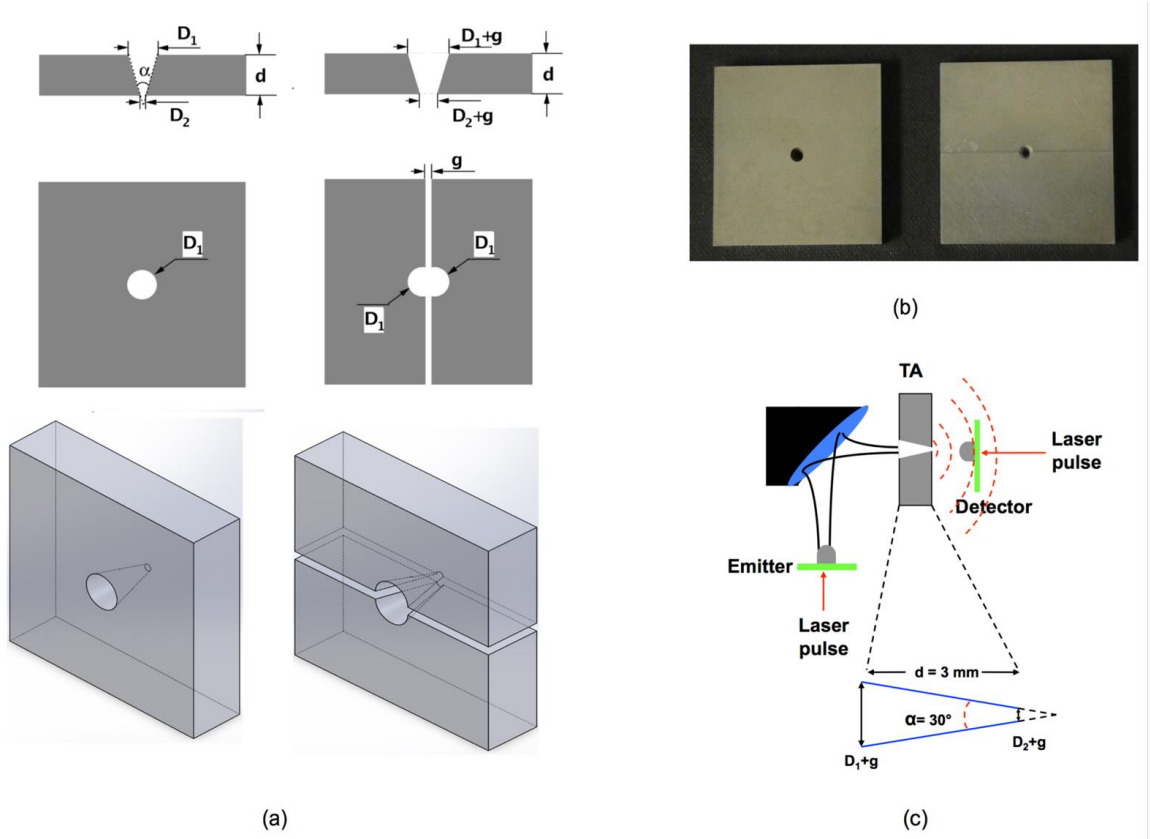

Figure 9.1. Details of the experimental design. (a) Schematic diagram of the different aperture structures studied. Left: cross-section (top), top view (middle) and perspective view (bottom) of the reference TA with an input aperture diameter, D_1 = 2.0 mm, an output aperture diameter, D_2 = 400 μm, and metal thickness, d = 3.0 mm. Right: cross-section (top), top view (middle) and perspective view (bottom) of the split TA with the same dimensions as the reference TA but split into two halves. The two halves of the aperture are separated by a variable gap spacing, g. (b) Photographs of the reference TA and the split TA (with $g \approx 0$). (c) Schematic diagram of the THz time-domain spectroscopy system. A collimated THz beam was normally incident on the sample. The radiated electromagnetic wave was detected using a photoconductive device for coherent broadband THz detection.

than the opening of the holder. For the split TA, one half of the structure was attached to a holder while the other half was attached to a precision translation stage, creating a variable gap spacing, g, as labeled in Fig. 9.1(a). When the two halves were brought together, such that g = 0, the resulting TA was nearly identical to the reference TA. For reference purposes, we also measured the field transmission through the PPWG, with the same gap spacing, g, used for the split TA, under the same experimental conditions. Coherent THz radiation transmitted from the output opening of the structures was focused onto a 9-mm-diameter hyper-hemispherical-silicon-lens-coupled photoconductive dipole detector that was located ~ 10 mm from the output face of the apertures. The detected transient photocurrent was then Fourier transformed, yielding a transmitted electric field spectrum in the range of ~ 0.05 - 0.8 THz. We did not normalize the observed transmission spectra using a reference aperture in a thin metal plate, as we have done in prior work [13], since the aperture geometry changes with the gap spacing and the small spatial differences between such apertures are difficult to fabricate accurately. Nevertheless, the notion of a relative electric field concentration factor can still be discussed.

We also performed numerical finite-difference time-domain (FDTD) simulations of the propagation properties. In the simulations, the metal was modeled as a perfect electrical conductor (PEC), since metal conductivities are typically high at THz frequencies, while the surrounding dielectric medium was assumed to be air. We set the spatial grid size to be 10 μm, which was necessary to ensure convergence of the numerical calculations, and modeled all boundaries with Liao-absorbing boundary conditions. For the input electric field, we used a plane wave with the time-domain waveform described by the first derivative of a Gaussian pulse. The resulting bipolar

waveform had the same bandwidth and approximately the same pulse shape as was available in the experimental work. All of the simulated results were recorded at specific spatial points in the vicinity of the output plane of the structure or integrated across the area of the output aperture.

9.3 Experimental Results, Simulation and Discussion

Figure 9.2 summarizes the essential characteristics of the split TAs when varying the gap spacing, g. In Fig. 9.2(a), we show the transmitted spectral amplitude of the split TAs with several different gap spacings, g, as well as the spectra for the incident pulse (no sample), reference TA, and PPWG with a 10-μm gap. There are a few points to be made regarding these data. Consistent with our earlier measurements [13], the reference TA exhibits strong transmission suppression below ~ 0.3 THz, with an effective cutoff frequency that appears to be red-shifted compared to that of a 400-μm-diameter straight cylindrical aperture [$\nu_c = 1.841c/(\pi D_2) = 0.44$ THz, where c is the speed of light in vacuum] [25]. When g = 0 μm, the maximum transmission occurs at ~ 0.4 THz. Though not discussed here, this corresponds to a field concentration factor of ~ 4, well above the cutoff frequency, which is consistent with our earlier findings [13]. As the gap spacing increases, the peak transmission at ~ 0.4 THz steadily decreases (i.e., we observe transmission bleaching), even though the effective aperture area increases. This is discussed in greater detail below. Although we would expect to obtain identical spectra for the reference TA and the split TA with g = 0 μm gap, there is a small difference in the spectral properties, as shown in Fig. 9.2(a). We attribute this small difference to a minor misalignment in our experimental setup that lies within the precision with which we can align these two halves. As expected, the spectrum associated with the PPWG looks nearly identical to that of the incident waveform, demonstrating that it supports broadband THz

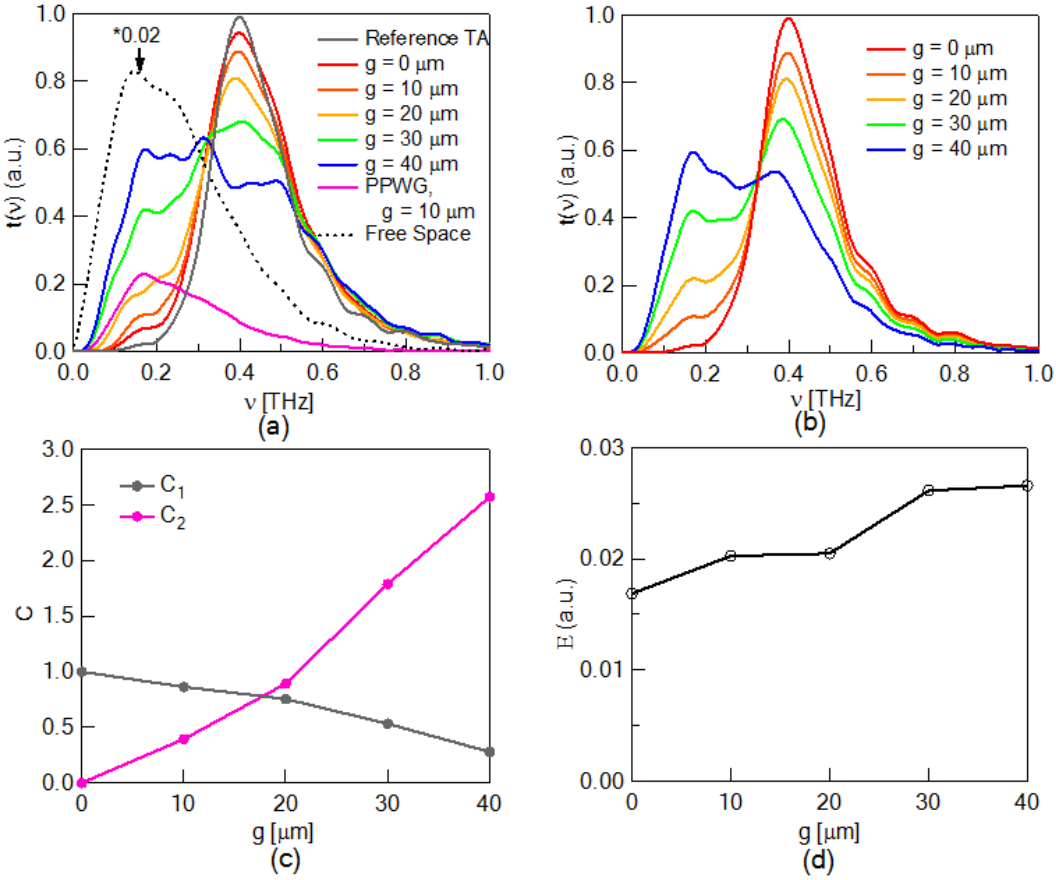

Figure 9.2. Experimentally measured spectral transmission properties of the split TA structures. (a) Amplitude spectra, t(ν), of the split TAs as a function of the gap spacing, g, as well as for the incident pulse (measured without a sample), reference TA, and a parallel plate waveguide with a gap of 10 µm. (b) Analytically calculated spectra using the spectral amplitude of the reference TA and parallel plates in Fig. 9.2(a). (c) Coupling coefficients used to model the spectra in Fig. 9.2(b). (d) Energy averaged over the input opening area, calculated from Fig. 9.2(a). The lines in Fig. 9.2(c) and Fig. 9.2(d) are only guides to the eye.

propagation. In addition, the transmission peak associated with the PPWG at ~ 0.17 THz has a larger magnitude than the split TA with g = 10 μm at the same frequency. We attribute this to the fact that a large fraction of the PPWG cross-sectional area is covered by the input aperture in the split TA, minimizing the TEM mode contribution when g = 10 μm.

From a theoretical standpoint, any separation between two conductors should allow for the propagation of TEM waves [21]. However, the coupling efficiency of the TEM mode is not necessarily constant as the separation between the conductors is varied. When the gap is very small, i.e., g = 10 μm or g = 20 μm, frequencies below 0.3 THz are only slightly enhanced. As g is increased further (g > 30 μm), the transmission becomes increasingly broadband with a corresponding reduction in the magnitude of the peak transmission amplitude. In all cases, the high frequency roll-off arises from the frequency response associated with the photoconductive emitter-detector pair in the THz-TDS system.

In order to understand the experimental observations, we analytically reproduced the spectral amplitude t(ν) of the split TA for each value of g using only the spectra of the reference TA, $t_1(\nu)$, and the PPWG, $t_2(\nu)$, both from Fig. 9.2(a), using the relation:

$$t(\nu) = C_1 t_1(\nu) + C_2 t_2(\nu). \tag{9.1}$$

Here, C_1 and C_2 are the coupling coefficients of $t_1(\nu)$ and $t_2(\nu)$, respectively. Using this equation, we display the resulting spectra in Fig. 9.2(b) and the corresponding coefficients in Fig. 9.2(c). The spectra in Fig. 9.2(b) agree well with those in Fig. 9.2(a) and the coefficients as a function of gap spacing vary almost linearly. Thus, we can regard the split TA as a superposition of a complete TA and a PPWG. Importantly, there is a crossover in the magnitude of the coupling coefficients that appears to occur at g ≈

18 μm, though the reason why it occurs for this gap spacing is unclear.

Since we are unable to directly obtain the field concentration values for each value of g, an alternate method for gaining insight into the problem is to consider the normalized (to area) spectral transmission. We can define a normalized spectral energy, E_N, as the total spectral energy divided by the cross-sectional area. Ignoring any constants of proportionality,

$$E_N = \frac{\int |t(\nu)|^2 d\nu}{A}, \tag{9.2}$$

where t(ν) is the measured spectral amplitude and A is the illuminated input aperture area, given by $A = \pi\left(\frac{D_1}{2}\right)^2 + g \times d$ (d = 5 mm is the 1/e beam diameter). The calculated data are shown in Fig. 9.2(d). The fact that E_N increases with increasing values of g indicates that the overall coupling of free-space radiation to the structure is enhanced as the gap becomes larger. Thus, the reduction in the peak transmission amplitude is not due to reduced coupling of radiation into the structure. The reduction is more likely associated with coupling of the pulse energy from the aperture into the gap between the plates as the pulse travels inside the cone of the TA. An analogous process occurs in a PPWG where radiation can leak from the finite edges of the structure into free space and also back to the aperture area [26].

To further explore the properties of this structure and validate the experimental findings, we performed numerical 3D FDTD simulations. In Fig. 9.3(a), we show the simulated transmission of the reference TA, the PPWG with 10-μm gap and the split TAs with gap spacings of 10 μm, 30 μm, 60 μm and 100 μm. Although there are some differences in the spectral amplitudes between experiment and simulation, it is clear that the spectra shown here are in good qualitative agreement with the spectra obtained

Figure 9.3. Numerical simulations of the field properties for split TAs and relevant stretched TAs. (a) Amplitude spectra t(ν) for split TAs with g = 0, 10, 30, 60 and 100 μm and the parallel plates with g = 10 μm. (b) Analytically calculated spectra using the spectral amplitude of the reference TA and parallel plates in Fig. 9.3(a). (c) Corresponding coefficients used in Fig. 9.3(b). The lines are only guides to the eye. (d) Transmitted field amplitude, t(ν), of the stretched TAs with various elongation, s. Inset: top view of the stretched TA with marked dimensions. (e) and (f) Snapshots of the magnitude of the transverse electric field perpendicular to the gap in the vicinity of the output aperture of a reference TA and a split TA with g = 60 μm. The white region is metal modeled as perfect electrical conductor.

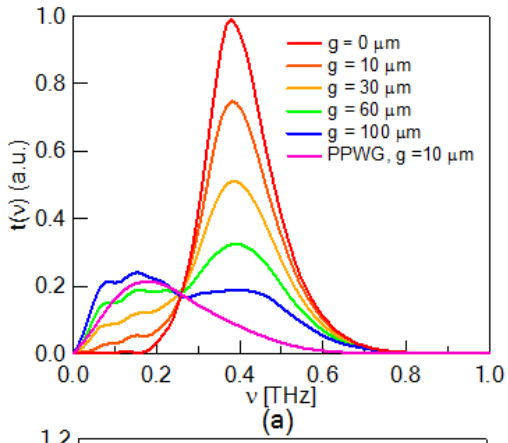
g = 0 μm
g = 10 μm
g = 30 μm
g = 60 μm
g = 100 μm
PPWG, g =10 μm
t(ν) (a.u.)
ν [THz]

(a)

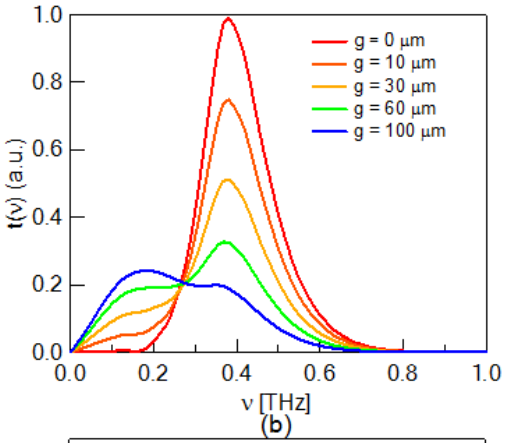
g = 0 μm
g = 10 μm
g = 30 μm
g = 60 μm
g = 100 μm
t(ν) (a.u.)
ν [THz]

(b)

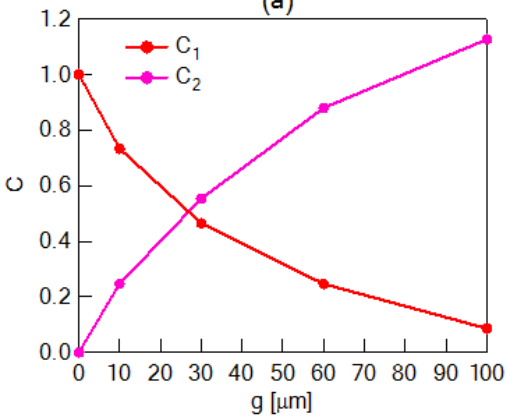
C1
C2
C
g [μm]

(c)

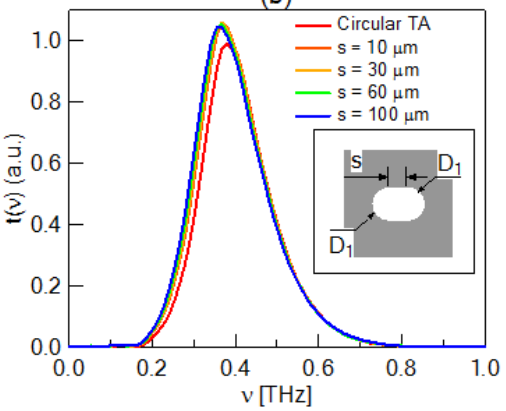
Circular TA
s = 10 μm
s = 30 μm
s = 60 μm
s = 100 μm
s
D1
D1
t(ν) (a.u.)
ν [THz]

(d)

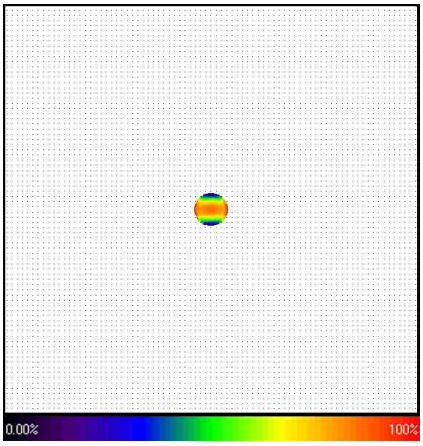
0.00%
100%

(e)

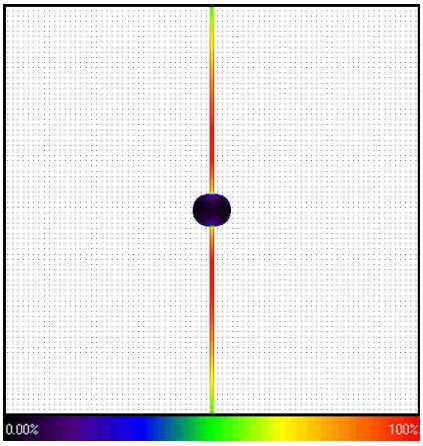
0.00%
100%

(f)

experimentally. The differences may result from how the detection takes place in the experiment and in the simulations: the detected signal was measured at only one point in the numerical simulations, while the silicon lens attached to the dipole detector in the experimental setup integrated the transmitted radiation over a larger solid angle.

In order to demonstrate that these data also correspond to the superposition of two modes (those associated with the TA and the PPWG), we once again reconstructed all of the other waveforms ($g \neq 0$) in Fig. 9.3(a) using Eq. (9.1). The resulting waveforms are shown in Fig. 9.3(b) and match the simulation results in Fig. 9.3(a) quite well. The resulting coupling coefficients, shown in Fig. 9.3(c), differ numerically from the values found experimentally, but show the same trend with g and also show a coupling cross-over at a similar value of g.

Since the gap spacing not only increases the input aperture area, but also changes the shape of the circular aperture, we also investigated whether or not any induced ellipticity in the aperture shape accounts for the decreased transmission in the vicinity of the peak concentration frequency (~ 0.4 THz). In the numerical simulations, a stretched TA was obtained by moving the two halves of the circular aperture apart by a distance s and filling the gap in the sidewalls with a metal assumed to be a perfect electrical conductor, leaving the taper angle unchanged. A top view of the structure is sketched in the inset of Fig. 9.3(d), while the main figure [Fig. 9.3(d)] shows the spectral transmission properties of the stretched TAs for s = 0, 10, 30, 60 and 100 μm. It is apparent that the introduction of a minor ellipticity in the aperture has minimal effect on the transmission spectra.

Moreover, we observed the field distribution in both the reference TA and split TAs through the FDTD simulation. In Figs. 9.3(e) and 9.3(f), we exhibit the snapshots of

the electric field distribution on the output surface of a reference TA and a split TA. It is obvious that the radiation is well confined in the aperture area of the reference TA in Fig 9.3(e). Also, Figure 9.3(f) confirms our conjecture that a large portion of the radiation propagating in the conical aperture is coupled into the gap and therefore the concentration effect in the tapered aperture is undermined.

Using our findings to this point, we now consider if any split TA geometry can be used to combine the beneficial properties of a TA and a PPWG. In the split TA embodiments used up to this point, we fabricated the structure in a larger metal block. This allowed for much of the radiation to be coupled to a TEM mode and to be distributed over a relatively large cross-sectional area. We now consider a split TA, in which the wall thickness of the aperture is small (less than the aperture diameter), as shown in Fig. 9.4(a). Since fabrication of such a structure, which we refer to as a split shell TA, is technically challenging, we performed only numerical simulations. In Fig. 9.4(b), we display a snapshot of the electric field pattern on the output surface of the split shell TA with a 60-μm gap. Although the structure will be prone to the same coupling cross-over process as in the earlier implementations, the electric field is more localized in the shell geometry. As a consequence, the resulting output transmission spectra, shown in Fig. 9.4(c), exhibits significantly higher magnitude than the simple split TA. More importantly, it exhibits the peak transmission amplitude that is close to that of the reference TA, though with a much broader bandwidth. In order to further confirm the functionality of the split shell TA and allow for quantitative comparisons with experimental results, we integrate the electric field magnitude on the planes just inside the input aperture and those just outside the output aperture for each grid element within the mesh, and divide them by the relevant cross-sectional area of the input or output

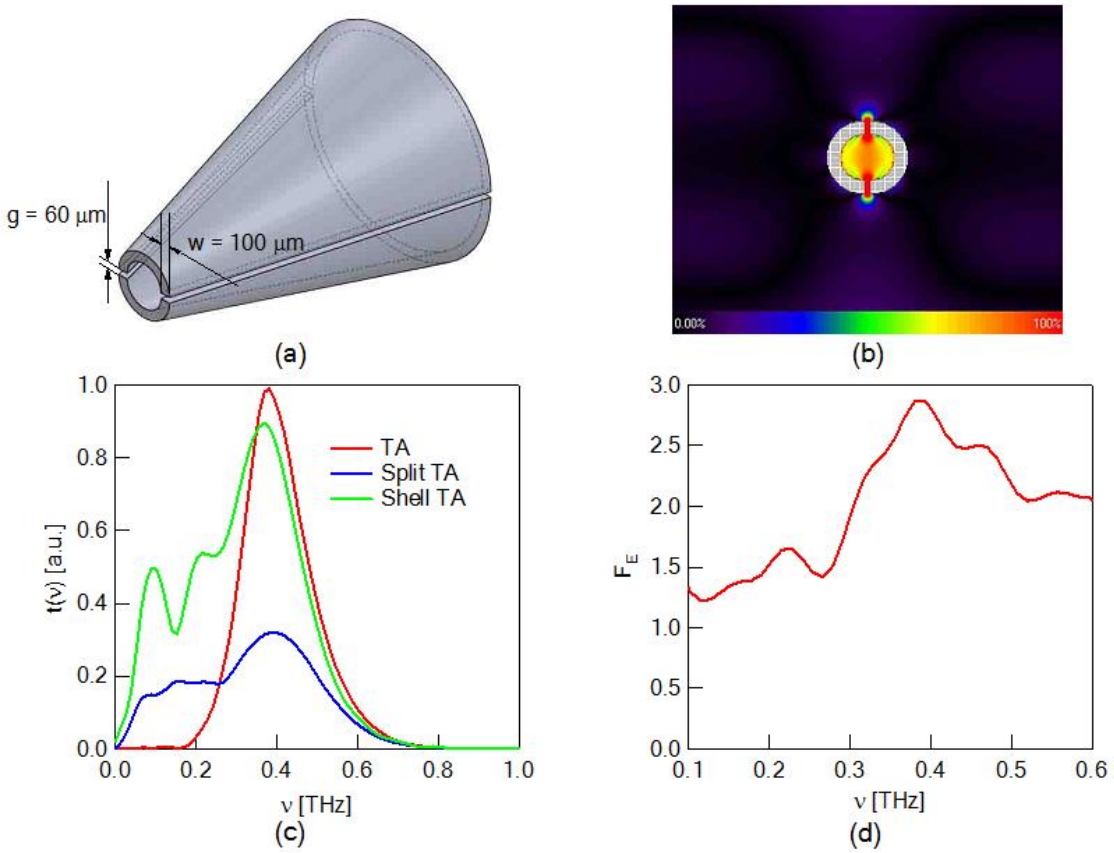

Figure 9.4. Numerical simulations of the split shell TA. (a) Schematic diagram of a split shell TA, in which the wall thickness of the aperture is small. (b) Snapshot of the magnitude of the transverse electric field perpendicular to the gap in the vicinity of the output aperture of a split shell TA. The white region is metal modeled as perfect electrical conductor. (c) Transmission spectra for the split shell TA, as well as the spectra associated with the simple split TA and the reference TA (from Fig. 9.3). (d) Electric field throughput concentration factor (F_E) obtained by integrating the field on the input and output planes of the TA and normalized by the opening area of the corresponding input and output surfaces.

aperture. This ratio, referred to as $F_E(\nu)$, is similar to the concentration factor we defined in earlier work with similar structures [11,13] and is effectively an electric field throughput concentration factor. As seen in Fig. 9.4(d), $F_E(\nu)$ demonstrates that this shell TA allows for concentration of the incoming THz electric field over a broad range of frequencies.

9.4 Supplementary Information: Comparison between Tapered Apertures and a Conventional Lens

In order to clarify the practical significance of such a split shell TA in Fig. 9.4(a), we also numerically calculated the intensity density of our structure on the output plane, and compared it with the theoretically calculated intensity density on the focus through a conventional focusing lens, taking the 1/e beam diameter of the terahertz beam in our system which is ~ 5 mm.

For the split shell TA, the time-domain signal was detected at each meshing grid of the output opening in the output plane. Then the signal waveforms were Fourier transformed and squared at each frequency point to get the required intensity. Finally, all the output intensity data were also summed at each frequency point, and divided by the corresponding area of the output aperture to define the intensity density. Therefore, the output intensity density of the split shell TA, $Ia(\nu)$, is defined as the total output spectral intensity divided by the cross-sectional area of the output opening,

$$Ia(\nu) = \frac{\sum_i [t_i(\nu)]^2}{\left[\frac{2 \times g \times w + \pi (D_2/2)^2}{a^2}\right]}, \tag{9.3}$$

where $t_i(\nu)$ is the measured spectral amplitude at the ith grid, g = 60 μm is the gap spacing between the two halves of the TA, w = 100 μm is the wall thickness [see Fig. 9.4(a), and a is the side length of each mesh grid, so the denominator indicates the

relative area of the output opening.

In the case of the conventional lens, a TPX lens was employed with the minimum available focal length, f_0 = 25 mm, and a large enough span to effectively focus the beam. In Fig. 9.5(a), the input beam waist was labeled as w_{01} = (5/2) = 2.5 mm, which is half of the 1/e beam diameter, and the focused beam waist was w_{02}. Supposing that the input intensity is homogeneously distributed on the input area and the beam follows the focusing theory of a Gaussian beam,

$$w_{02} = \frac{2\lambda}{\pi}\frac{f_0}{2w_{01}}, \tag{9.4}$$

so we can define the intensity density at the focus of a conventional lens as

$$Ia_0(\nu) = \frac{\frac{\pi {w_{01}}^2}{a^2} \times [t_0(\nu)]^2}{\frac{\pi {w_{02}}^2}{a^2}} = \frac{{w_{01}}^4 \pi^2 \nu^2 [t_0(\nu)]^2}{c^2 {f_0}^2}. \tag{9.5}$$

Here, $t_0(\nu)$ is the input wave spectral amplitude at a single grid, the free space wavelength is $\lambda = c/\nu$ (c is the speed of light in vacuum), and again a is side length of each mesh grid. The calculated intensity densities are shown in Fig. 9.5(b) and the plot associated with the lens is scaled by a factor of 10. Although the input opening of our structure was smaller than the input beam, the intensity density through the TA was still around 10 times larger than that focused by a conventional lens.

9.5 Conclusion

In summary, we experimentally characterized the spectral properties of a split tapered aperture that incorporated a variable spacing gap between the two halves of the metallic screen in order to eliminate the aperture cutoff effect and enable broadband confinement of THz pulses. However, we found that the peak spectral transmission was

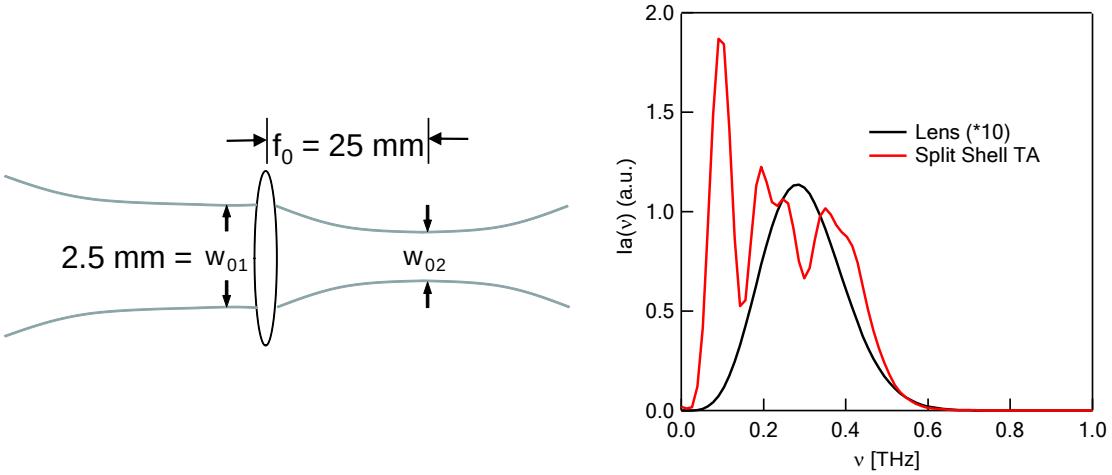

(a) (b)

Figure 9.5. Comparison of the concentration capabilities between the split shell TA and a conventional focusing lens. (a) Schematic diagram of Gaussian beam focused by a lens when the input beam waist is w_{01} and focal-plane beam waist is w_{02}. (b) Intensity densities calculated for a split shell TA with wall thickness of 100 μm and gap spacing of 60 μm, and a focusing lens with a focal length of 25 mm.

greatest when there was no gap and that the peak decreased steadily as the gap spacing was increased. Correspondingly, there was a crossover in the coupling coefficient between the TA mode and a TEM mode. This was verified both experimentally and numerically. Interestingly, we also found that an alternate embodiment of the split TA, one in which the wall thickness was small, appeared to do a better job of concentrating radiation (maintaining a relatively small spot size) while allowing for more broadband radiation to be transmitted. Moreover, we proved that such a structure also led to a greater concentrated intensity compared with a conventional optical focusing lens under the same circumstances. Therefore, such approaches may be useful in developing structures that enable high concentrations of truly broadband radiation.

9.5 References

1. D. W. Pohl, W. Denk, and M. Lanz, "Optical stethoscopy: Image recording with resolution λ/20," Appl. Phys. Lett. **44**(7), 651-653 (1984).

2. L. Chen, J. Shakya, and M. Lipson, "Subwavelength confinement in an integrated metal slot waveguide on silicon," Opt. Lett. **31**(14), 2133–2135 (2006).

3. P. Ginzburg, D. Arbel, and M. Orenstein, "Gap plasmon polariton structure for very efficient microscale-to-nanoscale interfacing," Opt. Lett. **31**(22), 3288–3290 (2006).

4. S. Kim, E. Lee, Y. Ji, and T. Jeon, "Improvement of THz coupling using a tapered parallel-plate waveguide," Opt. Express **18**(2), 2779–2783 (2010).

5. K. V. Nerkararyan, "Superfocusing of a surface polariton in a wedge-like structure," Phys. Lett. **A 237**(1-2), 103–105 (1997).

6. A. J. Babadjanyan, N. L. Margaryan, and K. V. Nerkararyan, "Superfocusing of surface polaritons in the conical structure," J. Appl. Phys. **87**(8), 3785-3788 (2000).

7. M. Stockman, "Nanofocusing of optical energy in tapered plasmonic waveguides," Phys. Rev. Lett. **93**(13), 137404 (2004).

8. Y. Bin Ji, E. S. Lee, J. S. Jang, and T. I. Jeon, "Enhancement of the detection of THz Sommerfeld wave using a conical wire waveguide," Opt. Express **16**(1), 271–278 (2008).

9. M. Awad, M. Nagel, and H. Kurz, "Tapered Sommerfeld wire terahertz near-field

imaging," Appl. Phys. Lett. **94**(5), 051107 (2009).

10. V. Astley, R. Mendis, and D. M. Mittleman, "Characterization of terahertz field confinement at the end of a tapered metal wire waveguide," Appl. Phys. Lett. **95**(3), 031104 (2009).

11. T. D. Nguyen, Z. V. Vardeny, and A. Nahata, "Concentration of terahertz radiation through a conically tapered aperture," Opt. Express **18**(24), 25441–25448 (2010).

12. M. C. Schaafsma, H. Starmans, A. Berrier, and J. Gómez Rivas, "Enhanced terahertz extinction of single plasmonic antennas with conically tapered waveguides," New J. Phys. **15**(1), 015006 (2013).

13. S. Liu, Z. V. Vardeny, and A. Nahata, "Concentration of broadband terahertz radiation using a periodic array of conically tapered apertures," Opt. Express **21**(10), 12363-12372 (2013).

14. A. Rusina and M. Durach, "Nanoconcentration of terahertz radiation in plasmonic waveguides," Opt. Express **16**(23), 1377–1386 (2008).

15. H. Zhan, R. Mendis, and D. M. Mittleman, "Superfocusing terahertz waves below λ/250 using plasmonic parallel-plate waveguides," Opt. Express **18**(9), 9643–9650 (2010).

16. K. Iwaszczuk, A. Andryieuski, A. Lavrinenko, X.-C. Zhang, and P. U. Jepsen. "Terahertz field enhancement to the MV/cm regime in a tapered parallel plate waveguide," Opt. Express **20**(8), 8344–8355 (2012).

17. B. Clark, M. P. Taylor, and H. D. Hallen, "Novel split-tip proximal probe for fabrication of nanometer-textured, in-plane oriented polymer films," J. Vac. Sci. Technol. B **28**(4), 687-692 (2010).

18. M. Burresi, D. van Oosten, T. Kampfrath, H. Schoenmaker, R. Heideman, A. Leinse, and L. Kuipers, "Probing the magnetic field of light at optical frequencies," Science **326**(5952), 550–553 (2009).

19. T. J. Antosiewicz, P. Wr, and T. Szoplik, "Magnetic field concentrator for probing optical magnetic metamaterials," Opt. Express **18**(25), 25906–25911 (2010).

20. J. D. Jackson, *Classical Electrodynamics* (Wiley, 1999), p. 832.

21. Z. B. Popović and B. D. Popović, *Introductory Electromagnetics* (Prentice Hall, 2000), p. 556.

22. R. Mendis and D. Grischkowsky, "Undistorted guided-wave propagation of subpicosecond terahertz pulses," Optics letters **26**(11), 846–848 (2001).

23. O. Mitrofanov, C. C. Renaud, A. J. Seeds, "Terahertz probe for spectroscopy of sub-wavelength objects," Opt. Express **20**(6), 6197-6202 (2013).

24. H. Cao, A. Agrawal, and A. Nahata, “Controlling the transmission resonance lineshape of a single subwavelength aperture,” Opt. Express **13**(3), 763–769 (2005).

25. C. A. Balanis, *Advanced Engineering Electromagnetics* (John Wiley & Sons, 1989).

26. R. Mueckstein, M. Navarro-Cía, O. Mitrofanov, “Mode interference and radiation leakage in a tapered parallel plate waveguide for terahertz waves,” Appl. Phys. Lett. **102**(14), 141103 (2013).

CHAPTER 10

NEAR-FIELD IMAGING USING BROADBAND TERAHERTZ TRANSMISSION THROUGH TAPERED APERTURES

10.1 Introduction

The ability to obtain subdiffraction limited spatial resolution [1,2] has proven to be an important tool for a variety of spectroscopic and imaging applications. This is generally accomplished using a variety of aperture-based [3,4] and apertureless [5,6] approaches. In the former category, high spatial resolution is achieved by bringing a sharply tapered wire in close proximity to the sample. Electromagnetic radiation is then scattered off the tip of the (vibrating) wire. Such techniques can allow for very high spatial resolution, though the coupling (or scattering) efficiency tends to be low. In the terahertz (THz) spectral range, early work using this approach demonstrated spatial resolution on the order of $\lambda/1000$ [7], though more recent work has shown that significantly higher resolution is possible [8]. Aperture-based techniques, on the other hand, do not typically allow for the same level of spatial resolution, but benefit from comparatively high coupling efficiency in the structures. In the simplest embodiment, parallel plate waveguides with small plate spacings have been shown to allow for high spatial resolution along one axis [9]. In a variation on this idea, Zhan et al. showed that when the individual plates are tapered along both transverse axes, they could achieve better than $\lambda/145$ resolution along both axes [10]. It is worth noting that a variety of other structures have also been employed to perform near-field THz imaging [11-14].

In conventional optical near-field microscopy, high spatial resolution is commonly achieved by tapering an optical fiber and appropriately metallizing it such that there is a subwavelength aperture at the tip [15]. The aperture exhibits a cutoff frequency associated with the aperture diameter [16]. At optical frequencies, where narrowband lasers are typically used, the aperture does not introduce any spectral distortion and only acts to lower the overall transmissivity of the probe. Moreover, such conically tapered structures should, in principle, also exhibit concentration of the incident radiation [17]. However, the observation of such effects is complicated by the lossy nature of metals at visible frequencies. Although tapered apertures have previously been used for near-field THz imaging [18], we have recently investigated the detailed spectral and field concentration properties of conically tapered apertures [19-21]. These structures have been fabricated in a variety of different metals and all exhibit approximately similar behavior: (i) concentration of the incident THz electric field that was maximized for a taper full angle of 30°, (ii) a corresponding reduction in the THz group velocity propagating through the aperture, and (iii) a cutoff frequency, f_c, associated with the output aperture diameter that suppressed THz transmission for frequencies below f_c. Based on the last observation, we fabricated a tapered aperture in a metal block that was cut through the center of the aperture [20]. The rationale for introducing a gap in the aperture is that when such structures are not fully electrically connected, they may be able to support broadband transmission. This device was indeed capable of supporting broader bandwidth transmission. However, since the resulting device was effectively the superposition of a tapered aperture and a parallel plate waveguide, by virtue of being fabricated in a metal block, the introduction of even a very modest gap on the order of 10-20 μm allowed for a significant fraction of the field to be leaked into the gap (a

parallel plate propagating mode), destroying the spatial localization along that axis. Because of these issues, we proposed and showed numerically that a tapered aperture that was split in half, but with sidewalls that were thin (~ 60 μm) in the vicinity of the gap, would minimize those issues [20].

We describe the fabrication and experimental transmission properties of that structure, hereafter referred to as a split shell tapered aperture (SSTA), and demonstrate its utility for near-field imaging. The structure consists of two halves of a conically tapered aperture that can be positioned to have a variable gap. That fact, along with the fact that the sidewall thickness near the gap is small, allows for broadband transmission, preserves the high concentration factor, and allows for high spatial resolution set by the output aperture diameter. This is demonstrated using THz time-domain spectroscopy. Based on these results, we use the probe to image a U-shaped structure fabricated into a thin metal foil at several different frequencies above and below the cutoff frequency of the SSTA. Based on the promising results, further refinements in the structure and the system should allow for high signal-to-noise near-field imaging well below the cutoff frequency.

10.2 Experimental Details

We fabricated SSTAs using wire electrical discharge machining (wire EDM). Figure 10.1 shows schematic diagrams of the structure, along with the relevant geometrical parameters, and a photograph of the final probe. The SSTA was fabricated using a 3-mm-thick stainless steel plate that was cut into two pieces and polished. Each half of the tapered aperture was then fabricated with a taper half-angle, relative to the propagation axis, of 15 °. The bottom face of the probe was also tapered, with an angle of $\theta = 10$ °, relative to the top plane, to minimize contact between the probe and the sample

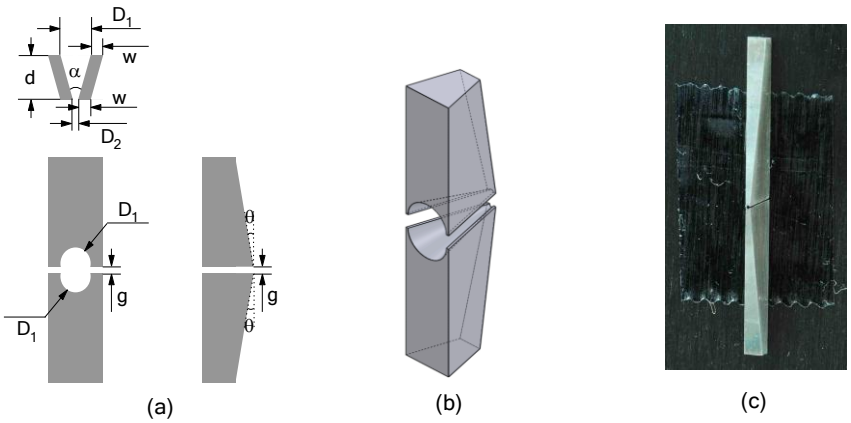

Figure 10.1. Details of the split shell tapered aperture (SSTA). (a) Schematic diagram of the SSTA. Cross-section (left top), top view (left bottom) and side view (right bottom) of the structure with an input aperture diameter, D_1 = 1.8 mm, an output aperture diameter, D_2 = 100 μm, probe length, d = 3.0 mm, and a taper full angle, α = 30 °. The two halves of the aperture are separated by a variable gap spacing, g. The bottom plane of the device is also cut with a tilted angle to the top surface, θ = 10°. The sidewall thickness at the gap on both sides is 60 μm. (b) Perspective view of the SSTA with a gap. (c) Photographs of the SSTA (with g ≈ 0). For the purposes of this image, the SSTA is attached to a planar surface using double-sided tape.

under test. The final device consisted of a conical TA with a circular input aperture of which the diameter, D_1 = 1.8 mm, length, d = 3.0 mm, and taper full angle, $\alpha = 30°$, which we have previously found to be the optimal taper angle [19]. The diameter of the circular output aperture was D_2 = 180 μm, corresponding to a cutoff frequency, f_c = 1 THz. Based on findings from earlier simulation work [20], we designed the thickness of the sidewalls near the gap to be 60 μm. The two halves of the device could be moved to allow for a variable gap, g. In all of the following work, the incident and transmitted THz radiation was polarized perpendicular to the gap.

We characterized the probes experimentally using THz time-domain spectroscopy with the setup shown in Fig. 10.2(a). The details of the system are described in Ref. [21] and discussed only briefly here. We used a photoconductive device to generate broadband THz radiation and a silicon lens to collect and focus the THz beam into the SSTA. The THz beam had a Gaussian spatial profile with a beam waist that occurred after the silicon lens at position A, as shown in Fig. 10.2(b). The input plane of the SSTA was placed at position B to ensure that the incident beam had a more uniform field distribution and that the beam size was larger than the input aperture of the SSTA. The two pieces of the SSTA were mounted on a rigid holder, which allowed the gap spacing, g, to be easily adjusted. The transmitted THz radiation was detected using a photoconductive dipole detector that had an integrated sub-wavelength aperture. This aperture was lithographically patterned above the dipole antenna and allowed for ~ 10 μm spatial resolution [21].

10.3 Experimental Results and Discussion

We initially measured the spectral transmission properties of the SSTAs with a 1.8-mm-diameter input aperture and a 180-μm-diameter output aperture for two different

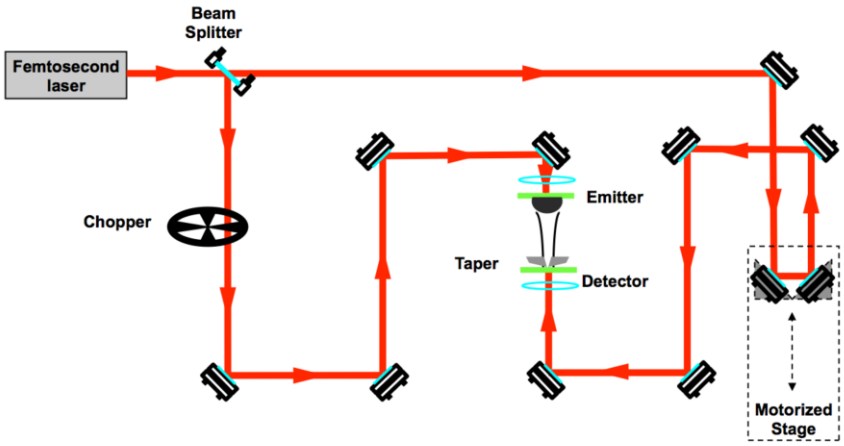

(a)

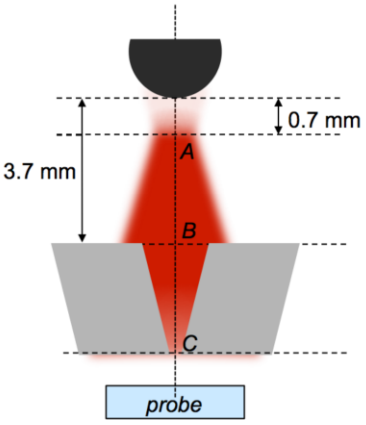

(b)

Figure 10.2. Schematic of experimental system and measured probe throughput properties. (a) Schematic diagram of the measurement system. Broadband THz radiation emitted from ZnTe was collected and focused using a spherical silicon lens and normally incident on the SSTA structure. The transmitted THz pulse was detected using a dipole antenna that had an integrated circular aperture and yielded 10-μm spatial resolution. (b) Enlarged diagram of the THz beam showing relevant positions of the components and the locations where measurements were taken.

gap spacing values, and compared these results to equivalent tapered apertures with no gap and to the input pulse. These data are shown in Fig. 10.3, with the positions where the measurements were taken given in the figure legend. Although the incident beam was divergent at the plane of the input aperture, as shown in Fig. 10.2(b), all three tapered aperture configurations still allow for a factor of ~ 3 concentration of the incident radiation. For the tapered aperture (g = 0 μm), the spectrum is strongly suppressed at frequencies below the cutoff frequency of 1 THz, though the tapered nature of the aperture ensures that there is not a sharp cutoff at that frequency [20]. For both SSTAs, lower frequencies are clearly enhanced relative to g = 0 μm tapered aperture. Both SSTAs also exhibit a dip in the 1.5 - 1.75 THz region, which may be due to reflections within the more complex structure. On the high frequency side, the reduced transmission above ~ 2.75 THz is associated with the frequency response of the THz system. For the SSTAs, even very small gaps allow for significant broadening of the transmitted THz spectrum. In fact, there appears to be relatively little difference between an SSTA with g = ~ 5 μm and g = ~ 20 μm. However, the transmission peak at ~ 2 THz becomes noticeably reduced for larger values of g. In all three cases, the transmission below 0.5 THz is relatively small. In fact, the spectral amplitude in this low frequency regime is smaller than we expected based on numerical simulations (not shown). The low amplitude below 0.5 THz may be the result of slight misalignment between the two pieces of the SSTA, as well as some surface roughness on the sidewalls that form the gap. Based on the experimental results, we use a gap of ~ 20 μm for all of the subsequent imaging work.

Figure 10.4 summarizes the basic spatial properties of the THz electric field measured approximately 10 μm from the output aperture of the SSTA. In order to

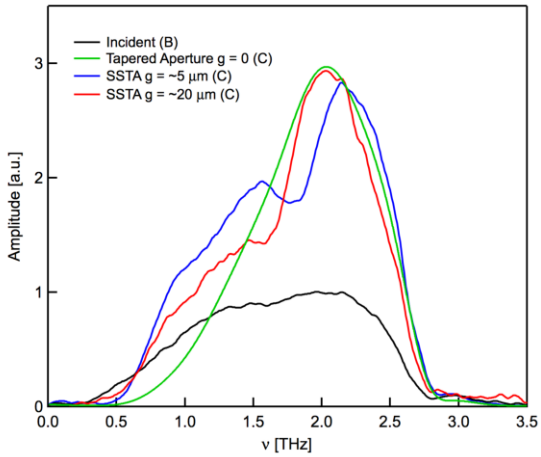

Figure 10.3. Amplitude spectra of the THz electric field incident and transmitted through the SSTAs for two different values of the gap spacing, g, and for a tapered aperture with g = 0. The maximum value of the incident field is scaled to 1.

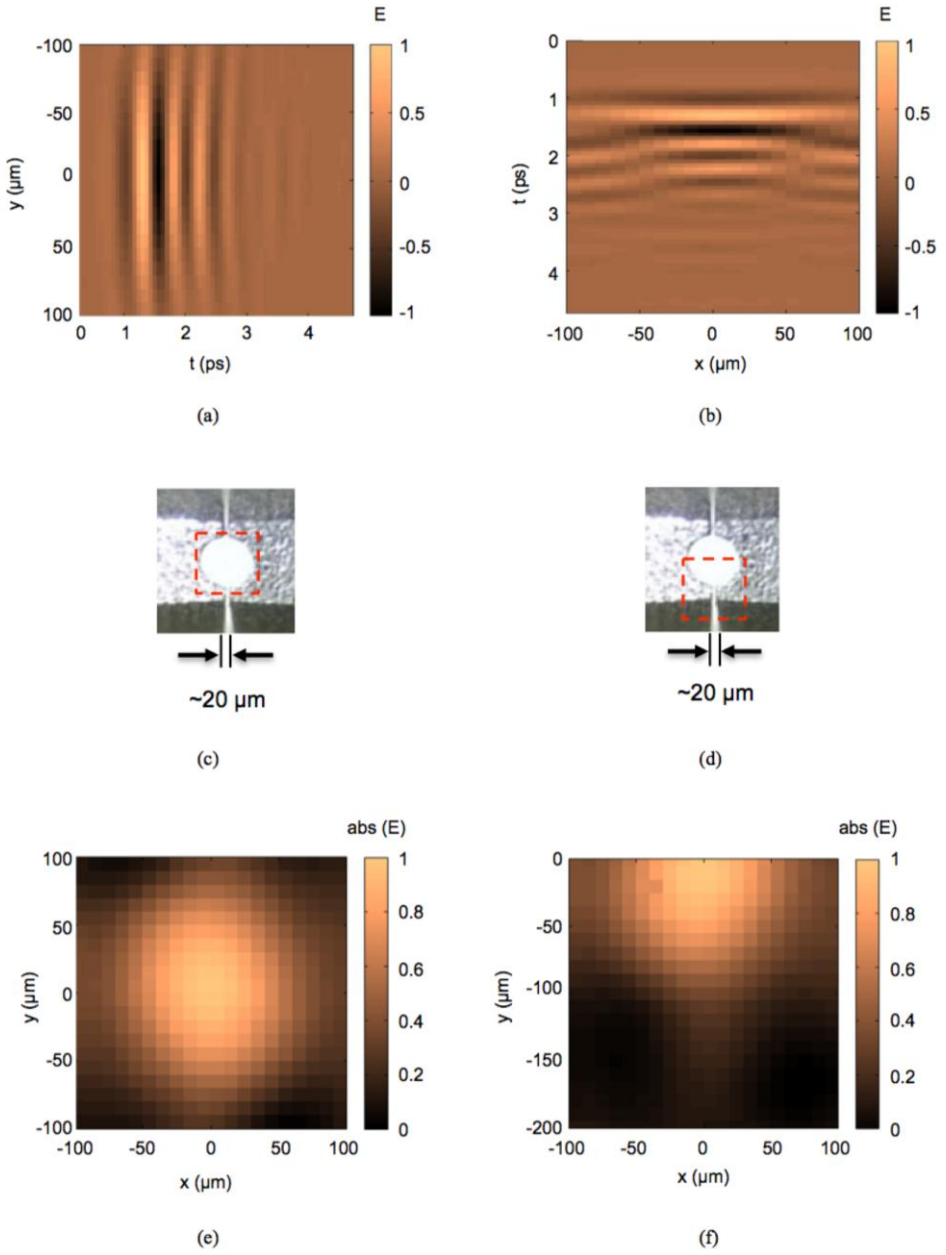

Figure 10.4. Measurement of the THz electric field distribution at the aperture output. (a) Temporal waveform measured close to the output aperture along x-axis, at the center of the aperture, as an example. (b) Temporal waveform measured close to the output aperture along y-axis, at the center of the aperture, as an example. (c) The photo of the output aperture taken from the bottom with the region circled by the red dashed line that is scanned. (d) The photo of the output aperture taken from the bottom with another region circled by the red dashed line that is scanned. (e) Field distribution (bottom image) in the proximity to the center of the output aperture (top photo) of the SSTA with a gap g = ~ 20 μm, with the value in the image obtained at a specific time point t = 1.27 ps in the temporal waveform from the experiment. (f) Field distribution (bottom image) in the proximity to the bottom edge of the output aperture (top photo) of the SSTA with a gap g = ~ 20 μm, again the value in the image obtained at a specific time point t = 1.27 ps in the temporal waveform from the experiment.

properly assess these spatial properties, we initially measured the THz time-domain electric field properties across a 200 μm × 200 μm region centered around the SSTA. Figures 10.4(a) and 10.4(b) show space-time maps of the measured THz waveforms along the x and y-axes, respectively. It is apparent from both plots that the maximum of the initial bipolar waveform occurs at approximately t = 1.27 ps, regardless of the position within that region. Therefore, we can simply use the field magnitude at that temporal position to map out the THz electric field. In Figs. 10.4(c) and 10.4(d), we show the specific regions that were interrogated. Finally, in Figs. 10.4(e) and 10.4(f), we show the measured field distributions taken in 10 μm increments along both axes. It is clear that despite a 20-μm gap between the two portions of the SSTA, the THz electric field is strongly confined within the region of the output aperture. This is also consistent with earlier numerical simulations on similar structures [20].

Using the experimental system shown in Fig. 10.2(a), we now demonstrate the imaging capabilities of the SSTA probe. We fabricated a U-shaped aperture via laser ablation in a 75-μm-thick free-standing stainless steel foil. A schematic diagram of the geometry is shown in Fig. 10.5(a) and a photograph of the sample is shown in Fig. 10.5(b). The sample was positioned <50 μm from the SSTA, so that it could be scanned along both transverse axes in 100 μm increments. For each pixel, we measured the THz time-domain waveform, Fourier transformed it, and used the resulting amplitude values at four separate frequencies (0.5 THz, 0.8 THz, 1.0 THz and 1.5 THz) to create false color images. These images are shown in Figs. 10.5(c)-10.5(f). While the image quality is reduced with decreasing frequency, the image of the U is still clearly visible even for frequencies well below the cutoff frequency. It is worth noting that we were not able to obtain such images for frequencies below cutoff using a conventional tapered aperture (g

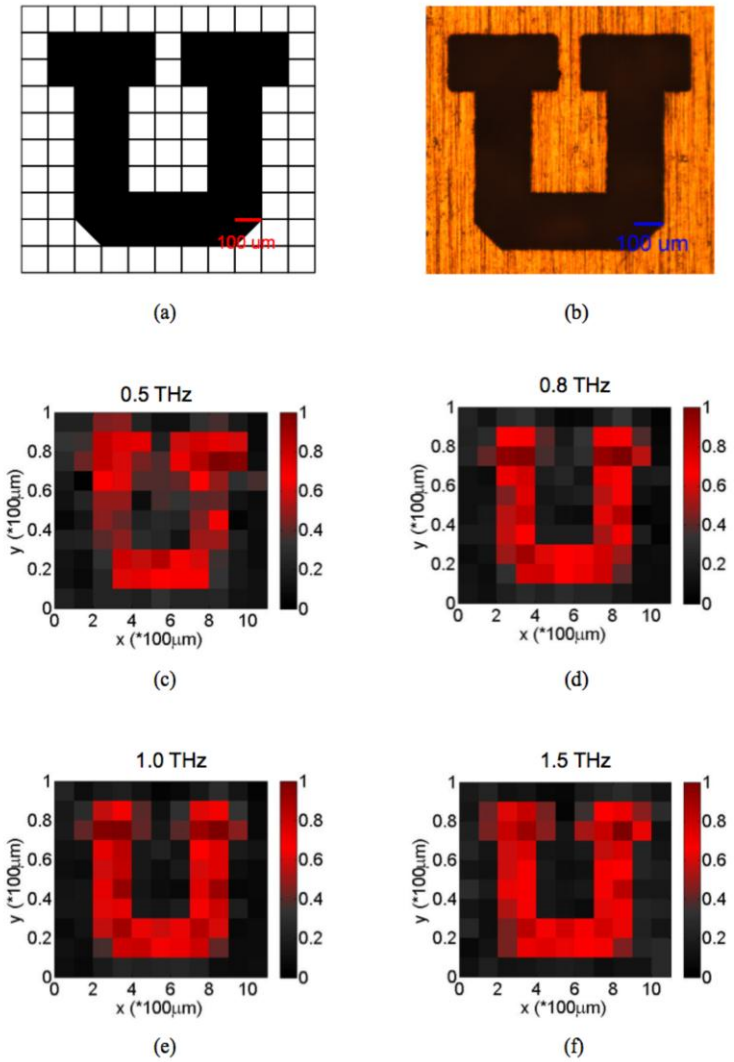

Figure 10.5. Imaging using an SSTA with an output aperture diameter of 180 μm and g = 60 μm. (a) Design of a U-shaped aperture. (b) Photograph of the fabricated structure in a 75-μm-thick free-standing stainless steel foil. Near field images of the structure at (c) 0.5 THz, (d) 0.8 THz, (e) 1.0 THz and (f) 1.5 THz.

= 0 μm).

10.4 Conclusion

In summary, we have demonstrated the utility of a split shell tapered aperture for near-field THz imaging. The structure consists of two halves of a conventional tapered aperture, allowing for the introduction of a variable gap between the two pieces. By virtue of the narrow sidewalls in the vicinity of the gap, the structure allows for broadband THz propagation, maintains its ability to concentrate the incident THz radiation across that spectral range, and allows for electric field confinement in a region determined by the output aperture. Based on these characteristics, we demonstrate near-field imaging of an aperture fabricated in a metal foil at several different frequencies above and below the cutoff frequency. Further refinement in the fabrication of the probe should allow for improved imaging capabilities at even lower frequencies. The results suggest that this device may be useful for near-field imaging at frequencies well below the diffraction limit.

10.5 References

1. E. H. Synge, "A suggested method for extending microscopic resolution into the ultra-microscopic region," Philos. Mag. **6**, 356–362 (1928).

2. E. A. Ash and G. Nicholls, "Super-resolution aperture scanning microscope," Nature **237**, 510–512 (1972).

3. A. Lewis, M. Isaacson, A. Harootunian, and A. Muray, "Development of a 500 Å spatial resolution light microscope: I. light is efficiently transmitted through λ/16 diameter apertures," Ultramicroscopy **13**, 227–231 (1984).

4. D. W. Pohl, W. Denk, and M. Lanz, "Optical stethoscopy: Image recording with resolution λ/20," Appl. Phys. Lett. **44**, 651-653 (1984).

5. F. Zenhausern, M. P. O'Boyle, and H. K. Wickramasinghe, "Apertureless near-field optical microscope," Appl. Phys. Lett. **65**, 1623–1625 (1994).

6. Y. Inouye and S. Kawata, "Near-field scanning optical microscope with a metallic

probe tip," Opt. Lett. **19**, 159 (1994).

7. H.-T. Chen, R. Kersting, and G. C. Cho, "Terahertz imaging with nanometer resolution," Appl. Phys. Lett. **83**, 3009–3011 (2003).

8. T. L. Cocker, V. Jelic, M. Gupta, S. J. Molesky, J. A. J. Burgess, G. D. L. Reyes, L. V. Titova, Y. Y. Tsui, M. R. Freeman, and F. A. Hegmann, "An ultrafast terahertz scanning tunnelling microscope," Nat Photon **7**, 620–625 (2013).

9. M. M. Awad and R. A. Cheville, "Transmission terahertz waveguide-based imaging below the diffraction limit," Appl. Phys. Lett. **86**, 221107 (2005).

10. H. Zhan, R. Mendis, and D. M. Mittleman, "Superfocusing terahertz waves below λ/250 using plasmonic parallel-plate waveguides," Opt. Express **18**, 9643–9650 (2010).

11. N. Klein, P. Lahl, U. Poppe, F. Kadlec, and P. Kužel, "A metal-dielectric antenna for terahertz near-field imaging," J. Appl. Phys. **98**, 014910 (2005).

12. K. Ishihara, K. Ohashi, T. Ikari, H. Minamide, H. Yokoyama, J. Shikata, and H. Ito, "Terahertz-wave near-field imaging with subwavelength resolution using surface-wave-assisted bow-tie aperture," Appl. Phys. Lett. **89**, 201120 (2006).

13. A. Bitzer and M. Walther, "Terahertz near-field imaging of metallic subwavelength holes and hole arrays," Appl. Phys. Lett. **92**, 231101 (2008).

14. O. Mitrofanov, C. C. Renaud, and A. J. Seeds, "Terahertz probe for spectroscopy of sub-wavelength objects," Opt. Express **20**, 6197 (2012).

15. Betzig, J. K. Trautman, T. D. Harris, J. S. Weiner, and R. L. Kostelak, "Breaking the diffraction barrier: optical microscopy on a nanometric scale," Science **251**, 1468–1470 (1991).

16. C. A. Balanis, Advanced Engineering Electromagnetics (John Wiley & Sons, 1989).

17. M. I. Stockman, "Nanofocusing of optical energy in tapered plasmonic waveguides," Phys. Rev. Lett. **106**, 019901 (2011).

18. S. Hunsche, M. Koch, I. Brener, and M. C. Nuss, "THz near-field imaging," Opt. Commun. **150**, 22–26 (1998).

19. T. D. Nguyen, Z. V. Vardeny, and A. Nahata, "Concentration of terahertz radiation through a conically tapered aperture," Opt. Express **18**, 25441–25448 (2010).

20. S. Liu, Z. V. Vardeny, and A. Nahata, "Concentration of broadband terahertz radiation using a periodic array of conically tapered apertures," Opt. Express **21**, 12363–12372 (2013).

21. S. Liu, O. Mitrofanov, and A. Nahata, "Transmission bleaching and coupling crossover in a split tapered aperture," Opt. Express **21**, 30895–30902 (2013).

22. O. Mitrofanov, M. Lee, J. W. P. Hsu, I. Brener, R. Harel, J. F. Federici, J. D. Wynn, L. N. Pfeiffer, and K. W. West, "Collection-mode near-field imaging with 0.5-THz pulses," IEEE Sel. Top. Quant. Electron. **7**, 600–607 (2001).

CHAPTER 11

FUTURE WORK AND CONCLUSIONS

11.1 Future Work

Based on the understanding of surface-plasmonic features of the structures we studied and the capabilities we gained during the course of research, we propose to extend our work in the following directions.

11.1.1 Reconfigurable filters and beam shaper using "exotic" media

The ability of two-dimensional (2D) subwavelength lattices to enhance amplitude transmission at resonance frequencies has been demonstrated using a variety of different materials and geometries, and focused primarily on passive devices [1,2]. The applications associated with 2D plasmonic lattices include molecular sensing and spectroscopy [2–4], photonic devices and methods [2], lithography and imaging [5–8], and even quantum optics [9,10] and nonlinear optics [11–13]. Even though several approaches have been exploited to create active device capabilities, the tuning capabilities are rather limited, e.g., in most cases the geometries of the structure are fixed after fabrication [11,12,14–32]. With this in mind, we propose to design, fabricate, and characterize a new class of 2D subwavelength plasmonic lattices that differ fundamentally from all prior published work and in that they allow for more flexible control of the 2D geometries. The goal of this work is to develop the active components

for spectral tuning and spatial beam shaping. From the investigation of the surface plasmon propagation, each hole in the periodic lattice could be regarded as a scattering point source, and the interferences between the scattering centers result in the resonance. Therefore, we could also restructure the lattice in a more flexible manner by altering the local transmission properties of the dielectric substrate or/and superstrate around each hole. It is easier to change the properties of dielectric media other than metals. We are currently investigating the possible materials and the work could be accomplished by carefully selecting the material.

11.1.2 Design and experimental implementation of transformational optic devices

As noted in Chapter 2, transformation optics is a unique approach for confining and controlling the flow of electromagnetic radiation. This mission is accomplished by mapping the material properties to eliminate field distortion [33,34]. Although the transformation algorithm is powerful and promising, most of the devices conceived are still within the theoretical framework. In our earlier work, we studied the dielectric component between co-polarized incident and transmitted radiation. However, with more careful and complete measurement of the electric and magnetic field [35], all components in the permittivity and permeability matrices could be obtained, even for the anisotropic and magneto-optic materials. Based on the understanding we gained from modeling the dielectric properties, we could estimate the properties of more metamaterial structures. Moreover, against that the resonant responses of most periodic geometries are limited within a narrow band, the random aperture arrays we worked on not only provide designed plasma frequency but also have a rather flat dielectric response. Using this

approach, we propose to extend the ability to characterize and engineer the properties of metamaterials to a broader range of materials, e.g., magneto-optic materials, and to design and implement transformation optic devices based on their specific features.

11.1.3 Active terahertz single-mode waveguide

Given the scarcity of device capabilities that currently exist at terahertz (THz) frequencies, there is great need for the development of broad classes of device capabilities. One of the simplest needs is the capability to route information between points. Although a number of waveguide geometries have been developed [36], using a variety of metal, semiconductor and polymer-based architectures, there have been relatively few experimental realizations of more complex guided-wave devices. A limitation that has hindered greater exploration in this direction is the fact that a large fraction of the dielectric waveguide materials for such geometries exhibit nonnegligible absorption and dispersion throughout the THz frequency range. Alternatively, metal waveguides offer a simple means for confining long-wavelength electromagnetic radiation. Given the high conductivity of metals at these wavelengths, propagation losses can be relatively small. In fact, the losses associated with metals are significantly smaller than with almost all dielectric materials in the THz frequency range. Under such circumstances, the propagation properties of THz pulses have been examined using a number of different metallic waveguide structures [37–39]. Even in these forms, the devices have been largely passive and not active. With this in mind, we propose to design, fabricate, and characterize a new class of THz waveguide structures that are planar, though fabricated from a multilayer construction, and can be filled with materials that respond to external stimuli. The goal of this work is to experimentally realize both

passive and active planar THz waveguide devices as a means of developing THz circuits. This goal may be accomplished using U-shaped metallic waveguides with embedded nonlinear optical materials, as shown schematically in Fig. 11.1. We are currently examining such structures theoretically to determine the optimal waveguide geometry.

11.2 Conclusions

Our work on the design, fabrication and characterization of plasmonic metamaterials and tapered structures is presented in this dissertation. The work was carried out to further understand the mechanisms underlying the phenomenon and to utilize them for THz optoelectronics devices and systems. In what follows we briefly summarize the results and conclusions drawn from the discussions in previous chapters.

In Chapter 2, we measured the complex dielectric function, $\varepsilon(\omega)$, at THz frequencies for random and periodic aperture arrays perforated in metallic films. We theoretically analyzed the extraction of the dielectric constants from the transmitted electric fields. From our previous studies, $\varepsilon(\omega)$ consists of a superposition of an effective

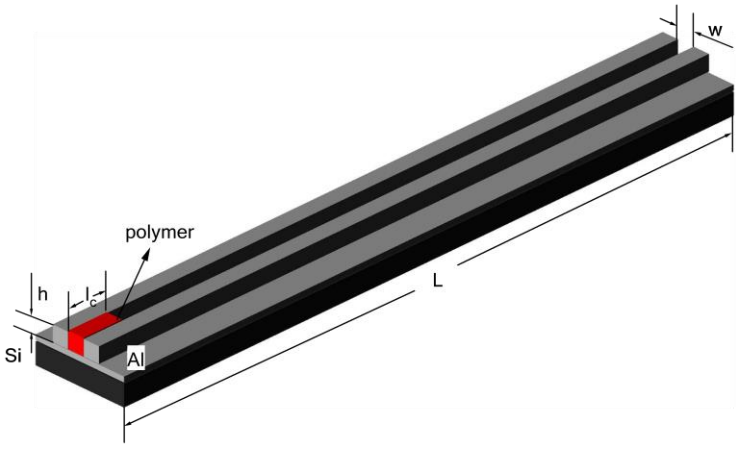

Figure 11.1. Schematic diagram of the proposed modified slot waveguide with a poled polymer (shown in red) embedded into the structure near the input.

‘plasma-like’ response that is associated with the uncorrelated individual apertures, and discrete resonance oscillation that is associated with the launched SPP interference related to the reciprocal vectors of the underlying aperture arrays in the Fourier space. Therefore, the dielectric responses could be modeled quantitatively according to the geometric parameters. For instance, the effective plasma frequency is determined by the diameter of the individual apertures, and the transverse optical (TO) frequencies are described by the antiresonance (AR) dip frequencies which are attributed to the periodicity of the lattice. Based on these conclusions, we further noticed that the resonance peak frequencies should also contribute to the formula model, reflected in the longitudinal optical (LO) frequencies. Due to this, we also modified the formula based on the careful observation of the Fano-resonance shape, and obtained a better fit to the experimentally extracted dielectric response. Moreover, we demonstrated the generalized application of this modeling. With a full measurement of all the components of the electric and magnetic fields, the dielectric function, $\varepsilon(\omega)$, could construct a complete model of the plasmonic metamaterials and deepen our understanding of the underlying surface plasmonic mechanisms in a broader field.

Our results that carefully designed multilayer aperture arrays can allow for two important device capabilities are demonstrated in Chapter 3: (1) the introduction of additional resonances associated with the layer spacing, which may be used to generate more complex THz spectral filtering properties, and (2) the ability to create high quality narrow bandpass THz filters. These capabilities were illustrated primarily using double-layer aperture arrays, although multilayer structures may allow for additional refinement of the transmission properties. In addition, the use of aperiodic geometries [40] as well as

conductive nonmetallic materials [41–43] may allow for greater control over the MFP resonance frequencies, as well as the potential for active THz optoelectronic device applications. Finally, it should be noted that interesting "three dimensional" structures, using stacks of aperture array layers in a variety of geometries, may give rise to new and interesting optical interference phenomena.

In Chapter 4, we investigated THz transmission through a ~7.5 μm-thick HOPG film using THz time-domain spectroscopy with the incident radiation polarized perpendicular to the graphite c axis. We obtained the complex refraction index and $\varepsilon(\omega)$ spectra using the measured transmission amplitude and phase, without the need of Kramer-Kronig transformations and related approximations. The $\varepsilon(\omega)$ spectrum was fit with the Drude model, from which we obtained the graphite plasma frequency, ν_p = 34 THz; this value is consistent with the low carrier density of graphite at room temperature. Despite the low plasma frequency, graphite clearly supports SPP excitations in the THz spectral range. To prove this we perforated the graphite film with periodic subwavelength HAs and measured resonant enhanced transmission, which arises from interference between SPPs on the film surfaces. Although graphite exhibits a lower conductivity than other conventional metals, such as stainless steel, the resonant transmission properties are similar in nature. This demonstrates that a broad range of similar materials may be useful for THz plasmonic applications.

In Chapter 5, we fabricated sub 100 μm-thick freestanding and highly oriented MWCNT sheets using the catalytic chemical vapor deposition method. Using THz-TDS we measured the complex index of refraction spectra of the sheets for two orthogonal nanotube orientations. We found that the thick CNT sheet shows highly anisotropic THz

polarization behavior with extinction ratio values of ~40. We investigated the existence and propagation of SPP excitations at THz frequencies by studying the resonantly enhanced transmission spectra through periodic aperture arrays fabricated on the MWCNT sheets. We found that CNTs support SPP propagation along the tubes. However, no SPP-related enhanced transmission was detected in the perpendicular direction. Furthermore we found that resonantly enhanced transmission is absent in aperture arrays fabricated on a thick MWCNT sheet, although the individual apertures still act as transmission enhancers. These somewhat contradictory results can be explained by the strong reabsorption of the SPP excitations on the CNT sheet, which prevents SPP propagation along the surfaces.

In Chapter 6, we experimentally demonstrated a coherent SPP-based narrowband THz detector by fabricating a portion of a circular grating about a conventional dipole antenna. We observed a factor of two enhancement at the designated frequency, although numerical simulations suggest that much larger enhancement factors can be obtained. The grating allows for the collection of incident radiation outside of the dipole region via coupling to SPPs, obviating the need for a substrate lens. By superimposing multiple periodicities and varying the details of the grooves, it is possible to obtain enhanced detection sensitivity at multiple frequencies. In the current work, these antennas have only been used for coherent detection. They should work equally well as narrowband or multiband THz emitters.

In order to conduct subsequent research more systematically, we experimentally studied individual aperture parameters, specifically the determination of the optimal taper angle, in Chapter 7. Interestingly, the effective cutoff frequency red shifted with

increasing taper angle, which was a consequence of the rate of change in a continuously varying aperture diameter. Further characterization of the tapered aperture structure through numerical method also confirmed our findings. This investigation provided us with further understanding of the tapered apertures and "best parameters" for the next step of the research.

Then in Chapter 8, we demonstrated experimentally that periodic arrays of tapered apertures are able to concentrate broadband THz radiation. With the optimal taper angle we studied earlier, we constructed a hexagonal lattice of nineteen TAs that led to a factor of ~ 10 increase in the broadband THz throughput for frequencies above the effective cutoff frequency. Further concentration of the transmitted radiation with higher field density was shown to be possible by tilting the apertures in an array toward the array center. Such a demonstration suggests that cascaded TA structures may allow for an even greater level of field concentration than any single layer structure is capable of providing.

In Chapter 9, we experimentally characterized the spectral properties of a split tapered aperture that incorporated a variable spacing gap between the two halves of the metallic screen in order to eliminate the aperture cutoff effect and enable broadband confinement of THz pulses. However, we found that the peak spectral transmission was greatest when there was no gap and that the peak decreased steadily as the gap spacing was increased. Correspondingly, there was a crossover in the coupling coefficient between the TA mode and a TEM mode. This was verified both experimentally and numerically. Interestingly, we also found that an alternate embodiment of the split TA, one in which the wall thickness was small, appeared to do a better job of concentrating radiation (maintaining a relatively small spot size) while allowing for more broadband

radiation to be transmitted. Moreover, we proved that such a structure also led to a greater concentrated intensity compared with a conventional optical focusing lens under the same circumstances. Therefore, such approaches may be useful in developing structures that enable the concentration of truly broadband radiation.

Last in Chapter 10, we experimentally demonstrated the utility of a split shell tapered aperture for near-field THz imaging. The structure consists of two halves of a conventional tapered aperture, allowing for the introduction of a variable gap between the two pieces. By virtue of the narrow sidewalls in the vicinity of the gap, the structure allows for broadband THz propagation, maintains its ability to concentrate the incident THz radiation across that spectral range, and allows for electric field confinement in a region determined by the output aperture. Based on these characteristics, we demonstrate near-field imaging of an aperture fabricated in a metal foil at several different frequencies above and below the cutoff frequency. Further refinement in the fabrication of the probe should allow for improved imaging capabilities at even lower frequencies. The results suggest that this device may be useful for near-field imaging at frequencies well below the diffraction limit.

10.3 References

1. C. Genet and T. W. Ebbesen, “Light in tiny holes,” Nature **445**(7123), 39–46 (2007).
2. F. J. Garcia-Vidal, L. Martin-Moreno, T. W. Ebbesen, and L. Kuipers, “Light passing through subwavelength apertures,” Rev. Mod. Phys. **82**(1), 729–787 (2010).
3. R. Gordon, D. Sinton, K. L. Kavanagh, and A. G. Brolo, “A new generation of sensors based on extraordinary optical transmission,” Acc. Chem. Res. **41**(8), 1049–1057 (2008).
4. D. Sinton, R. Gordon, and A. Brolo, “Nanohole arrays in metal films as optofluidic elements: progress and potential,” Microfluid. Nanofluid. **4**(1–2), 107–116 (2008).

5. Z. Xie, W. Yu, T. Wang, H. Zhang, Y. Fu, H. Liu, F. Li, Z. Lu, and Q. Sun, "Plasmonic nanolithography: A review," Plasmonics **6**(3), 565–580 (2011).

6. R. Bakker, V. Drachev, H.-K. Yuan, and V. Shalaev, "Enhanced transmission in near-field imaging of layered plasmonic structures.," Opt. Express **12**(16), 3701–3706 (2004).

7. F. Miyamaru, M. W. Takeda, T. Suzuki, and C. Otani, "Highly sensitive surface plasmon terahertz imaging with planar plasmonic crystals," Opt. Express **15**(22), 14804–14809 (2007).

8. N. C. Lindquist, A. Lesuffleur, H. Im, and S.-H. Oh, "Sub-micron resolution surface plasmon resonance imaging enabled by nanohole arrays with surrounding Bragg mirrors for enhanced sensitivity and isolation," Lab Chip **9**(3), 382–387 (2009).

9. E. Altewischer, M. P. van Exter, and J. P. Woerdman, "Plasmon-assisted transmission of entangled photons," Nature **418**(6895), 304–306 (2002).

10. S. Fasel, F. Robin, E. Moreno, D. Erni, N. Gisin, and H. Zbinden, "Energy-time entanglement preservation in plasmon-assisted light transmission," Phys. Rev. Lett. **94**(11), 110501 (2005).

11. I. Smolyaninov, A. V. Zayats, A. Stanishevsky, and C. C. Davis, "Optical control of photon tunneling through an array of nanometer-scale cylindrical channels," Phys. Rev. B **66**(20), 205414 (2002).

12. G. Wurtz, R. Pollard, and A. V. Zayats, "Optical bistability in nonlinear surface-plasmon polaritonic crystals," Phys. Rev. Lett. **97**(5), 057402 (2006).

13. M. Kauranen and A. V. Zayats, "Nonlinear plasmonics," Nat. Photonics **6**, 737–748 (2012).

14. J. G. Rivas, P. H. Bolivar, and H. Kurz, "Thermal switching of the enhanced transmission of terahertz radiation through subwavelength apertures," Opt. Lett. **29**(14), 1680–1682 (2004).

15. T. Ribaudo, E. A Shaner, S. S. Howard, C. Gmachl, X. J. Wang, F.-S. Choa, and D. Wasserman, "Active control and spatial mapping of mid-infrared propagating surface plasmons," Opt. Express **17**(9), 7019–7024 (2009).

16. A. Tsiatmas, A. R. Buckingham, V. A. Fedotov, S. Wang, Y. Chen, P. A. J. de Groot, and N. I. Zheludev, "Superconducting plasmonics and extraordinary transmission," Appl. Phys. Lett. **97**(11), 111106 (2010).

17. Z. Tian, R. Singh, J. Han, J. Gu, Q. Xing, J. Wu, and W. Zhang, "Terahertz superconducting plasmonic hole array," Opt. Lett. **35**(21), 3586–3588 (2010).

18. X. Fang, C. Zhuang, Z. Wen, X. Han, Q. Feng, X. X. Xi, F. Nori, X. Xie, Q. Niu, and

X. Qiu, "Influence of intrinsic electronic properties on light transmission through subwavelength holes on gold and MgB_2 thin films," Phys. Rev. B **84**(20), 205438 (2011).

19. H.-T. Chen, H. Lu, A. K. Azad, R. D. Averitt, A. C. Gossard, S. A Trugman, J. F. O'Hara, and A. J. Taylor, "Electronic control of extraordinary terahertz transmission through subwavelength metal hole arrays," Opt. Express **16**(11), 7641–7648 (2008).

20. T. J. Kim, T. Thio, T. W. Ebbesen, D. E. Grupp, and H. J. Lezec, "Control of optical transmission through metals perforated with subwavelength hole arrays," Opt. Lett. **24**(4), 256–258 (1999).

21. C.-L. Pan, C.-F. Hsieh, R.-P. Pan, M. Tanaka, F. Miyamaru, M. Tani, and M. Hangyo, "Control of enhanced THz transmission through metallic hole arrays using nematic liquid crystal," Opt. Express **13**(11), 3921–3930 (2005).

22. J. Han, A. Lakhtakia, Z. Tian, X. Lu, and W. Zhang, "Magnetic and magnetothermal tunabilities of subwavelength-hole arrays in a semiconductor sheet," Opt. Lett. **34**(9), 1465–1467 (2009).

23. C. Janke, J. G. Rivas, P. H. Bolivar, and H. Kurz, "All-optical switching of the transmission of electromagnetic radiation through subwavelength apertures," Opt. Lett. **30**(18), 2357–2359 (2005).

24. E. Hendry, M. Lockyear, J. Gómez Rivas, L. Kuipers, and M. Bonn, "Ultrafast optical switching of the THz transmission through metallic subwavelength hole arrays," Phys. Rev. B **75**(23), 235305 (2007).

25. A. K. Azad, H.-T. Chen, S. R. Kasarla, A. J. Taylor, Z. Tian, X. Lu, W. Zhang, H. Lu, A. C. Gossard, and J. F. O'Hara, "Ultrafast optical control of terahertz surface plasmons in subwavelength hole arrays at room temperature," Appl. Phys. Lett. **95**(1), 011105 (2009).

26. J. Dintinger, I. Robel, P. V. Kamat, C. Genet, and T. W. Ebbesen, "Terahertz all-optical molecule-plasmon modulation," Adv. Mater. **18**(13), 1645–1648 (2006).

27. J. Gu, R. Singh, A. K. Azad, J. Han, A. J. Taylor, J. F. O'Hara, and W. Zhang, "An active hybrid plasmonic metamaterial," Opt. Mater. Express **2**(1), 31–37 (2011).

28. B. Gjonaj, J. Aulbach, P. M. Johnson, A. P. Mosk, L. Kuipers, and A. Lagendijk, "Active spatial control of plasmonic fields," Nat. Photonics **5**(6), 360–363 (2011).

29. J. Wang, S. Liu, Z. V. Vardeny, and A. Nahata, "Liquid metal-based plasmonics," Opt. Express **20**(3), 2346–2353 (2012).

30. J. Wang, S. Liu, and A. Nahata, "Reconfigurable plasmonic devices using liquid metals," Opt. Express **20**(11), 12119–12126 (2012).

31. J. Wang, S. Liu, S. Guruswamy, and A. Nahata, "Reconfigurable liquid metal based terahertz metamaterials via selective erasure and refilling to the unit cell level," Appl. Phys. Lett. **103**(22), 221116 (2013).

32. J. Wang, S. Liu, S. Guruswamy, and A. Nahata, "Reconfigurable terahertz metamaterial device with pressure memory," Opt. Express **22**(4), 1097–1104 (2014).

33. U. Leonhardt, "Optical conformal mapping," Science **312**(5781), 1777–1780 (2006).

34. J. B. Pendry, D. Schurig, and D. R. Smith, "Controlling electromagnetic fields," Science **312**(5781), 1780–1782 (2006).

35. M. Burresi, D. van Oosten, T. Kampfrath, H. Schoenmaker, R. Heideman, A. Leinse, and L. Kuipers, "Probing the magnetic field of light at optical frequencies," Science **326**(5952), 550–553 (2009).

36. S. Atakaramians, S. A. V., T. M. Monro, and D. Abbott, "Terahertz dielectric waveguides," Adv. Opt. Photonics **5**, 169–215 (2013).

37. G. Gallot, S. P. Jamison, R. W. McGowan, and D. Grischkowsky, "Terahertz waveguides," J. Opt. Soc. Am. B **17**(5), 851–863 (2000).

38. R. Mendis and D. Grischkowsky, "Undistorted guided-wave propagation of subpicosecond terahertz pulses," Opt. Lett. **26**(11), 846–848 (2001).

39. W. Zhu, A. Agrawal, and A. Nahata, "Planar plasmonic terahertz guided-wave devices," Opt. Express **16**(9), 6216–6226 (2008).

40. T. Matsui, A. Agrawal, A. Nahata, and Z. V. Vardeny, "Transmission resonances through aperiodic arrays of subwavelength apertures," Nature **446**(7135), 517–521 (2007).

41. T. D. Nguyen, S. Liu, G. Kumar, A. Nahata, and Z. V. Vardeny, "Terahertz plasmonic properties of highly oriented pyrolytic graphite," Appl. Phys. Lett. **102**(17), 171107 (2013).

42. T. D. Nguyen, S. Liu, M. D. Lima, S. Fang, R. H. Baughman, A. Nahata, and Z. V. Vardeny, "Terahertz surface plasmon polaritons on freestanding multi-walled carbon nanotube aerogel sheets," Opt. Mater. Express **2**(6), 782–788 (2012).

43. T. Matsui, Z. V. Vardeny, A. Agrawal, A. Nahata, and R. Menon, "Resonantly-enhanced transmission through a periodic array of subwavelength apertures in heavily-doped conducting polymer films," Appl. Phys. Lett. **88**(7), 071101 (2006).